STRUCTURE OF THE DIFFUSION REGION IN THREE DIMENSIONAL MAGNETIC RECONNECTION

by

John C. Meyer III

A dissertation submitted to the Faculty of the University of Delaware in partial fulfillment of the requirements for the degree of Doctor of Philosophy in Physics

Winter 2015

ProQuest LLC.
789 East Eisenhower Parkway
P.O. Box 1346
Ann Arbor, MI 48106 - 1346

STRUCTURE OF THE DIFFUSION REGION IN

THREE DIMENSIONAL MAGNETIC RECONNECTION

by

John C. Meyer III

Approved: _____

Edmund R. Nowak, Ph.D.
Chair of the Department of Physics & Astronomy

Approved: _____

George H. Watson, Ph.D.
Dean of the College of College Arts & Sciences

Approved: _____

James G. Richards, Ph.D.
Vice Provost for Graduate and Professional Education

I certify that I have read this dissertation and that in my opinion it meets the academic and professional standard required by the University as a dissertation for the degree of Doctor of Philosophy.

Signed: _____

Michael A. Shay, Ph.D.
Professor in charge of dissertation

I certify that I have read this dissertation and that in my opinion it meets the academic and professional standard required by the University as a dissertation for the degree of Doctor of Philosophy.

Signed: _____

Qaisar Shafi, Ph.D.
Member of dissertation committee

I certify that I have read this dissertation and that in my opinion it meets the academic and professional standard required by the University as a dissertation for the degree of Doctor of Philosophy.

Signed: _____

Michael R. Brown, Ph.D.
Member of dissertation committee

I certify that I have read this dissertation and that in my opinion it meets the academic and professional standard required by the University as a dissertation for the degree of Doctor of Philosophy.

Signed: _____

William H. Matthaeus, Ph.D.
Member of dissertation committee

ACKNOWLEDGMENTS

I would like to thank my graduate committee for their service. Your time is valuable and I am very grateful to you for sharing it with me.

Paul Cassak, your tutelage in the early years of my plasma study was invaluable. Even now, I've often returned to your notes and continued to find insight within them.

Tulasi and Kittipat, it would almost be crass to mention my gratitude here. Your friendship and camaraderie made the entire journey many times more enjoyable and enriching.

Finally, Mike, you must be a saint. Not only have I heard it said again and again, but I feel it to be true in my bones. Nothing short of that could explain your perseverance with me through all of the difficulties I have made for you. If ever you need a character reference, I stand as a walking testament to its quality. Thank you, very much.

TABLE OF CONTENTS

LIST OF TABLES

LIST OF FIGURES

ABSTRACT

Although magnetic reconnection has been successfully used to explain many different astrophysical phenomena, it has yet to demonstrate some key properties observed in smaller bursty plasma flows within the magnetotail. In this thesis, we present 3D Hall simulations demonstrating that under wide equilibrium current sheet conditions, magnetic reconnection will become transient and localized. In doing so, we show that magnetic reconnection is capable of producing the bursty bulk flows observed in the magnetotail.

Toward this goal, we first introduce a new framework for analyzing 3D magnetic reconnection. Using this framework, we deconstruct the significant physical structures and processes comprising x-lines derived from a thin equilibrium current sheets. After establishing this mapping of the 3D diffusion region, we move on to probe the more marginal cases of reconnection which result from very wide equilibrium current sheets.

Finally, we incorporate all of this into a simple analytical model for 3D reconnection -- reproducing many of the observed properties of both transient magnetic reconnection and long-lasting magnetic reconnection.

By doing so, not only do we expand upon the known behaviors of magnetic reconnection, but we also present novel insight into the mechanisms behind these behaviors.

Chapter 1

INTRODUCTION

From our perspective, comfortable within the bubble of our planet, space has a certain clean austerity to it. Stars twinkle in a cold lonely luminescence while floating in a vast and empty nothingness. Since the very first creatures climbed from the seas until the present day, any life which has looked skyward has seen a quintessential vision played out in the majesty of the evening tapestry. With this view of space granted almost as a primordial birthright, we are naturally ill prepared to understand the gossamer breath of magnetism stretching across the intervening emptiness of the cosmos. If only we could sit atop a mountain, noses aloft, and smell the tenuous vapors of space. Then we might know something of the unseen space. We might know magnetism, like we know of crisp Fall breezes or the smoky umbrage of an explosive New Year's Eve. In that case, we may be in a good position to understand the nuanced importance of magnetic reconnection in the order of all things. Unfortunately, such is not the case. We were not so endowed in our creation and for most of our natural history, have lacked a vital understanding of the processes among the stars. So it is left to the mean faculties of our imagination to temper truth from mathematics. We must sieve purpose, path, energy, and influence from the chirpings of robots and sensory artifice. After decades of human investment in will and perseverance, we have done so.

Far from being empty, the space between stars is filled with a gaseous breath -- a fiery exhalation of magnetized star dust. This breath, subject to nuclear and radiative pressure, is first blown from the surface of a star. It then threads through the local planets, breaking across them like water across river stones. Before it finally percolates from the solar system into the greater galactic milieu

From end to end and head to toe, the universe is filled with this bubbling, swirling, tonic of ionized star embers. It is only in realizing the full pervasiveness of this context, that is, the full pervasiveness of the vast space between stars, that we can begin to appreciate how fundamentally important what follows is to our understanding of everything.

What is Magnetic Reconnection?

Before we can talk about reconnection, we must talk about everything that it isn't. Like a description of a key is meaningless without the context of a lock, reconnection has no meaning outside of the greater context of a plasma universe. So we begin with a discussion where most things begin.

"We are all made of star-stuff."

It's an iconic quote by the inimitable Carl Sagan; the idea that our muddy, earthy selves can come from something as beautiful as a star has certainly captured the imagination of the general population. It evokes a certain poetic imagery -- a literal dust falling to the earth like sparkling dew or a rain of precious gemstones. In which each twinkling shard of light carries a living seed. The thing about this quote that is especially enchanting and especially clever is that it is absolutely true. And its truth reveals a ringing ubiquity far better than the poetic fantasy it inspires. It's not just that

we are star-stuff, but rather that all stuff is star-stuff. Everything on Earth from the mountain in its cloudy repose to the torpid ocean depths is star-stuff. Every flake of satellite, streak of comet, or puff of gas that can be found in the space above is star-stuff.

Besides guiding people toward some sort of cosmic nirvana, this little fact also gives insight into the physical nature of things. Most stuff out there came from a star. And stars, among other things, are known for being pretty hot places. When matter is first flung from a star, it is always in the plasma state. Unlike a backyard barbeque, where hot embers thrown from the fire mix with the cool air above and are themselves cooled, the embers thrown from a star have nothing to mix with. They are flung into nothingness. A nothingness so sparse of material, that even if the plasma is cooled enough to become ordinary matter once again, the tiny constituent particles within it cannot find each other in order to re-combine.

Planets, comets, meteors, and moons are ordinary matter. Everything else, everything in expanse between, is plasma. So, not only is the universe made of star-stuff. Most of it is still piping hot. We live in a plasma universe.

Plasma Behavior

The salient characteristic of a cloud of plasma drifting through space is that it's made up of independent charges. Charges which are free to answer the call of any electric field they feel. This means that if there is an electric field, the charges will move until they no longer feel an electric field. Being really small particles with incredible sensitivity to electric fields, they respond to this calling very quickly. With the ions and electrons zipping around in order to balance out any perceived electric field, we can see that from the perspective of the plasma, the electric field should be

zero (or quickly become zero). Although reality is more nuanced, we'll take this as our starting axiom in the discussion -- 'from the perspective of the plasma, the electric field is zero.'

It's important to note, that *perspective* is significant in this discussion. We are used to discussing electric and magnetic fields in our everyday life. Refrigerator magnets have magnetic fields. Electric fields drive current to our lamps and computers. We view these things as static external things. What is less popularly known about magnetic and electric fields is that their appearance can change dramatically depending on who is observing them.

This dependence of the system on the perspective of the observer is a relativistic affect of nature. The appearance of electric and magnetic fields is unique to a reference frame. Reference frames moving at different velocities will 'see' different field configurations. If we know the fields as measured from a particular observer, we can use the non-relativistic Lorentz transformation to predict what the fields would appear like in our own (or any other) reference frame,

$$\vec{E}' = \vec{E} + \frac{\vec{v} \times \vec{B}}{c},$$

$$\vec{B}' = \vec{B} - \frac{\vec{v} \times \vec{E}}{c}.$$

The primed variables in these equations represent the electric and magnetic fields from the perspective of the moving plasma. The un-primed fields on the right hand side of the equation represent the fields as measured in a distant reference frame observing the plasma moving at a velocity, $\vec{v}$. Although these equations are interesting and give great insight into the nature of the universe on their own, for our purposes they are merely stepping stones.

Combining this understanding of electric fields with what we know about plasmas leads us to a powerful interpretation of plasma behavior. If a plasma always adjusts so that from its perspective the electric field appears to be zero, then from our perspective the plasma will appear to move such that the electric field is:

$$\vec{E} = 0 - \frac{\vec{v} \times \vec{B}}{c},$$

$$\vec{E} = -\frac{\vec{v} \times \vec{B}}{c}.$$

The magnetic field, on the other hand, is not as fickle as the electric,

$$\vec{B} = \vec{B}' + \frac{\vec{v}}{\mathrm{c}} \times 0,$$

$$\vec{B} = \vec{B}'.$$

It stays roughly the same for all observers.

Taken together, we can see that the electric field is an expression unique to a particular observer. Since an observer can be moving at any speed relative to the plasma, there are an infinite number of possible electric fields which can be measured -- observers riding trains will see the plasma travelling at a different velocity than those riding bicycles and hence will observe different electric fields. No matter the mode of transportation of the observing reference frame, the plasma will appear to drift perpendicularly to the electric field and the magnetic field with a constant velocity.

When it comes to its velocity, a plasma behaves like any other thing. Its velocity is simply due to the relative motion between the observer and the plasma. Considering that the magnetic field stays the same for all reference frames, these facts beg the important question of whether or not the electric field is important to the

behavior of the plasma. As the premise of our question implies, it's not. In plasma physics, the electric field is generally considered a spectator variable. In other words, the magnetic field and the velocity are the primary drivers of the plasma dynamics throughout most of the universe. If we are to understand how plasma behaves in the universe, it is therefore logical to ask how magnetic fields behave in the universe.

To this aim, consider a blob of ideal plasma. By faraday's law,

$$\frac{\partial \vec{B}}{\partial t} = -c\vec{\nabla} \times \vec{E}.$$

We know that the magnetic field in the plasma cannot change without there being a spatial change in electric field. However, as we already discussed, our ideal plasma axiom denies the existence of any electric field within the body of the plasma (in its own reference frame). If there can be no electric field, then there certainly cannot be a changing electric field. Therefore the magnetic field cannot change within the body of a plasma.

This is not to say the magnetic field cannot change outside of the plasma. Our axiom puts no restriction on the behavior of the fields around or near-to the plasma. The magnetic field is free to change anywhere outside of the plasma body. Really, since there's more than just one plasma cloud in the universe, it's not simply 'the' plasma. It's actually 'a' plasma. There are many clouds of plasma in the universe and there is no reason to say that different blobs of plasma need have the same magnetic fields within them. Two different blobs separated in space may very well have two completely different albeit fixed magnetic fields within them. The curious question arises, "what happens should two blobs of plasma, each with differing magnetic fields, collides with one another?" Or perhaps, "can they mix or diffuse through each other, like an ordinary gas?" It would seem impossible to allow two different plasmas to mix

together without also mixing their magnetic fields at the same time. Mixing the fields should change them, so it should be forbidden.

Indeed, nature has shown that so long as the electric field remains zero in the frame of the plasma, different plasmas are forbidden from mixing. Such a plasma would be frozen to its magnetic field for all time. This understanding is a basic and fundamental concept in plasma physics. It's known as the 'frozen-in' theorem and is a powerful tool for understanding and predicting how a plasma will behave in many different environments.

Frozen-in Flux

One of the first insights to develop from the restrictions introduced by the plasma is that the magnetic field becomes stuck or frozen-in to any plasma that it threads through. Like hairs are caught in the tines of a brush, the plasma is stuck to the magnetic field. It's important to realize that this does not mean that one drives the other. Rather they serve to moderate each other. When some force causes the plasma to stir, the magnetic field will also stir. Likewise, if the magnetic field is pulled, the plasma will likewise be pulled. They move, bend, and stretch together. More rigorously stated, the frozen-in theorem says, "The magnetic flux through a loop travelling with the plasma does not change."

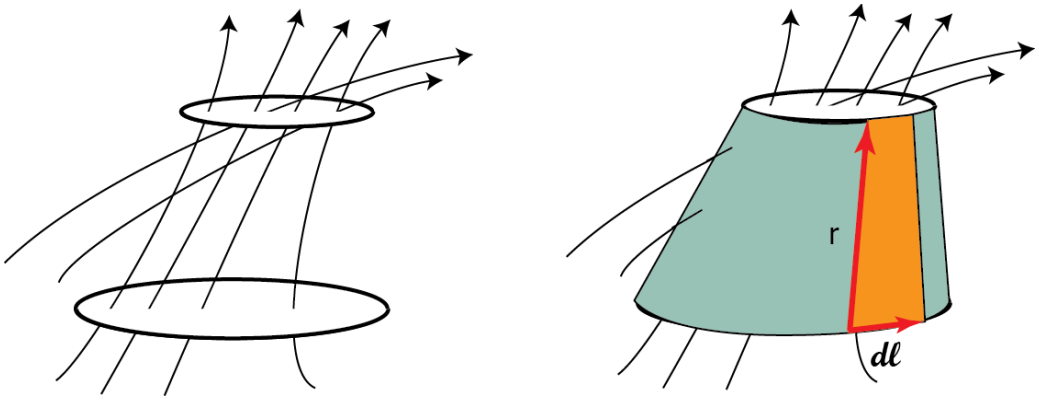

Figure 1 Two Amperian loops separated in space. The arrows represent the flux of magnetic field through the loops. Connecting the loops with a sheet allows us to quantify the flux shared by both loops.

To see a formal derivation of this, we consider the two loops depicted on the left in Figure 1. They clearly have different amounts of magnetic flux passing through them. By wrapping the two loops with a connecting sheet (the right half of the figure), we can divide this flux into two different categories. The flux they both share passes directly from one loop to the other staying within the boundary of the sheet. Any flux that they do not share must pass through the wrapping sheet. The flux passing through the sheet can be represented by the equation:

$$\phi_{sheet} = \oint_c \vec{B} \cdot (\vec{r} \times d\vec{l}), \qquad (1)$$

where $\vec{r}$ is a function of position along the loop and $(\vec{r} \times d\vec{l})$ is a surface element of our wrapping sheet.

This lets us then express the flux through the second loop in terms of the first loop and Equation (1),

$$\phi = \oint_c \vec{B} \cdot (\vec{r} \times d\vec{l}) + \oint_S \vec{B} \cdot d\vec{A}.$$

If instead of considering the loops to be separated in space, we consider them to be the same loop shown at two different times. In the intervening time, this loop has changed its shape in some way. Much the same as we did for the loops separated in space, we can calculate the flux shared between the loops separated in time. This allows us to represent the flux through the final loop as:

$$\phi = \oint_c \vec{B} \cdot \left(\vec{v}dt \times d\vec{l}\right) + \oint_S \vec{B} \cdot d\vec{A}.$$

Leading us to an expression for the change in flux in time,

$$\frac{d\phi}{dt} = \oint_c \vec{B} \cdot \left(\vec{v} \times d\vec{l}\right) + \oint_S \frac{\partial \vec{B}}{\partial t} \cdot d\vec{A}.$$

Using some basic vector calculus identities, we merge the two integration terms,

$$\frac{d\phi}{dt} = \oint_S \frac{\partial \vec{B}}{\partial t} \cdot d\vec{A} + \oint_c d\vec{l} \cdot \left(\vec{B} \times \vec{v}\right),$$

$$\frac{d\phi}{dt} = \oint_S [\frac{\partial \vec{B}}{\partial t} - \vec{\nabla} \times \left(\vec{v} \times \vec{B}\right)] \cdot d\vec{A}.$$

And by faraday's law,

$$\frac{\partial \vec{B}}{\partial t} = -\mathrm{c}(\vec{\nabla} \times \vec{E}),$$

$$\frac{\partial \vec{B}}{\partial t} = \vec{\nabla} \times \left(\vec{v} \times \vec{B}\right),$$

we demonstrate that the change in the magnetic flux through a loop travelling with the plasma is indeed zero:

$$\frac{d\phi}{dt} = \oint_S [\vec{\nabla} \times \left(\vec{v} \times \vec{B}\right) - \vec{\nabla} \times \left(\vec{v} \times \vec{B}\right)] \cdot d\vec{A}.$$

$$\frac{d\phi}{dt} = 0$$

As powerful of a tool as the frozen-in theorem is, it is clearly not the entire story. A plasma is still a gas. It follows that it should have gas-like properties, such as pressure and a temperature. It should be able to swirl, expand, or contract. It is in that vein that researchers have developed a special set of equations which merge the plasma concepts introduced thus far with some of the more classical ideas of gas behavior. The resulting equations are known as the MHD equations.

Magnetohydrodynamics

In order to understand the work that follows, a basic understanding of the usage of the MHD equations is more important than understanding their derivation. With that thought, we eschew their derivations and instead present them. The equations are expressed in terms of ρ and p, the plasma density and pressure, the velocity, $\vec{v}$, as well as the current, magnetic field, and electric field: $\vec{J}, \vec{B},$ and $\vec{E}$ respectively.

First we have an equation for the continuity of the plasma,

$$\frac{\partial \rho}{\partial t} + \vec{\nabla} \cdot (\rho \vec{v}) = 0.$$

This equation simply states that plasma cannot appear out of nothing, it must move from place to place. Following that, we have an equation for the acceleration of an element of plasma fluid due to the influences of both electromagnetic fields and pressure,

$$\rho \frac{d\vec{v}}{dt} = \frac{\vec{J}}{\mathrm{c}} \times \vec{B} - \vec{\nabla} P. \qquad (2)$$

In more basic physics terms, this is $m\vec{a} = \sum \vec{F}$. The next two equations,

$$\vec{E} = -\frac{\vec{v}}{\mathrm{c}} \times \vec{B}$$

and

$$\frac{\partial \vec{B}}{\partial t} = -c\vec{\nabla} \times \vec{E}$$

we discussed earlier. The top equation is the electric field as measured from an observer not travelling with the plasma. Below that is Faraday's law of induction. As we already discussed, together they gave us the frozen-in condition. Next up we have some basic identities from Maxwell's equations,

$$\vec{J} = \frac{c}{4\pi}\vec{\nabla} \times \vec{B}, \tag{3}$$

$$\vec{\nabla} \cdot \vec{B} = 0. \tag{4}$$

The first says that a current and a curling magnetic field are a coupled pair. When you have one, you will always have the other. The second equation says that a magnetic field cannot terminate or originate at a single point; tracings along the magnetic field must either spiral forever or be joined into loops. Finally we have the thermodynamic equation of state,

$$\frac{d}{dt}\left(\frac{P}{n^{\gamma}}\right) = 0.$$

This equation dictates how the gas responds to changes in temperature, pressure, and number density. Gamma can be tuned in order to allow the gas to behave according to well understood paradigms which best approximate environmental conditions. Some examples of these, would include the ideal gas equation assumed to be in the isochoric, isothermal, or isobaric states.

Together these equations describe the plasma universe, in the absence of magnetic reconnection. It's not practical to solve them without the use of computers in all except the most trivial of circumstances. So any discussion of them at this point

will be heuristic. In that manner, we've already discussed some of the MHD equations during our development of the frozen-in effect. In order to enrich our understanding of the universe, we now discuss the coupling between the electromagnetic and gas dynamics of the system; in other words, the force equation (2).

On the left hand side of this equation, we have a kinematic term -- the net force on an element of fluid plasma. On the right we have a complicated term involving the current, $\vec{J}$, and the magnetic field, $\vec{B}$. These are followed by a simple term involving the pressure, P. The ion equation of motion is the only equation in this set which involves the dynamics of both the gas and electromagnetic terms. By using the definition for the current from Maxwell's equation, we can begin to interpret the meaning of this equation. Using $\vec{J} = c/4\pi\vec{\nabla} \times \vec{B}$, we can derive

$$\rho \frac{d\vec{v}}{dt} = \frac{1}{4\pi}\left(\vec{\nabla} \times \vec{B}\right) \times \vec{B} - \vec{\nabla}P,$$

$$\rho \frac{d\vec{v}}{dt} = \frac{\left(\vec{B} \cdot \vec{\nabla}\right)\vec{B}}{4\pi} - \vec{\nabla}\left(\frac{B^2}{2}\right) - \vec{\nabla}P,$$

$$\rho \frac{d\vec{v}}{dt} = \frac{\left(\vec{B} \cdot \vec{\nabla}\right)\vec{B}}{4\pi} - \vec{\nabla}\left(\frac{B^2}{8\pi} + P\right).$$

Recasting the equation of motion in this form makes it easier for us to interpret. The most straight forward term is on the far right. We see that the magnetic energy, $(1/8\pi)B^2$, comes into the equation in the same way that the pressure does. This means that an element of fluid will respond to a region of intense magnetic field in the same way that it would respond to a region of intense gas pressure. We call these two terms together the total pressure. The contribution from the magnetic term alone is called the *magnetic pressure*. Just like a high pressure gas could pop the top

off of a soda bottle, a high magnetic pressure could pop the top off of a bottle containing a plasma. If we ignore the first term completely we find,

$$\rho \frac{d\vec{v}}{dt} = -\vec{\nabla}\left(\frac{B^2}{8\pi} + P\right),$$

$$0 = -\vec{\nabla}\left(\frac{B^2}{8\pi} + P\right).$$

We can see that the system will move until the term on the right is equal to zero. This occurs when the sum of the magnetic pressure and gas pressure are the same everywhere. This is called *pressure balance*.

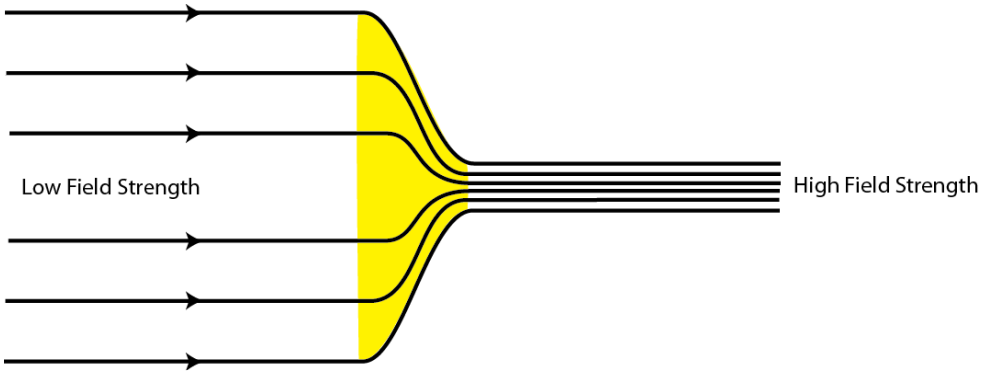

Figure 2 A transition between a weak magnetic field (on the left) and a strong magnetic field (on the right). In the middle, highlighted in yellow, is the transition region where $(\vec{B} \cdot \vec{\nabla})\vec{B}$ is large.

Next we switch our attention to the first term in the force equation, $(\vec{B} \cdot \vec{\nabla})\vec{B}/4\pi$. This term represents the change in the magnetic field as you travel along the magnetic field. Because there can be no divergence in the magnetic field, Equation (4), the intensity of the magnetic field cannot simply change as you travel along it. Its intensity must develop as a consequence of a bend in the travel path, like in Figure 2.

If the magnetic field makes a sharp change in direction at some point in space, this term will be large. In other words, plasma in regions where the magnetic field changes directions rapidly will experience a force -- a force which will tend to un-bend the field. We call this force a *magnetic tension*.

Taken together, the plasma will move such that the pressures become balanced while at the same time smoothing out bends in the magnetic field.

In order to build on this, we look at the case of an elliptical magnetic bubble (Figure 3). Initially the right and left ends of the bubble are very bent. The force equation told us that this bubble will attempt to smooth out the bends in its magnetic field. It will move the plasma in the bubble until it is circular. If the bubble had some initial magnetic field, $\vec{B}_0$, there will be an initial magnetic flux, $B_0 a$, and an initial magnetic energy, $\frac{1}{8}B_0^2(ab)$. Likewise after the change in geometry there will be a final magnetic field, flux, and energy of: $\vec{B}_f, B_f R$, and $\frac{1}{8}B_f^2(R^2)$.

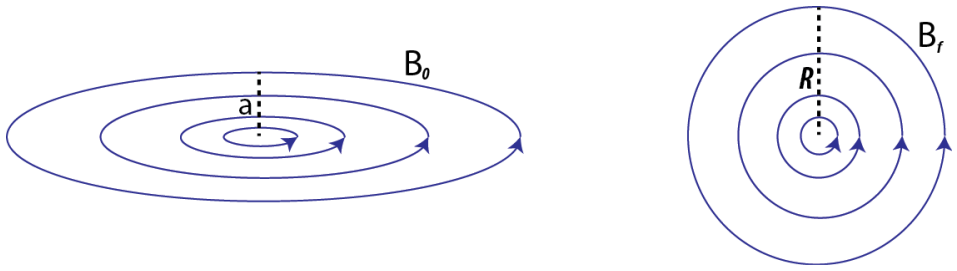

Figure 3 A magnetic bubble before (left) and after (right).

In order to isolate the affect caused by the change in shape, we assume that the bubble is incompressible and so stays the same size, $\pi ab = \pi R^2$. And since it's a plasma we know that the magnetic flux through the plasma must remain constant,

$B_0 a = B_f R$. Using these we can find the ratio between the final and initial magnetic energy,

$$\frac{\mathcal{E}_f}{\mathcal{E}_0} = \frac{\left[\frac{1}{8} B_f^2 (R^2)\right]}{\left[\frac{1}{8} B_0^2 (ab)\right]},$$

$$\frac{\mathcal{E}_f}{\mathcal{E}_0} = \frac{[B_f^2]}{[B_0^2]}.$$

Combining our initial assumptions we find that, $B_f^2 = B_0^2 \frac{a}{b}$ and substituting that in gives,

$$\frac{\mathcal{E}_f}{\mathcal{E}_0} = \frac{a}{b}.$$

The magnetic energy has been reduced by a factor of a/b. Without delving into the semantic black hole of questioning whether or not magnetic fields *can* do work, we point out that initially we had some amount of magnetic energy. At a later time we had less magnetic energy and from the plasma equation of motion, we can see that work will have been done on the plasma. Surely, there is some complex microphysics, intermediary electric fields, or distant dynamos which are *truly* responsible for the work being done. We, however, are going to simply say that it was the magnetic field that did the work, just like we prefer to say that cars take us from one place to another, in lieu of attributing the engine or fossil fuels.

More important than a debate about language is an understanding of how the plasma is behaving. The tension in the magnetic field was the mechanism by which energy could be transferred from the field into the plasma. The tension itself holds no energy. It is the intensity of the magnetic field which holds the energy. So we can identify that highly stressed, bent, or twisted fields are fields which are capable of

releasing magnetic energy into the plasma through an unbending process. This process will result in a reduction of the magnetic field intensity. It's often said that a sphere is the most efficient way of packing things in a space given a radius. Something similar apparently holds true for magnetic fields. Spherical magnetic bubbles are able to pack in the most magnetic flux while using the least amount of energy.

Logical End of the Universe

Recall that our purpose in presenting this introduction to plasma physics was to present context. Let's consider the universe without magnetic reconnection. Hot stars spew magnetized plasma into the emptiness of space. Stars, like our Sun, are quite inhomogeneous on the surface. They have hot spots, cool spots, and spots of varying magnetic fields. With so much variance, the plasma is inevitably frozen-in to the topology of its origin. Married forever to those origins, ropes of plasma extend across the surrounding space. Forbidden from mixing, they twist around each other and drape across magnetized planets. They run abut to and push against the encapsulating plasma of the greater galaxy. Dynamos within the cores of adjacent stars and planets continue to churn, generating more and more magnetic flux. This relentless production of magnetic energy will begin to tighten everything like an over-wound rubber band. Planets will squeeze stars. Stars will squeeze each other. And space will become a gridlock of twisted magnetic ropes, filling the emptiness with ever-growing sheets of current and bubbles of escalating plasma pressure. Eventually the honeycomb labyrinth of frozen magnetic domains will invade the cores of the stars themselves, seizing the very dynamos responsible for fathering them -- ending the Universe as we know it.

With great satisfaction, plasma physicists often say that 90% of the universe is perfectly described by this model. Astute readers will perhaps find some flaw with it. Subtle things, such as being alive, betray the truth of the matter; there's something very important in the remaining 10%.

Magnetic Reconnection

Built within the framework of MHD is the strict idea that the electric field must remain zero within the reference frame of the plasma. We argued that this was true because the sensitivity and sizes of the charges allowed them to 'very quickly,' adjust to any internal electric field. However, the charges, being real particles with real masses, have real constraints on them.

The most obvious constraint to anyone familiar with terrestrial electronics is the idea of resistivity. More universally, the concept would be familiar anyone who has attempted to walk through a crowded plaza. They will understand that high densities (crowded plazas) or high temperatures (running children) could affect their ability to traverse the plaza. It is likewise with plasma dynamics. Like ourselves, the particles in a plasma sometimes have trouble moving around because they keep bumping into things. If the charges are bumping into each other or into ambient neutral species, they will not be able to respond quickly enough to neutralize the electric field. Instead of happening 'near instantly,' the flow of charge in response to the electric field will become a part of the relevant dynamics,

$$\vec{E} = -\vec{v} \times \frac{\vec{B}}{\mathrm{c}} + \eta \vec{J}.$$

When the MHD equations are modified to include the effect resistivity on the plasma, they are called the *resistive-MHD equations*. When the current becomes

strong, this added term will begin to play a larger and larger role in the dynamics of the plasma.

Another important and commonly used modification to the electric field is the Hall effect. This effect is more subtle than simple resistivity. Plasma species are made of charges of different masses. In the simplest case, this is usually taken to mean protons and electrons. In practice it could be a more complex pairing such as triply ionized oxygen and electrons. Whatever the plasma species, the mass becomes relevant when you consider the mechanism by which charges couple to the magnetic field. Charges, even when they are drifting in a frozen-in state do not simply drift with the field. They gyrate around it. The more massive charges, like protons or triply ionized oxygen, gyrate more slowly and at greater distances from their gyration center than their smaller counterparts. More massive species will thus sample the magnetic field from a larger area of space. This large sampling area will make the heavier species respond to the magnetic field differently than the lighter species. As the plasma species respond differently, they will move differently. The disparate motions that develop will produce an internal electric field. In order to express this mechanism in a hydrodynamic way, we add another term to the electric field equation,

$$\vec{E} = -\vec{v}_i \times \frac{\vec{B}}{\mathrm{c}} + \eta\vec{J} + \frac{1}{nec}\vec{J} \times \vec{B}.$$

When modified to include the Hall term, the equations are redubbed, the *Hall-MHD equations*. In this extra term, *n* is the number density of the particles and their electric charge is represented by *e*. Since we have broken the parity of the two charges, we have also introduced the idea that the plasma is actually comprised of more than one fluid by changing $\vec{v} \rightarrow \vec{v}_i$, meaning the ion velocity. Like the resistivity term, the Hall term begins to be a major player in the dynamics where there is a strong current.

Revisiting our doomed plasma universe, the strict adherence to the frozen-in condition painted a picture where stressed magnetic field lines twisted and bent about each other in an eternal state of contention. Now, however, something interesting occurs. And it occurs exactly at these magnetic stress points. Where magnetic flux ropes press against each other, strong sheets of current will naturally develop from Equation (3). The more tightly they are pressed against each other, the stronger the current sheet separating them will become. There will eventually come a point where the dynamics of the plasma will no longer be dominated by the $\vec{v}_i \times \vec{B}/c$ term, but instead will be dominated by the resistive or Hall terms. This will liberate the plasma from the magnetic field and break the frozen-in condition. With the plasma no longer married to the magnetic field, gas and magnetic flux will be free to mix around regions of intense current. These mixing junctions become a locus around which the magnetic field can reconfigure itself, reducing its tension and dissipating some of the energy it carried. Instead of ending in a gridlock, the Universe will find a balanced equilibrium. The dynamos within stars and planets will continue to spool magnetic energy out into space. Contending flux ropes of frozen-in plasma will pile up until the stress transforms the region into a local mixing junction. Then those junctions will serve as transfer terminals for the plasma and magnetic fields, connecting them to the greater universe through a never ending magnetic interchange network. This interchange mechanism responsible for unlocking plasma gridlock is called *magnetic reconnection*. And it's as integral to a plasma universe as a door is integral to a house.

In fact, reconnection enjoys a similar ubiquity as doors do in houses. Wherever there is a magnetic domain, there often will be a mixing junction connecting it to an adjacent domain. It's found at every length scale from the miniscule to the

massive. Reconnection creates these mixing junctions, where it is theorized that rapid and dramatic field line reconfiguration contributes to the energization of solar flares [60]. It appears in the emptiness between planets -- long and extended mixing regions develop among the lonely weaves of the solar wind [46] [47]. Terrestrial and Solar plasma resolve their conflict in a cascade of reconnection events around the Earth's magnetic bubble, beautifying our lives with the polar auroras [17]. Reconnection is even found in the turbulent aftermath of those magnetic storms, enabling a cascade of eddies and whorls from large to small [35] [56].

Introduction to Research

The first successful model of magnetic reconnection grew out of an attempt to explain the magnetic structure and rapid energy release of Solar flares. This model, developed by Sweet and Parker, demonstrated that magnetic energy could be converted into plasma kinetic energy through a magnetic mixing region or diffusion region. This simple 2D model for magnetic reconnection is now called the *Sweet-Parker scaling model* [44]. Unfortunately, the conversion of magnetic energy into plasma flow energy was not rapid enough to explain the explosive energy dissipation observed in solar flares [8].

Not long after, a model developed by Petschek demonstrated that if the aspect ratio of the diffusion region could remain small, then reconnection would process magnetic flux at a rate sufficient for flare-like energy release [45]. The key word in the phrasing was, "if." Petschek proposed no mechanism which would cause the diffusion region to remain small.

Over thirty years later, work begun by Biskamp et al. and further developed by the plasma physics community lead to a magnetic reconnection model which naturally produced small diffusion regions and rapid magnetic energy conversion. Relying on the Hall term to decouple the ion and electron behavior in the diffusion region, this model was therefore called a *collisionless two-fluid model* ([6] and references therein). With its development, the idea that the Sun's magnetic field could drive the explosive release of energy observed in flares had come to fruition [32]. Furthermore it allowed observed reconnection to more generally be used to explain plasma

energization near the Sun, the Earth, and within the IMF. Our modern understanding of magnetic reconnection has grown from its successes.

The collisionless model, like its predecessors is a 2D model designed to explain the energy conversion rates around magnetic mixing regions. To that end, it has been wildly successful. However, a cursory inspection of the mixing regions observed in nature show that their 3D geometries can vary wildly. Near to the Sun, reconnection occurs across arcades of twisted magnetic loops [61]. At the bow-shock, where the Earth and Sun's magnetic field meet, the mixing region curves across the structure of the Earth's dipole, [15]. Even here on Earth, laboratory plasmas, such as Swarthmore's Spherical Experiment (SSX), reveal a forest of interplay between the in and out-of-plane dimensions [11] [14]. A simple extension of the planar 2D collisionless model into 3D would be missing these and other complexities.

One approach taken is a top-down attempt to describe 3D reconnection by deconstructing the magnetic topology into its basic constituents. In these types of studies, magnetic reconnection develops as an outgrowth of the structural necessity of the system's magnetic spines, nulls, and fans [29] [15] [51]. One of the challenges to this approach is that it has proven difficult to find a 3D equilibrium state amenable to computational study.

A more bottom-up approach is to work from the success of the 2D reconnection models. Although reconnection in the Sun, solar wind, and day-side bow shock are all structurally complex, reconnection in the magnetotail occurs within the laminar wake of the planet [36]. There, opposing magnetic flux in the tail collides across long extended current sheets. These sheets are reminiscent of the 1D current sheet equilibriums used in 2D models and 2D simulations. As such, magnetotail

reconnection is naturally well described by the 2D approximation. One of the aforementioned successes of reconnection is that it was able to explain the presence of global plasma flows during substorm events [30] [51].

Despite the success of these 2D models at describing global magnetic reconfiguration, there are aspects of magnetotail flows which are not well understood. In addition to global flows capable of reconfiguring the whole magnetotail, a spectrum of more localized plasma flows have been observed [5] [2] [1] [16] [38]. Transient events lasting 1-10 minutes achieving velocities of 400 km/s or more are termed bursty bulk flows (BBFs). While being unable to drive global magnetotail reconfiguration, BBFs are still an essential and widespread phenomenon in the magnetotail and are thought to contribute significantly in the flux transfer between the tail and the Earth [1]. Observed to be 1 R_E in extent in the north-south direction and spread as long as 3 R_E along the current sheet [37], the presence of these BBFs strongly implies the existence of bursty magnetic reconnection in the near magnetotail. So, not only does reconnection come in a variety of forms in nature, the impact of reconnection on the local magnetosphere has been shown to have some sensitivity to the reconnection structure. In a survey of BBF events, Ohtani et al., found that only a fraction of observed reconnection events are able to create outflows which penetrate deep into the near earth magnetosphere [40]. Following that, [13], [7], [16], showed that this penetration was directly correlated with the outflowing island entropy.

Magnetic reconnection is one possible mechanism for driving these smaller flows. From a basic reconnection standpoint, the question becomes: will a 3D model of reconnection realize the different flavors of plasma flow observed in the magnetotail?

Since the magnetotail presents an equilibrium state which is easily extensible into three dimensions, a few studies of this nature have already been done. Shedding some light on the asymmetric x-line growth in the near magneto-tail, *Huba and Rudakov* as well as *Shay et al.* found in simulation that the reconnection propagated in the direction of the electron flow [28] [59]. While *Shay et al.* introduced the concept of a solitary x-line while offering the refinement that reconnection will grow in the direction of the current carrying species [59]. The discovery of the solitary x-line suggests that reconnection is indeed able to produce plasma flow events localized in space. In 2006, kinetic simulations done by *Lapenta et al.* [33] demonstrated that the out-of-plane growth rates of the reconnection region had a dependence on the initial current sheet width, mass ratios, and initial temperatures. Further work by *Huba and Rudakov* [27] correlated the asymmetry of the growth direction with a $\vec{B} \times \vec{\nabla} n$ wave, giving some insight into the possible micro-scale physics driving the gross phenomenon.

These studies strongly suggest that the smaller plasma flow events observed in the magnetotail can be the result of magnetic reconnection. However, there remain unresolved questions. The transient nature of BBFs has still been undiscovered in reconnection simulations; 2D reconnection was both theorized and observed in simulation to always grow until it had consumed all of the available magnetic flux ([6] and references therein). The ability of reconnection to explain smaller plasma flows hinges upon the discovery of a termination mechanism. Also unresolved was an explanation of the observed size of the BBFs. In 2004 Nakamura et al. used Cluster data to establish that the extent of these smaller BBFs was between 2-3R_E [37]. Previous work has no explanation for this limitation.

In this thesis, we provide evidence for this behavior in a reconnection simulation. As well as introduce a 3D scaling model for reconnection which explains the physical mechanisms behind the behaviors.

Reconnection Structure

Magnetic reconnection is a magnetic mixing process which occurs in the collision zone between magnetized clouds of plasma. When the current between the two clouds grows strong enough, a plasma diffusion region develops between them. In a very dense plasma where collisions happen frequently, this development can be due to those same collisions interfering resistively with the current flow.

In more airy plasma clouds, where collisions happen far too infrequently to affect the dynamics, a different mechanism is responsible for separating the behavior of the ions and electrons. As mentioned before, the charges gyrate around the magnetic field. This causes their behavior to be derived from a sampling area within their gyro-radius. In the abutment of opposing magnetic fields, the charges will sample an area of space which has a net magnetic field of zero. This essentially de-magnetizes the plasma. The ions incident on the collision zone, having a larger gyro-radius, sample the opposing magnetic field first. This results in them de-coupling from the magnetic field before their less massive siblings.

The de-magnetization length scale of the ions defines the width of the diffusion region. In a fluid sense it is called the ion-inertial length, it is:

$$d_i = \frac{C_A}{\Omega_{ci}} = \frac{c}{\omega_{pi}} = \left(\frac{m_i c^2}{4\pi \mathrm{n} e^2}\right)^{1/2}.$$

Similarly, an electron diffusion region is created of the size of the electron inertial length,

$$d_e = c/\omega_{pe.}$$

Numerical simulations by Shay et al. have confirmed these length scales [57].

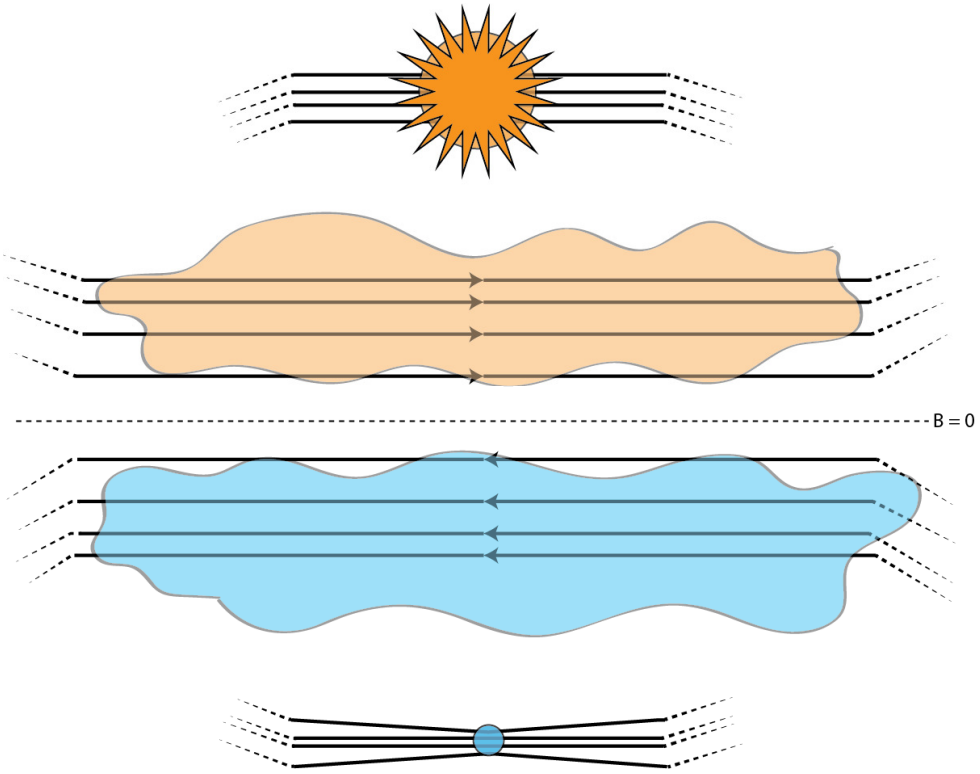

Figure 4 Collision region between two topologically distinct plasmas shown in blue and orange. The magnetic flux is represented by the solid field lines. Dashed lines connect the flux to their distant foot prints. Between the two plasmas a current sheet forms around the B = 0 magnetic null sheet.

Before the onset of reconnection, the structure of the current sheet appears like Figure 4. In the collision space between the plasmas, the opposing field lines must have a null-sheet between them. The two sets of plasma are considered topologically distinct. The magnetic field approaching the current sheet from the top threads a

completely different plasma than that of the bottom. If this were reconnection between Sun-born plasma and Earth-born plasma, the magnetic field originating at the top of the figure would have footholds on the Sun, while the magnetic field originating on the bottom has Earth-bound foot prints.

Soon after the formation of a diffusion region, the structure in Figure 5 will form. We see that in addition to the two originating topological structures, there are now two child topologies. These fields are of mixed origins - one foot on the Sun with the other foot on the Earth. Squeezed between these four magnetic domains is what remains of the magnetic-null. Originally a sheet, it has now become a null-point. Stretched into the 3rd dimension, this point is called the *x-line*. It is around this line, through the diffusion region, that reconnection is said to occur.

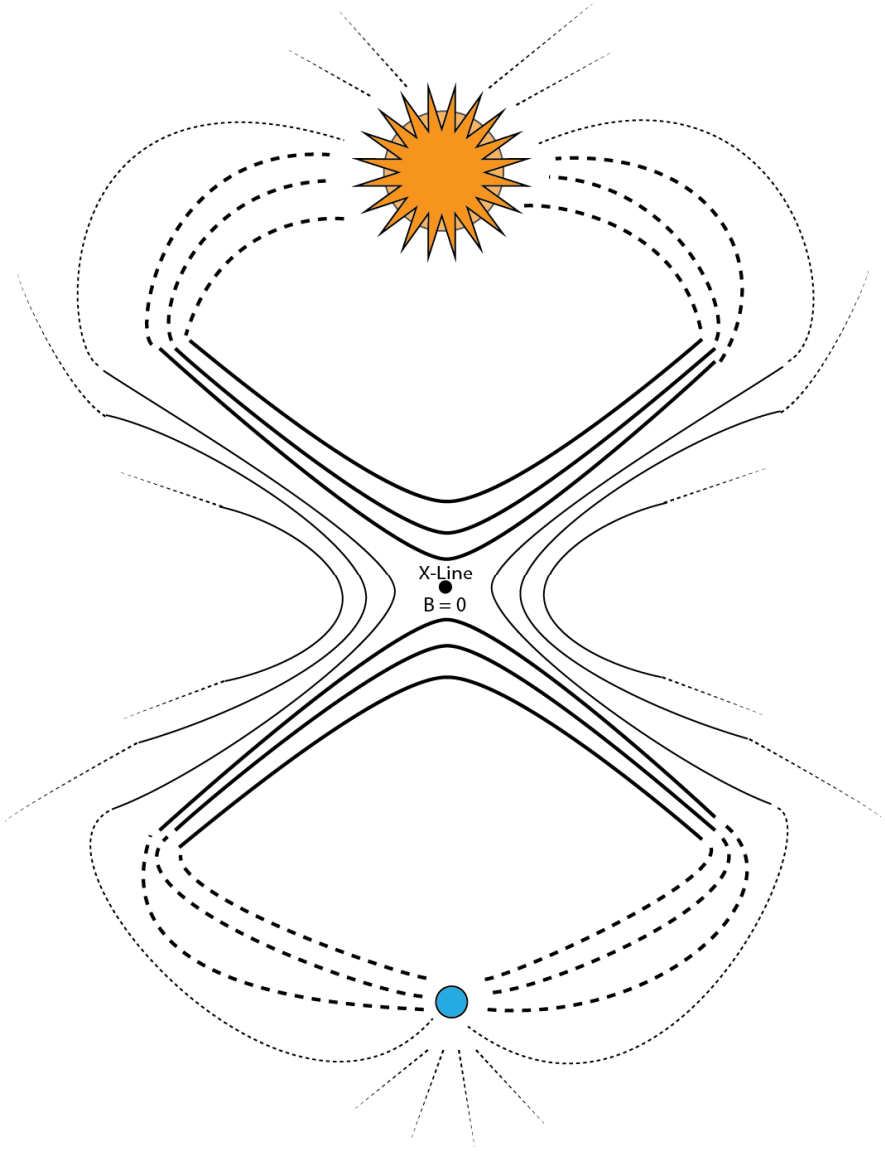

Figure 5 Structure of the collision region between two different plasmas after the onset of magnetic reconnection. Reconnection occurs around a center magnetic null, the x-line. This line, seen head-on, extends some distance into and out of the page. It separates the four different magnetic topologies.

The traditional viewpoint of a reconnecting x-line is represented by Figure 6. Once again, at the top and bottom of the figure there are magnetic field lines with opposite polarity colliding about a center sheet of current - directed into the page. The strength of the current depends heavily on the separation between the magnetic field lines. Places where the separation is wide (the left and right sides of the figure), the magnitude of the current is relatively weak. In region where the magnetic field pinches in, the current can become quite strong. Within the most pinched part of the current sheet, we find the diffusion region. Plasma flux enters the diffusion region from the top and bottom of the figure. Once inside the diffusion region, the plasma decouples from the magnetic field. After decoupling, the plasma is free to mix and the magnetic field undergoes its topological transformation. The change in topology leads to the creation of highly curved magnetic field lines within the current sheet. Behaving much like a stressed spring, the magnetic field attempts to unbend away from the pinched section of the current sheet. On its way out of the diffusion region, the plasma is once again frozen into the magnetic field and they are both accelerated away together.

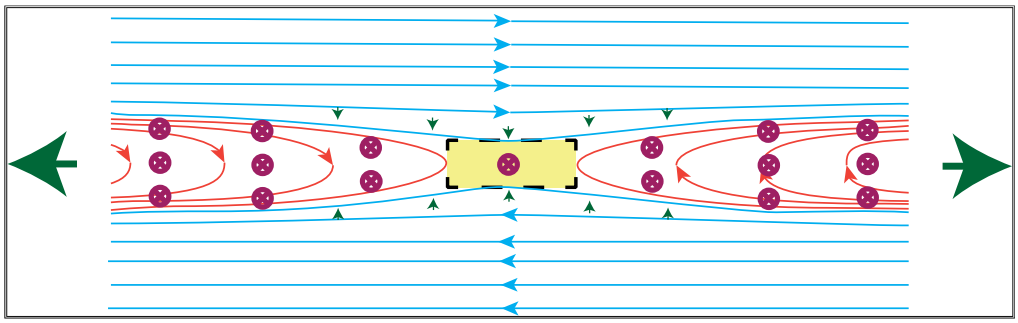

Figure 6 Close up view of the magnetic collision region during reconnection. Plasma flow is represented by green arrows. The magnetic flux being carried with the plasma into and out of the x-line is represented by blue (incoming) and red (outgoing) lines. In yellow, surrounding the region of the x-line is the diffusion region. Finally, the maroon markers depict current flowing into the page.

As a general rule of thumb, the fully-formed system obeys the concept of 'what goes in, must come out.' As such, the rate that plasma leaves the system and the rate that plasma enters the system is intimately coupled via the aspect ratio of the diffusion region. Anyone who has driven on an interstate as it narrowed from 4 lanes to 1 lane should have a very intuitive grasp of this relationship. Traffic slows down when the number of lanes abruptly drops. Likewise, if the inflow edge of the diffusion region is much bigger than the outflow edge, then the inflow will have to greatly slow itself to accommodate the limited outflow capacity.

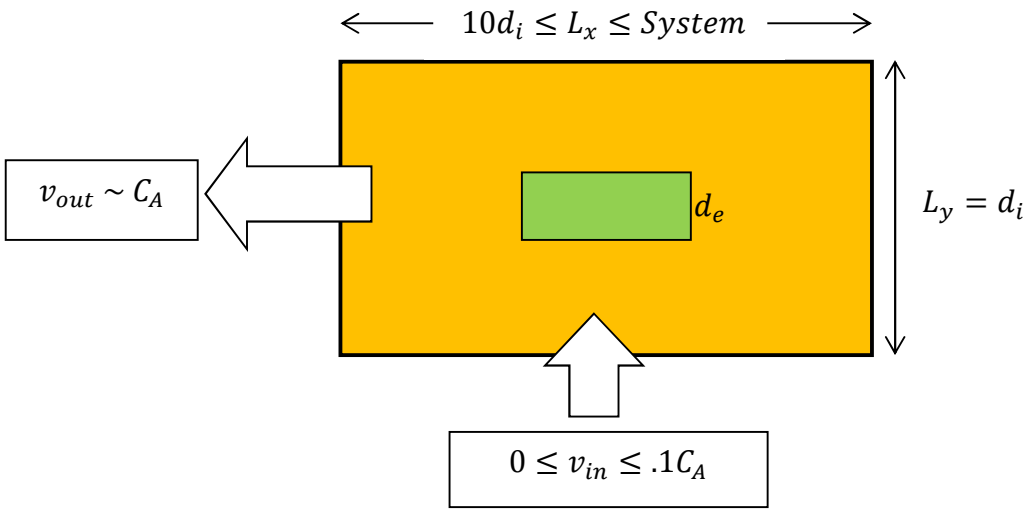

Figure 7 Dimensions of the diffusion region. The ion diffusion region is drawn in yellow while the electron diffusion region is drawn in green. The plasma inflow and outflow are closely related to the dimensions.

To see this, we actually balance of the inflow and outflow in a steady state assumption. The two quantities usually considered are the plasma matter itself, because of the continuity condition as well as the energy flow. The continuity equation says that the amount of plasma passing through the top of the diffusion rectangle should equal the amount of plasma leaving through a side.

$$\rho v_{in} L_x = \rho v_{out} L_y,$$

$$\frac{v_{in}}{v_{out}} = \frac{L_y}{L_x}.$$

For the energy flux, the inflow is slower than the outflow by a ratio of L_y/L_x, so the majority of the inflowing energy is being carried by the incoming magnetic flux. While the outflowing energy leaves while being constrained to the current sheet, which has depleted magnetic field strength. This means that the energy balance is

mostly a balance between the incoming magnetic energy and the outgoing kinetic energy. Using,

$$\frac{B_x^2}{8\pi} v_{in} = \frac{1}{2} m_i n v_{out}^3,$$

and the continuity equation we find that the outflow speed is,

$$v_{out}^2 = \frac{B_x^2}{4\pi\sqrt{m_i n}} = C_A^2.$$

This outflow speed is the equilibrium Alfven speed. Resulting in,

$$v_{in} = \frac{L_y}{L_x} C_A = \frac{d_i}{L_x} C_A$$

Simulations have shown that for Hall reconnection L_y/L_x has a roughly fixed ratio 0.1 [58] . And for resistive-MHD simulations, L_x has been shown to scale with the system size. This means that Hall reconnection in nature will have an inflow speed of $.1C_A$ regardless of the overall system size. Evidence of this ratio has also been observed in 3D experiments [10]. The basic structure of the diffusion region can be seen in Figure 7. Since laminar resistive reconnection will allow L_x to grow very large, it can have very slow inflow speeds in nature.

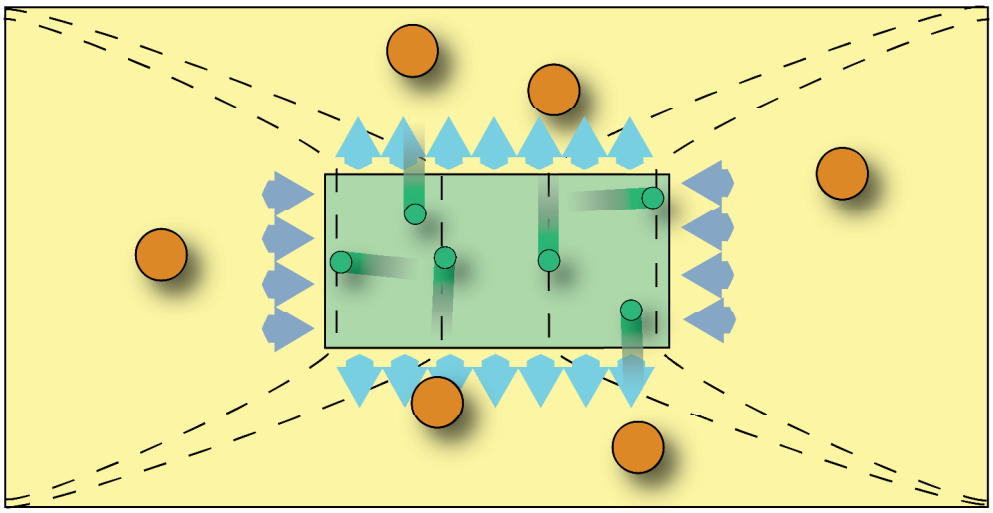

Figure 8 Two-fold structure of the diffusion region. Once again, the ion diffusion region is in yellow and the electron diffusion region in green. The dashed lines represent the magnetic field structure. Protons and electrons are present as orange and green circles. The electrons are carried by the magnetic field into the electron diffusion region, distinguishing their bulk motion from the protons. As a result of this difference in motion, an electric field arises, seen as blue and purple arrows.

The diffusion region itself has a two-fold structure [Figure 8]. The plasma is minimally made up of two different species of charges, a positive charge (large orange dots) and a negative charge (small green dots). Typically these are electrons and protons. Owing to their large differences in mass, they tend to decouple from the magnetic field under different conditions. The electrons being much lighter are carried with or stick to the magnetic field quite a bit more faithfully than the ions. This means, that when the plasma enters the diffusion region, it is the ions which break away from the magnetic field first, while the electrons continue to be carried deeper into the diffusion region.

The two different charge species moving with different velocities can be represented by a current flow into or out of the diffusion region. Since it is typically the negatively charged particles which lead the way into the diffusion region, the resulting current points away from the diffusion region on the inflow and toward the diffusion region on the outflow. Subsequently, as the ions enter and leave the diffusion region, they are driven by this smaller current in the direction of the greater current. This can be seen from the force equation on the ions,

$$\vec{F}_i = e\left(\vec{E} + \frac{\vec{v}_i}{\mathrm{c}} \times \vec{B}\right),$$

$$\vec{E} = -\frac{\vec{v}_i}{\mathrm{c}} \times \vec{B} + \frac{\vec{J}}{\mathrm{nec}} \times \vec{B},$$

$$\vec{F}_{\mathrm{i}} = \frac{\vec{J}}{nc} \times \vec{B}.$$

Typically, this behavior by the ions is considered negligible in 2D studies of reconnection. However, for 3D reconnection this affect will become important.

Meanwhile, the electrons are carried with the pre-existing current in the out of plane direction. Since they are still tied to the magnetic field, as they are carried, they pull the magnetic field with them. This dragging of the field lines is sometimes alternatively viewed as being derived by the aforementioned current deforming the field line between the electron and ion diffusion regions. Regardless of the description, this results in what is often referred to the quadrupole nature of Hall reconnection in 2.5 dimensions, depicted in Figure 9. The stretching of the field line out of the plane enhances the reconnection rate, as the speed at which the magnetic field can rotate back into the plane is controlled by whistler physics, which tends to be greater than the speed at which the magnetic field can unbend. However, as is

depicted in the figure, this out of plane rotation does result in an over-shoot further downstream near the o-line.

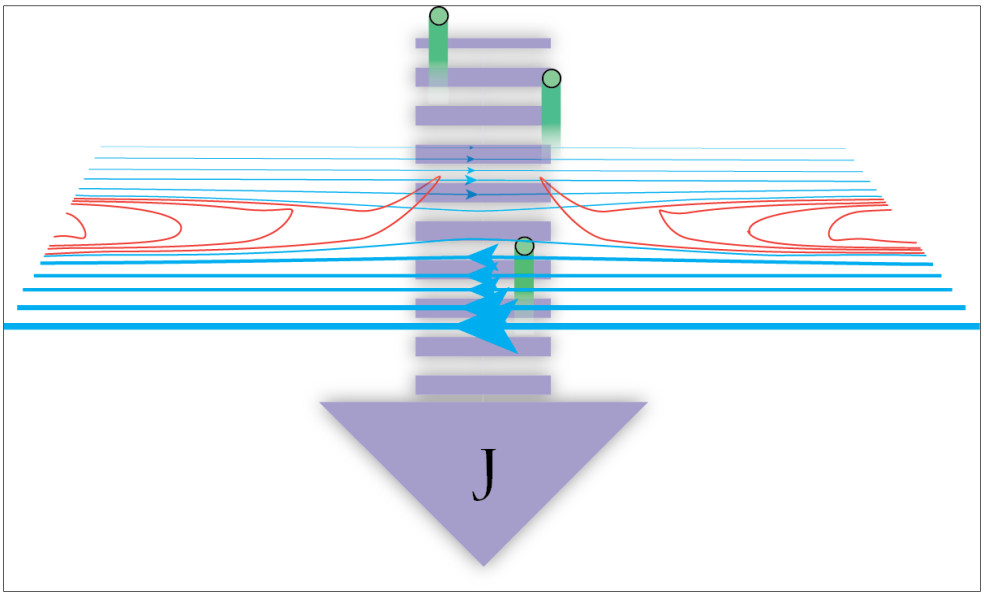

Figure 9 Quadrupole nature of magnetic reconnection in 2.5 dimensions. The outflowing magnetic field (red) is pulled out of the reconnecting plane by the moving electrons (green dots). The resulting magnetic structure is quadrupolar in nature and is considered a signature of collisionless reconnection.

As comfortable as steady state analysis of reconnection is, real reconnection is not steady state. Reconnection sites evolve both in time and in space. Shown in Figure 10, the system can be observed to be in one of several states. Initially, before the onset of anything that can be called reconnection, the magnetic flux must be brought together -- forming an ever narrowing current sheet. Once the current sheet has narrowed enough so that some physics can begin to violate the ideal conductivity of the system, magnetic flux will begin to be processed and reconnected by a diffusion

region. Initially, the diffusion region begins in a long and narrow configuration. This configuration tends to scale with the system size and the conversion of magnetic flux between the different domains tends to be 'slower.' In time, however, the contact point between the opposing magnetic fields will inevitably change from a system-sized line to one of approximately $10c/\omega_{pi}$ in width. At this juncture, the x-line has generally not yet reached its full potential. It's not until later, when the outflow jets have opened up, as seen in panel 4 of the figure, that the reconnection site is considered to be operating at full capacity.

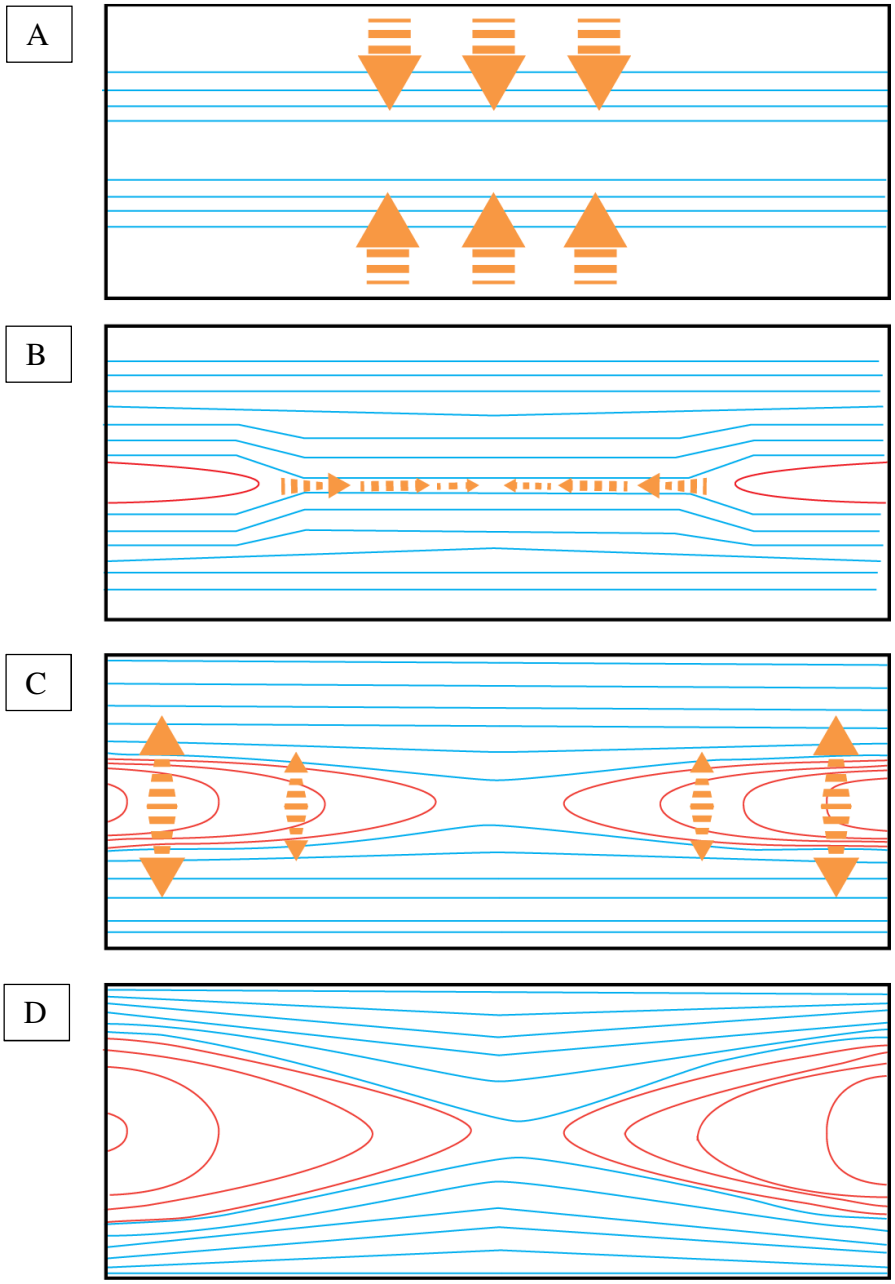

Figure 10 Magnetic reconnection structure as it evolves in time. Panel A: before the onset of reconnection, the current sheet narrows. Panel B: the diffusion region width L_x shrinks as the reconnection transitions from a Sweet-Parker like structure to a more Petschek-like structure. Panel C: the outflow nozzle opens, transitioning the reconnection to its final structure, seen in Panel D.

With a basic understanding of what traditional reconnection looks like 'in the plane,' we can now rotate out of the that plane into one which gives better insight into the mechanism of 3D reconnection. For most of this thesis, we will be inspecting the physics within the plane of the current sheet instead of the reconnecting plane. Prominent in this sheet is the region of enhanced current found inside of the diffusion region. From the rotated perspective, this region of enhanced current takes on the appearance of a current ribbon which shadows the x-line. Figure 11, shows this current ribbon in perspective a relative to the traditional picture of reconnection.

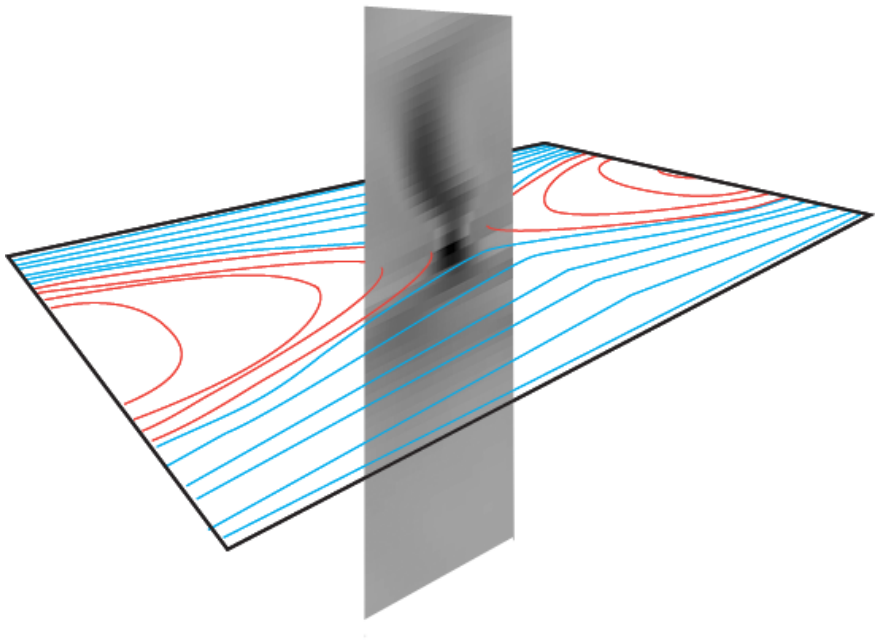

Figure 11 A ribbon of current in the out-of-plane direction taken from simulation and placed into the context of the 2D reconnecting plane. This current ribbon defines the plane in which most of the analysis for this thesis takes place.

Chapter 2

SIMULATIONS

Now that we are familiar with the basics of 2D reconnection, we lay the foundation for our study of 3D reconnection. Firstly, the study is based on simulation. It follows that we discuss the computational framework before we introduce results based on simulated data. Also, the work being based on a simulation has quite a few subtle consequences. The most important consequence is that simulated reality is not the same as physical reality. Simulations are crafted around a set of rules meant to reproduce certain aspects of reality. Some of the rules are chosen for investigative purposes while others are chosen in compromise with escalating computational costs. Whatever the case, care must be taken to not inject paradigms into the interpretation of the simulation which are not innately there. For example, in a fluid simulation particles do not exist. It would therefore be inappropriate to describe any of the physical phenomenon observed in a fluid simulation via particle kinematics. To do this would be akin to discussing what type of transmission is present in a toy Hot Wheels car. Whenever we are discussing the behavior of the simulation, it must be in the context of the simulation rule set.

The second subtlety to consider is derived from the numerical methods by which the simulation rules are solved. At some level, computational work must always have its results rounded-off. Exactly how and to what degree is determined by the necessity of balancing quality against efficiency. We do this every day when we work with numbers. Driving directions are given in miles and human heights are given in feet. We actively choose appropriate resolutions for a given task.

Since both of these considerations are important to the interpretation of the work, we will discuss them both.

Simulation Rule Set

As already said, the choice of a simulation rule-set can be done for investigative purposes or to mitigate computational costs. Simulating reality, 'as-is,' is simply not possible -- on any budget. The real world is so information dense, that a 'true simulation' of even the tiniest patches of existence would stress the world's fastest supercomputers. Simulating larger and larger patches of existence means compromising the 'truth' with layers and layers of approximation. By the time we've reached patches of existence large enough for even the most basic plasma physics, we've already abandoned the ideas of quantum fields and particles. We've abandoned the idea that our particles have internal structures by assuming them to be classically charged point-like particles.

What we would call an ideal or perfect plasma simulation would be one able to kinematically track every point of charge in a plasma and calculate the sum contribution of each to the electric and magnetic fields. Even this system, as compromised as it is, is far beyond the computational capabilities of any computer on Earth.

The simulation types which are as close to 'true' as we're able to make while also simulating a patch of plasma large enough to be of interest are called *kinetic simulations*. One type of these simulations, termed *particle-in-cell simulations*, apply the physics directly in the fashion described as 'ideal,' however, the physics is applied over a randomly sampled subset of the particles. This subset is many orders of magnitude smaller than the actual number found in a comparable physical plasma.

With current computational limitations, this class of simulation is typically used for 2D areas of the magnetotail described in terms of tens of earth radii.

Hybrid simulations are considered the next most physical subtype. These simulations treat the ions kinetically while treating the electrons as a fluid. In other words, they are hybrid kinetic-fluid simulations. The assumption of fluid electrons, allows researchers to simulate areas several times larger than full kinetic codes for the same cost. Much of the cost reduction comes from the removal of light waves, plasmas waves, and Debye length scales from the simulation physics, which allows much larger grid scales and time steps. Furthermore, substepping the electron fluid relative to the ion particles allows the particle time step to be much larger than in fully kinetic PIC.

The cheapest class of simulations are fluid simulations. These simulations treat both the ions and the electrons as fluids. With the extreme reduction in cost afforded by this approach, researchers have been able to use them to simulate plasmas over much larger areas. Some groups even use variants of fluid simulations in order to do global MHD models over the entire magnetosphere [68] or across large swaths of the solar system [65] [66]. Really large simulations such as these necessarily sacrifice the ability to resolve comparatively small phenomenon.

Being hundreds or thousands of times more computationally expensive than their 2D counterparts, 3D simulations must be done with a careful eye to cost. It was with that expense in mind that we chose to use fluid simulations in our research.

A Fluid Model

The equations used to simulate the plasma are based on the MHD equations introduced in the background section of this thesis. Written in the form already presented, they appear as:

$$\frac{\partial \rho}{\partial t} + \vec{\nabla} \cdot (\rho \vec{v}_i) = D\nabla^4 \rho,$$

$$m_i n \left(\frac{\partial \vec{v}_i}{\partial t} + (\vec{v}_i \cdot \vec{\nabla}) \vec{v}_i \right) = \frac{1}{c} \vec{J} \times \vec{B} - \vec{\nabla} P + D\nabla^4 \vec{v}_i,$$

$$\frac{\partial \vec{B}}{\partial t} = -c\vec{\nabla} \times \vec{E} + D\nabla^4 \vec{B},$$

$$\frac{d}{dt}\left(\frac{P}{n}\right) = 0,$$

$$\vec{J} = \frac{\mathrm{c}}{4\pi} \vec{\nabla} \times \vec{B},$$

$$\vec{\nabla} \cdot \vec{B} = 0,$$

$$\vec{E} = -\frac{1}{c} \vec{v}_i \times \vec{B} + \frac{1}{nec} \vec{J} \times \vec{B} - \frac{m_e}{e} \frac{d\vec{v}_e}{dt}.$$

Although they look a little different, the meanings of the equations remain unchanged from before. We have, however, added a few things of note. The first thing to notice is that on all of the equations that evolve in time, we have added the term:

$$\frac{\partial A}{\partial t} = \cdots + D\nabla^4 A.$$

This term is known as *hyperviscosity*. It's added for purely numerical purposes and not physical. It serves as a smoothing term, preventing changes in the variables from becoming *too* sharp. Because of the nature of our computational methods, very sharp gradients will destabilize the simulation, causing it to crash. Also because of the

nature of our computational methods, sharp noise level gradients are unavoidable. The parameter D is tuned according to the needs of each simulation.

We have also chosen an isothermal equation of state for our system, $\gamma = 1$.

$$\frac{d}{dt}\left(\frac{P}{n}\right) = 0,$$

can be rewritten more plainly as,

$$PV = NkT = constant.$$

We chose to work in an isothermal state in order to remove pressure as a variable. When the temperature is held constant, the pressure variable can be replaced by:

$$P = nkT.$$

Assuming an isothermal plasma is not strictly justified in the Earth's magnetotail. However, the goal in this thesis is to understand the fundamental behavior of these basic 3D x-lines. Including more complex behavior is left for future studies.

For similar reasons, the electron temperature was chosen to be zero. This means that the only relevant gas dynamics in the simulations are those of the ions.

Finally, the equation for the electric field has been drastically modified from the simple MHD presentation in the beginning of this work. Inspired by the electron equation of motion,

$$nm_e \frac{d\vec{v}_e}{dt} = -en\vec{E} - \frac{en}{c}\vec{v}_e \times \vec{B} - \vec{\nabla}P_e,$$

$$\frac{\vec{J}}{ne} = \vec{v}_i - \vec{v}_e,$$

$$nm_e \frac{d\vec{v}_e}{dt} = -en\vec{E} - \frac{en}{c}\left(\vec{v}_i - \frac{\vec{J}}{ne}\right) \times \vec{B} - \vec{\nabla} P_e.$$

Solving for the electric field, we get our electric field equation,

$$\vec{E} = -\frac{1}{c}\vec{v}_i \times \vec{B} + \frac{1}{nec}\vec{J} \times \vec{B} - \frac{1}{ne}\vec{\nabla} P_e - \frac{m_e}{e}\frac{d\vec{v}_e}{dt}.$$

Since there is no electron temperature, we can remove the electron pressure term from the equation,

$$\vec{E} = -\frac{1}{c}\vec{v}_i \times \vec{B} + \frac{1}{nec}\vec{J} \times \vec{B} - \frac{m_e}{e}\frac{d\vec{v}_e}{dt}.$$

This introduces two additions above and beyond the standard MHD electric field. First, we have added the familiar Hall term,

$$\frac{1}{nec}(\vec{J} \times \vec{B}).$$

As well as a new term called the *electron inertia*,

$$\frac{m_e}{e}\frac{d\vec{v}_e}{dt}.$$

It is really these additions to the electric field which elevate the simulation above the level of being an MHD simulation. The technical nomenclature for the simulations would be: "Hall-MHD simulation with electron inertia."

Although this is the standard form used for our analytical work, it's not the form for the equations as they are used in the simulation code. In the simulation, they are expressed in a more efficient set of variables. Those being, $J, J_i, B,$ and n and the intermediate variables, B' and E'. So we rewrite the formulas in terms of these variables using these identities and a good amount of algebra,

The Normalization

The virtual space in which a simulation runs is completely arbitrary. At the most basic level, a researcher has a few thousand cells of 'space' and a few thousand blocks of 'time' with which to work. Instead of dividing up the space and time into fixed quantities like meters or feet, we choose to divide our virtual space into a more scalable set of units. The generic statement would be: "How far can X move during action Y?" Taking the example of a race planner and applying this scalable logic. A race planner may ask, "How far can my runners run before they become exhausted," in order to choose a race distance. Following this type of thinking, a long distance race length for athletes will be scaled larger than a race length for children.

By setting our dynamical variables in a similar fashion, we are giving our plasma simulation the capability to represent an infinite number of real world plasmas. The length scales in our work have all been normalized to the equilibrium ion inertial length, $\gamma_L = c/\omega_{pi} = \sqrt{c^2 m_i/(4\pi n e^2)}$, which is a function of our equilibrium conditions. This means that our diffusion region will have a length along the outflow direction of approximately 10 in code units. Our time scales have all been normalized to the ion cyclotron frequency, $\gamma_t = \Omega_i^{-1} = (eB/m_i c)^{-1}$, which is also a function of our equilibrium conditions. Alternatively, this can be viewed as a normalization resulting in an equilibrium Alfven wave traveling a unit distance in a unit time. Since these length and time scales depend on the properties of the equilibrium plasma, the simulation results can be applied to many different real-world length and time scales. The other independent variables, B and n, are normalized to their equilibrium values. And the mass is normalized to the ion mass.

Another necessary compromise due to the limited number of space cells available to us are some of the choices for constants. For example, the mass of the

electron was chosen to be 1/25th of the mass of the ions. This factor sets the relative difference in scale between electron and ion dynamics. With a factor 25 in the mass, the length scale of the electron dynamics are set to be about 1/5th the size of the ion dynamics. With them being so close to the same scale, it's reasonable to expect a fixed number of space cells to be able to capture both dynamics adequately. However, in the natural world electron dynamics occur at about 1/50th of the scale of the proton dynamics. Which means a gridding which nicely resolves the electron-scale physics, will be missing the vast majority of the proton physics. It would be like trying capture a baseball game on film using a narrow-angle zoom lens.

To see an example of this normalization process, consider,

$$\vec{\nabla} \times \vec{B} = \frac{4\pi}{c}\vec{J}.$$

If we replace each physical quantity with its normalized counterpart,

$$B \to \gamma_B \bar{B},$$
$$J \to \gamma_J \bar{J},$$
$$\nabla \to \left(\frac{1}{\gamma_L}\right)\bar{\nabla},$$

and

$$c \to C_A \bar{c}.$$

We get a new version of the relationship,

$$\left(\frac{\gamma_B}{\gamma_L}\right)\vec{\bar{\nabla}} \times \vec{\bar{B}} = \left(\frac{\gamma_J}{C_A}\right)\frac{4\pi}{\bar{c}}\vec{\bar{J}}$$

Using $J = nev$ and $\bar{J} = \bar{n}\bar{e}\bar{v}$, we can find,

$$\gamma_J = \gamma_n \gamma_e C_A.$$

Substituting this in and following the algebra down the rabbit hole,

$$\left(\frac{\gamma_B}{\gamma_L}\right)\vec{\bar{\nabla}} \times \vec{\bar{B}} = \left(\frac{\gamma_n \gamma_e C_A}{C_A}\right)\frac{4\pi}{\bar{c}}\vec{\bar{J}},$$

$$\left(\frac{\gamma_B}{C_A\gamma_t}\right)\vec{\nabla}\times\vec{B} = \left(\frac{\gamma_n\gamma_e C_A}{C_A}\right)\frac{4\pi}{\bar{c}}\vec{J},$$
$$\left(\frac{\gamma_B}{\gamma_t}\right)\vec{\nabla}\times\vec{B} = \left(\frac{4\pi\gamma_n\gamma_e C_A^2}{C_A}\right)\frac{1}{\bar{c}}\vec{J}.$$

Utilizing the fact that we are essentially normalizing to the Alfven speed,

$$C_A^2 = \frac{\gamma_B^2}{4\pi\gamma_n\gamma_m},$$

Simplifies the expression even more,

$$\left(\frac{\gamma_B}{\gamma_t}\right)\vec{\nabla}\times\vec{B} = \left(\frac{\gamma_e\gamma_B^2}{C_A\gamma_m}\right)\frac{1}{\bar{c}}\vec{J},$$
$$\left(\frac{1}{\gamma_t}\right)\vec{\nabla}\times\vec{B} = \left(\frac{\gamma_e\gamma_B}{\bar{c}C_A\gamma_m}\right)\vec{J}.$$

Until finally, with one last substitution,

$$\gamma_t = \frac{\bar{c}C_A\gamma_m}{\gamma_e\gamma_B} = \frac{c\gamma_m}{\gamma_e\gamma_B},$$

We find the form of the equation actually used in the simulation:

$$\vec{\nabla}\times\vec{B} = \vec{J}.$$

All of the formulas used in the fluid code undergo a similar normalization, resulting in a final representation. From this point on in this thesis, all variables will be implicitly normalized:

$$m_i = 1$$

$$\vec{J}_i = ne\vec{v}_i,$$

$$P = nkT,$$

$$\frac{\partial n}{\partial t} + \vec{\nabla}\cdot\left(\vec{J}_i\right) = D\nabla^4 n,$$

$$\frac{\partial\vec{J}_i}{\partial t} = -\vec{\nabla}\cdot\left(\vec{J}_i\vec{J}_i/n\right) + \left(\vec{J}\times\vec{B}\right) - \frac{1}{n}\vec{\nabla}P + D\nabla^4\vec{J}_i,$$

$$\frac{\partial\vec{B}'}{\partial t} = -\vec{\nabla}\times\vec{E}' + D\nabla^4\vec{B}',$$

$$\vec{E}' = \frac{1}{\rho}\left(\vec{J} \times \vec{B}' - \vec{J}_i \times \vec{B}\right),$$

$$\vec{B}' = \left(1 - \frac{m_e c^2}{ne^2}\nabla^2\right)\vec{B}, \tag{5}$$

$$\frac{d}{dt}(T) = 0,$$

$$\vec{J} = \vec{\nabla} \times \vec{B},$$

$$\vec{\nabla} \cdot \vec{B} = 0.$$

The final modification made to the equations before being used in simulation is done to Equation (6). The coefficient

$$\frac{m_e c^2}{ne^2}$$

is taken to be the constant, d_e^2, with n set to the equilibrium value.

The Equilibrium

As mentioned above, the simulation length scales depend on the equilibrium of the system. This raises the important question, "what is the equilibrium of this system?"

The system is initialized in a double Harris sheet configuration with periodic boundary conditions in every direction. The orientation of the current sheets in our systems can be seen in Figure 12. The double Harris sheet is a well known starting condition in 2D reconnection studies [23]. The basic idea is to begin reconnection around a flat current sheet, much like what would be expected in the magnetotail. In computational work, boundary conditions are always problematic. Simulating two antipodal current sheets instead of one introduces a symmetry to the system which

allows periodic boundary conditions to be applied. Mathematically, our starting magnetic field simply follows as:

$$B_x(y) = B_0(\tanh[(y + \Delta_y/4)/\omega_0] - \tanh[(y - \Delta_y/4)/\omega_0] - 1).$$

Where, $B_0 = 1$, Δ_y is the system length in the y-direction, and ω_0 roughly represents the starting width of the current sheet.

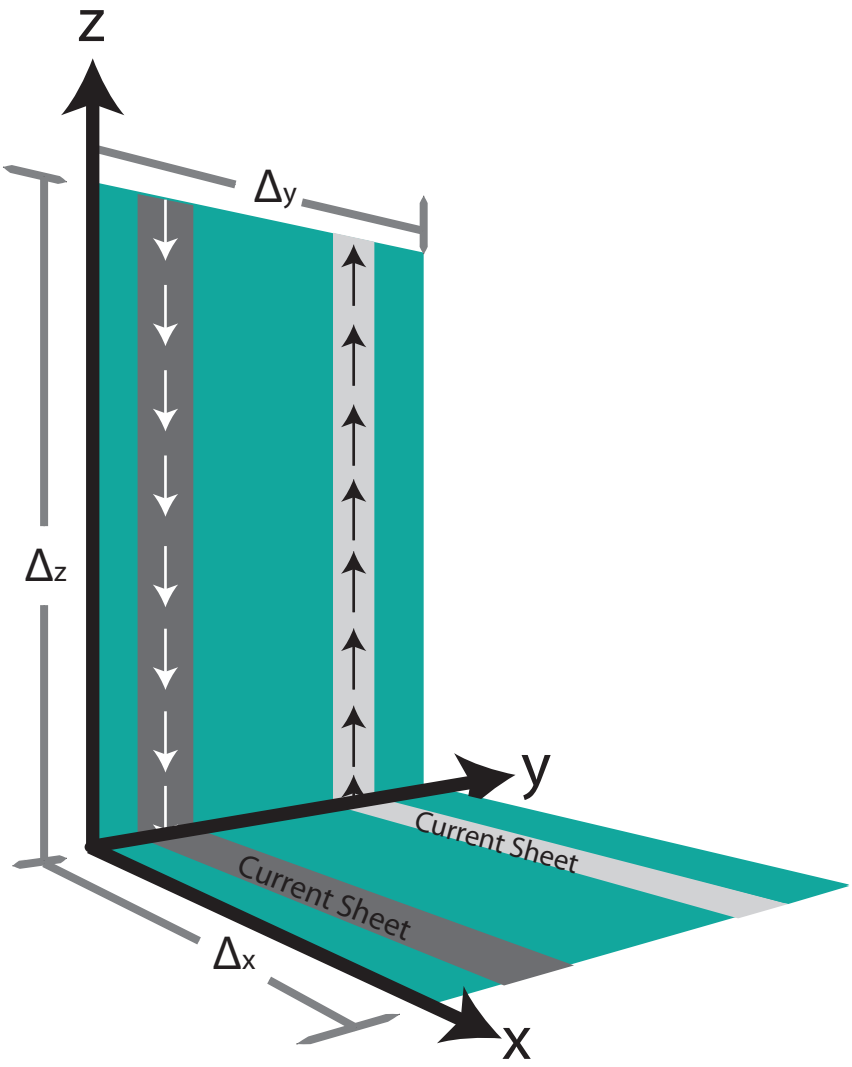

Figure 12 Schematic relating our simulation coordinates to the double Harris sheet orientation. The current flows in the $\pm z$ directions. The traditional outflow is in the x-direction. The traditional 2D inflow is in the y-direction. The length of the system in the x, y, and z directions are Δ_x, Δ_y, and Δ_z respectively. Most figures in this thesis are taken from the negative current sheet, depicted as dark gray in the figure.

Having decided upon an initial current distribution and thus an initial magnetic field configuration, this also fixes the starting density. The system is initialized in pressure balance, so the gas pressure is chosen so that the total pressure remains constant,

$$P_{total} = B^2/2 + P_{gas}.$$

Finally, small random fluctuations are added to the ion velocities and magnetic fields.

The Seed Perturbation

In order to initiate reconnection in our system, we perturb the vector potential, $\vec{A}$, by a small amount given by,

$$A_z = \mathcal{E}_0 \left(\frac{\Delta_x}{4\pi}\right)\left(1 + \cos\left(\frac{4\pi}{\Delta_y}(y + \Delta_y/4)\right)\right)\sin\left(\frac{4\pi x}{2\Delta_x}\right)F(z),$$

where

$$F(z) = \left(\frac{1}{\cosh(z/\omega_{0z})}\right)^2.$$

This perturbation, in turn, perturbs the magnetic field while maintaining, $\vec{\nabla} \cdot \vec{B} = 0$. The easiest inroad into understanding this perturbation is to first look at $F(z)$ in Figure 13. $F(z)$ is an envelope function of height 1 and width approximately $2\omega_{0z}$.

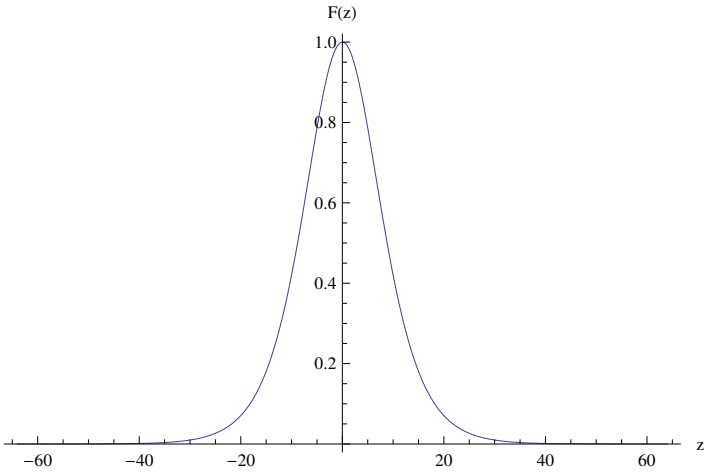

Figure 13 The envelope function, F(z), restricts the perturbation size in the z-direction.

This function serves only to localize the perturbation of the vector potential in the out-of-plane direction.

This leaves us to only have to consider the perturbation in the x-y plane. The affect of the perturbation on the magnetic field in that plane can be calculated from:

$$B_{x1} = \frac{\partial A_z}{\partial y},$$

$$B_{y1} = -\frac{\partial A_z}{\partial x}.$$

Resulting in,

$$B_{x1} = -\mathcal{E}_0 \left(\frac{\Delta_x}{\Delta_y}\right) \sin\left(\frac{4\pi}{\Delta_y}\left(y + \Delta_y/4\right)\right) \sin\left(\frac{4\pi x}{2\Delta_x}\right) F(z),$$

$$B_{y1} = \mathcal{E}_0 \left(1 + \cos\left(\frac{4\pi}{\Delta_y}\left(y + \Delta_y/4\right)\right)\right) \cos\left(\frac{4\pi x}{2\Delta_x}\right) F(z).$$

We can see immediately, the amplitude of the perturbation is determined by, $\mathcal{E}_0$. The trigonometric portion of the equation determines the placement of the perturbation in the space. In this case, Figure 14, Figure 15, and Figure 16 tell the story much more concisely.

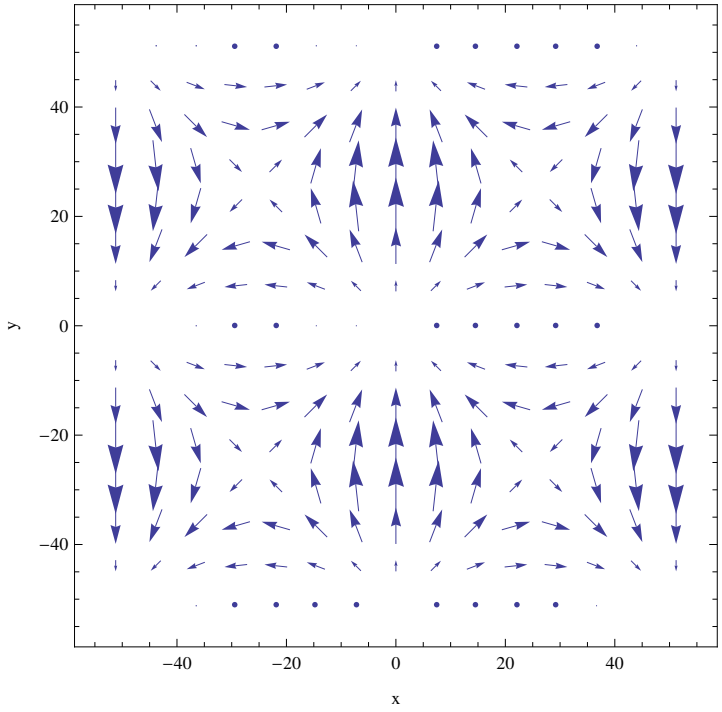

Figure 14 Plot of the in-plane perturbation in the magnetic field which will be added to the equilibrium field.

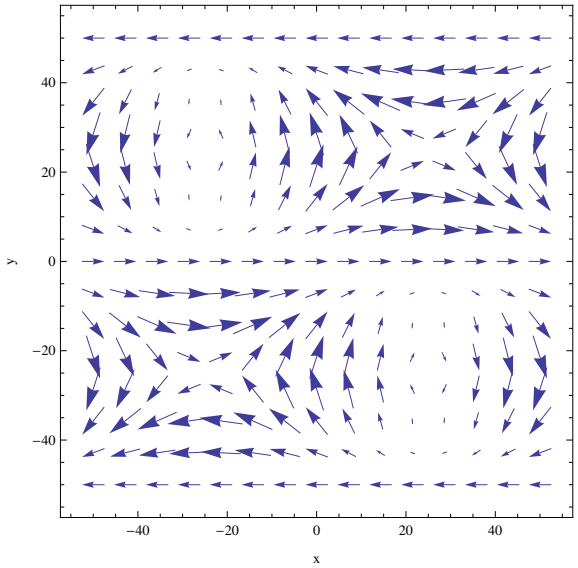

Figure 15 Plot of the magnetic field in the plane of reconnection after the perturbation has been added. In this case, the perturbation magnitude, $\mathcal{E}_0$, has a value of 1.0 in order to increase the visibility of its contribution. From this figure we can locate the x-lines in the system in the bottom-left and top-right corners.

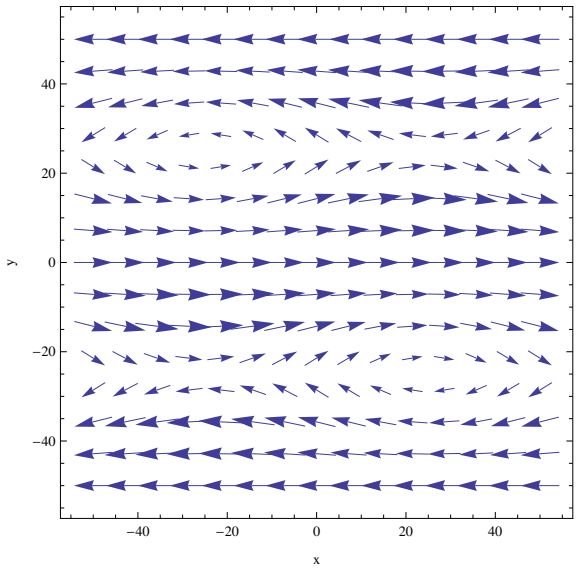

Figure 16 Plot of the magnetic field in the plane of reconnection after the perturbation has been added with $\mathcal{E}_0 = 0.1$

The perturbations are positioned in such a way that it produces two x-lines and two o-lines compatible with the periodic boundary conditions. It does this at each value of z, scaled by the envelope factor.

Taken on its own, this perturbation in the magnetic field would represent a magnetic energy as can be seen in Figure 17.

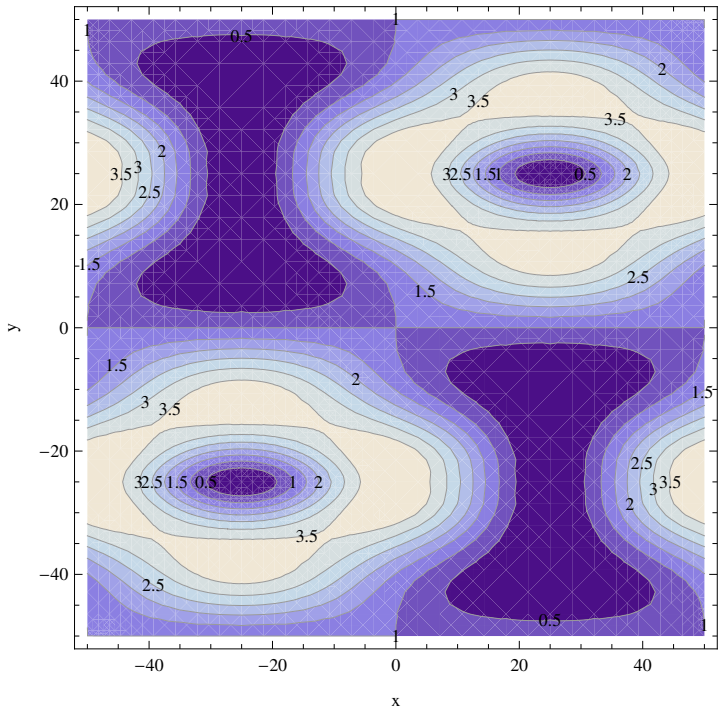

Figure 17 Contour plot for the magnetic energy of the perturbation, in the absence of an equilibrium field.

The total magnetic energy when combined with the equilibrium can be seen in the contours of Figure 18. A bubble of magnetic energy roughly $\mathcal{E}_0$ in magnitude is transplanted from the upstream location of the o-line to the x-line.

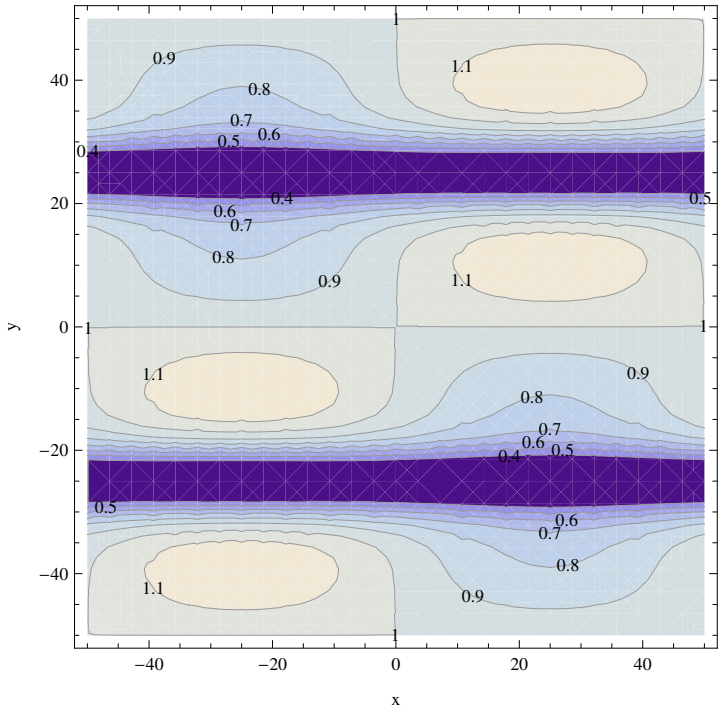

Figure 18 Contour of the magnetic energy in the plane of reconnection after adding the seed perturbation to the equilibrium field.

The major contribution to the energy perturbation can be calculated by:

$$U = \vec{B} \cdot \vec{B} = B_x^2 + B_y^2 + B_z^2,$$

$$B_x^2 = (B_{x0} + B_{x1})^2 = B_{x0}^2 + 2B_{x0}B_{x1} + B_{x1}^2,$$

$$B_y^2 = B_{y1}^2,$$

$$B_z^2 = 0.$$

Since the perturbation is of magnitude, $\mathcal{E}_0$, which is small compared to the initial magnetic field, we can neglect higher powers of the perturbed magnetic field's contribution to the energy. Giving a perturbation energy of,

$$U_1 = 2B_{x0}\mathcal{E}_0. \tag{6}$$

So the perturbation moves a volume of energy from one part of the system to the other part of the system. That amount of energy scales with: $B_{x0}\mathcal{E}_0(\omega_{0z}\omega_0\Delta_x)$.

Numerical Methods

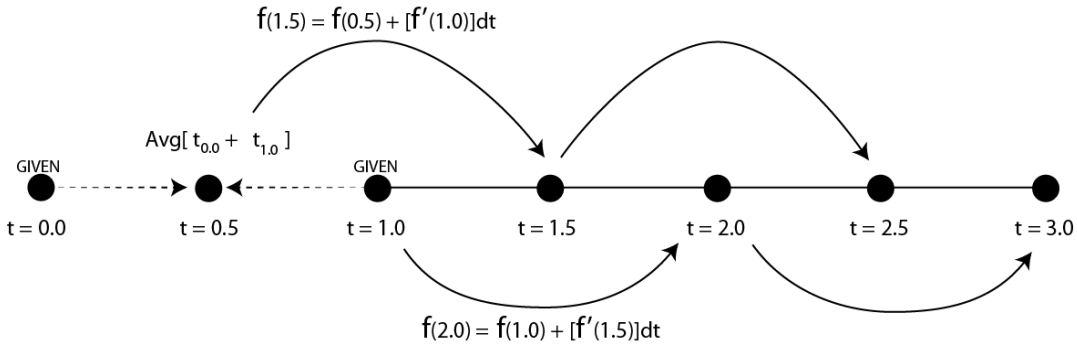

Figure 19 Second-order leap frog technique used to integrate the differential equations in time. Each dot represents a point in time. Integral values of the time are outputted as data while fractional values are intermediary values kept for calculation purposes only.

Some of the equations that we are solving are differential equations in time. In order to integrate these equations numerically, we use the a technique which at its core is, after a time interval Δt:

$$f_1 = f_0 + f_0'\Delta t,$$

where the subscript 1 represents the future value of the variable and 0 is the present or given value. One of the inaccuracies introduced by this technique is that f' may change over the time interval Δt, making f_0' an inaccurate representation of the change in f over the interval. In order to reduce this error, instead of simply using f' as

calculated at the present time, we use a valued averaged between $old\ f$ and $new\ f$. Superficially, this appears to introduce a logical paradox. In order to calculate *new f*, we need $f'_{0.5}$. In order to calculate $f'_{0.5}$, we need *new f*. We solve this basic dilemma with the trapezoidal leapfrog method presented in Figure 19.

We can see from the figure, that by calculating intermediary values of *f*, we can proceed in a 'leap frog' fashion forward indefinitely. The only catch is that in order to start this technique, we must begin the simulation with an *f* at two different times. To skirt that problem, we generate a 2nd *initial* time step using the less accurate method first mentioned.

To handle the spatial derivatives, we use a 4th order accurate numerical approximation,

$$\frac{\Delta u}{\Delta x} = \left(\frac{1}{\Delta x}\right)\left[\frac{2}{3}u(x+\Delta x) - \frac{2}{3}u(x-\Delta x) - \frac{1}{12}u(x+2\Delta x) + \frac{1}{12}u(x-2\Delta x)\right] + \mathcal{O}^5$$

In order to arrive at this relationship, begin with the tailor expansions of,

$$u(x+\Delta x) = u(x) + u'(\Delta x) + 1/2\ u''(\Delta x)^2 + \cdots, \tag{7}$$

$$u(x-\Delta x) = u(x) - u'(\Delta x) + 1/2\ u''(\Delta x)^2 - \cdots, \tag{8}$$

$$u(x+2\Delta x) = u(x) + 2u'(\Delta x) + 2u''(\Delta x)^2 + \cdots, \tag{9}$$

$$u(x-2\Delta x) = u(x) - 2u'(\Delta x) + 2u''(\Delta x)^2 - \cdots. \tag{10}$$

Subtract (6) from (5) and (8) from (7) to get,

$$u(x+\Delta x) - u(x-\Delta x) = 2u'(\Delta x) + 1/3\ u'''(\Delta x) + \mathcal{O}^5,$$

$$u(x+2\Delta x) - u(x-2\Delta x) = 4u'(\Delta x) + 8/3\ u'''(\Delta x) + \mathcal{O}^5.$$

Solving for u' while eliminating u''' gives us the result.

Simulation Parameters

Finally, we present the simulation parameters used in this work in Table 1. We began with a series of runs intended to establish the standard behavior of the x-line as we varied the equilibrium current sheet width, ω_0. It was our hope to discover that very wide current sheet widths would produce transient reconnection. The "High Noise" section of the table represents notable examples taken from this series.

With run 107.9, we discovered our first example of a simulation with transient reconnection. It was, however, produced using a very strong initial perturbation and strong ambient noise. After this example was found, we did further runs in a low noise environment, intended to probe the circumstances of marginal or failed reconnection. The, "Low Noise" section represents this probing.

Run	Spatial Dimensions						Time	Perturbation Size		
	Δ_x	Δ_y	Δ_z	N_x	N_x	N_z	Δt	ω_0	$\mathcal{E}_0$	ω_{0z}
High Noise										
105.3	51.2	51.2	128	512	512	64	.02	0.5	.08	10
107.8	102.4	51.2	128	1024	512	64	.02	1.4	.08	10
107.6	102.4	51.2	128	1024	512	64	.02	3.376	.08	10
107.9	102.4	51.2	128	1024	512	64	.02	5.0	.24	10
107.25	102.4	51.2	128	1024	512	64	.02	5.0	.24	60
Low Noise										
107.29	102.4	102.4	128	512	512	64	.1	5.0	.015	10
107.31	102.4	102.4	128	512	512	64	.1	5.0	.03	10
107.30	102.4	102.4	128	512	512	64	.1	5.0	.24	10
1077.4	102.4	102.4	128	512	512	64	.1	5.0	.24	2.5
107.36	102.4	102.4	128	512	512	64	.1	5.0	.12	10
107.37	102.4	102.4	128	512	512	64	.1	5.0	.12	5
1077.2	102.4	102.4	128	512	512	64	.1	5.0	.12	2.5
107.34	102.4	102.4	128	512	512	64	.1	5.0	.06	10
107.39	102.4	102.4	128	512	512	64	.1	5.0	.06	5
107.41	102.4	102.4	128	512	512	64	.1	5.0	.05	10
107.42	102.4	102.4	128	512	512	64	.1	5.0	.04	10
107.45	102.4	102.4	128	512	512	64	.1	5.0	.038	10
107.46	102.4	51.2	128	1024	512	64	.1	1.4	.08	10
107.47	102.4	102.4	256	512	512	128	.1	5.0	.04	20
107.50	102.4	102.4	256	512	512	128	.1	5.0	.04	30
107.49	102.4	102.4	256	512	512	128	.1	5.0	.04	40
107.51	102.4	102.4	256	512	512	128	.1	5.0	.04	60

Table 1 Table of simulations used. The runs can be broken into two main categories – an initial set of runs done with a large random perturbation and a quiescent set of runs done with very little noise with a more focused goal. Δ_x, Δ_y, and Δ_z are the spatial dimensions of the simulation box. N_x, N_y, and N_z are the numbers of grid cells in the x, y, and z directions. The time steps used in the numerical integration are listed in the Δt column. Finally, the parameters adjusted in the course of the investigation, the perturbation size, are listed under the columns ω_0, ω_{0z}, and $\mathcal{E}_0$. Runs discussed at length in the following chapters are highlighted.

Although all simulations held two reconnection current sheets, all of the figures presented come from a single current sheet. The coordinate system for that current sheet can be seen in Figure 20.

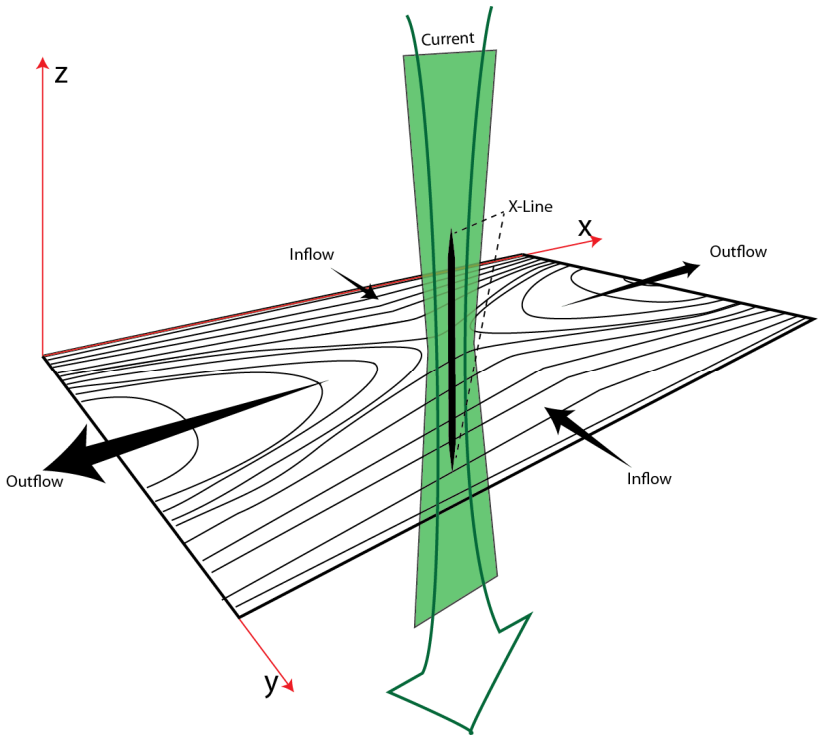

Figure 20 Schematic of the 3D X-line.

Chapter 3

TRACING

The first stumbling block to any study of magnetic reconnection in 3D is, unfortunately, a semantic one. Since magnetic reconnection is an active field of research, there is still much to be learned with many aspects of the physics still misunderstood or mischaracterized. In two dimensions, where most of the research to date has been focused, the semantics of reconnection is robust. In three dimensions, many of those concepts and much of the vocabulary must be inspected and modified.

"Types" of 2D Reconnection

As we've already discussed, when opposing magnetic fields are brought together in a plasma, a current sheet will form in the space between the two magnetic polarities. If that current sheet is then subject to a uniform resistivity, then the system will eventually undergo Sweet-Parker reconnection. Studies of Sweet-Parker reconnection show its diffusion region has an aspect ratio which scales with system size and thus it does a poor job of converting magnetic energy into plasma flow at larger scales [58]. Since reconnection in space typically occurs over very large length scales, this type of reconnection is also called "slow" reconnection. It reconnects magnetic flux at a rate too slow to explain the explosive energy releases observed near the Sun and Earth.

If instead of having a uniform resistivity, the current sheet has a region of anomalously high resistivity, magnetic reconnection which forms there will have a different structure. Instead of having a very long system dependent inflow, like Sweet-Parker reconnection, it will have a very constrained system independent inflow.

This type of reconnection is sometimes called "fast" reconnection, because the rate of energy conversion from magnetic energy to plasma flow is fast enough to explain observed phenomena in space. Reconnection with a fixed diffusion region, like this, is called Petscheck-like reconnection.

The final 'type' of reconnection which is often discussed in 2D studies is called, Hall reconnection. In fluid simulations hall reconnection has been found to occur when the stock MHD equations are modified to include the Hall term and the current sheet becomes narrow. Hall reconnection is much like Petscheck reconnection. It has a fixed aspect ratio which can lead to explosive energy conversion, this similarity often leads to it also being called, 'fast reconnection.'

All of these 'types' of reconnection have caveats attached to them. Sweet-Parker reconnection results from a fluid description of plasma physics, where the basic MHD equations are modified by a uniform resistivity term. The conditions for uniform resistivity assume that the collisions frequency is large compared to all other dynamical frequencies. In the magnetotail, where this study is focused the collision frequency is quite small and this assumption is suspect. However, in the 3D reconnection studied in this thesis, there are reconnecting regions where $L_y/L_x \ll 0.1$. We use the term "Sweet-Parker-like" to describe these regions.

It is much the same with Petschek reconnection. However, unlike Sweet-Parker reconnection, the idea that pieces of space could have anomalous resistivity is suspect. Although there are theoretical arguments for the existence of anomalous resistivity based on theoretical analysis of various instabilities , no fully kinetic simulation of reconnection has demonstrated that such anomalous resistivity is playing a dominant role [26]. Reconnection driven by the Petschek mechanism has yet to be

found in nature, however the term "Petschek-like" is still used to describe fixed aspect ratio reconnection for historical reasons.

Hall reconnection has a somewhat stronger theoretical footing than Petschek reconnection. 'Hall-like' reconnection has been observed to form naturally in fully kinetic 2D simulations. Differences between Hall reconnection as discovered through fluid simulations and hall reconnection as observed in the real world or in kinetic codes are still being explored. Once again, we should be careful to say, "Hall-like" reconnection when discussing nature or kinetic simulations, as the name refers to a specific behavior found in the fluid equations.

At the same time that researchers were exploring these different ways of converting magnetic energy into plasma flow energy, others were attempting to codify a singular formal definition for magnetic reconnection. Axford argued that a local break down of the frozen-in condition was the key component by which we can identify reconnection [4]. Vasyliunus observed that the break down in connectivity required an electric field parallel to a separator line [67]. Priest and Forbes defined reconnection as a slew of properties coincident in reconnecting systems, including plasma flow across separators [51]. Hesse et al. derived a generalized reconnection law, which linked the integral along a field line of the parallel electric field with the rate at which magnetic connectivity was broken [25]. Most researchers operated outside of this debate utilizing the umbrella of experience identify reconnection.

Despite there being no consensus on a formal definition for magnetic reconnection, in the context of 2D research, magnetic reconnection was well defined. Fluid simulations underwent Sweet-Parker or Hall reconnection, there was no confusion. Every formal definition seemed adequate. Observed reconnection in

space, laboratories, or kinetic simulations had Sweet-Like or Hall-Like properties. All of the definitions adequately described reconnection observed in 2D simulations.

However, in the transition to 3D, none of the formal definitions of reconnection went un-scathed. For example, in the formation of a plasmoid reconnection was shown to not require separator surfaces [54]. Any definitions which required this aspect of reconnection geometry suddenly lacked generality.

Likewise, as we will see, the clean archetypes for 2D reconnection discussed thus far will fall short even in simple 3D systems.

Three Dimensions

Reconnection in 2D simulations can be easily ascribed. If the simulation is utilizing fluid physics with the Hall term included, the resulting reconnection will invariably be Hall reconnection. Any structure reminiscent of Sweet-Parker reconnection is just a transient state on the way to the 'real reconnection.' In that context, if a researcher is tasked with the goal of studying some aspect of reconnection, there is no ambiguity. You don't have to ask, "What do you mean reconnection?" In 3D, that question has to be asked.

To illustrate the need for this question, Figure 21 provides an out-of-plane cut of a reconnection current ribbon. Or more colloquially: the central black smudge on the right hand side of the figure roughly represents the x-line of the reconnection site.

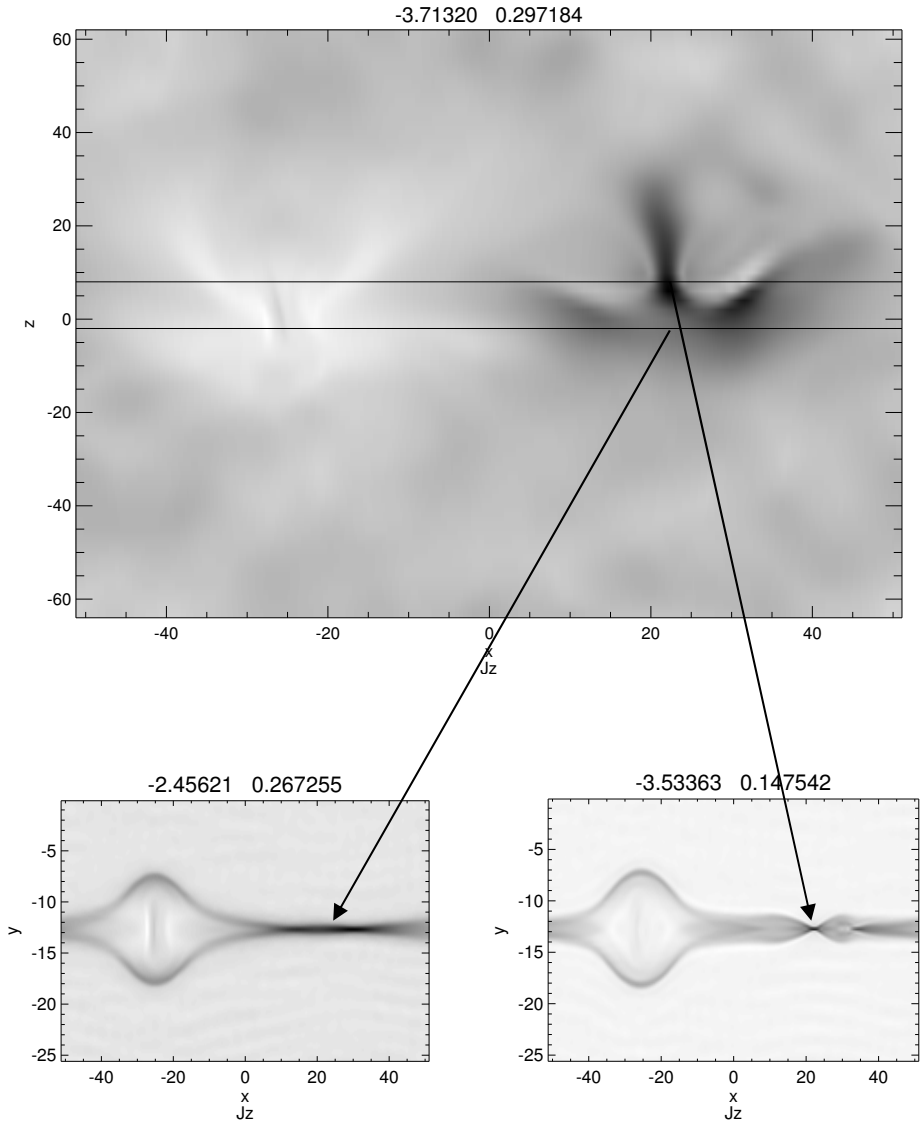

Figure 21 (107.8; t = 60) (Top, y = -12.8): A slice of J_z along the current sheet. To the right, in black, is the x-line. In 3D, a single x-line can be found in several different configurations in the out of plane direction. Along the top, edge, the hazy dispersed current is representative of newly forming or proto-reconnection. At the very bottom (Bottom Left Figure, z = -2) an in-plane cut shows that the x-line is in a long and extended configuration, reminiscent of Sweet-Parker. Just above that, where the x-line is dramatically pinched inward (Bottom Right Figure, z = 7), we see the expected narrow reconnection configuration with open outflows.

It's a region of enhanced current due to the pinched nature of the current sheet. Key to understanding the language difficulty is seeing that the x-line has a beginning and an end -- as you traverse the x-line from top to bottom, the structure and behavior of the reconnection changes. In the center of the most intense current, the reconnection structure has a fixed geometry, which as we discussed before is a requirement for fast conversions of magnetic energy into flow energy. However, just below the pinched region, reconnection appears to still be present. There are fast outflows and magnetic flux is consumed. It's just not configured with a fixed sized diffusion region. Instead, the diffusion region in that area appears to be more Sweet-Parker-like as you leave the heart of the x-line. This Sweet-Parker like structure on the bottom of the x-line is not simply a transient state which can be dubbed 'proto-hall-reconnection,' and be dismissed. It's a long lasting component in the overall 3D structure of the x-line. In fact, it can't really be called 'Sweet-Parker,' since the current sheet width is in the Hall physics domain. In the lingua of 2D reconnection, a single 3D x-line simultaneously contains proto-reconnection, hall reconnection, and sweet-parker-like hall reconnection. It also simultaneously contains the spectrum of behavior and structures between these archetypes.

So to re-iterate: “Which if any of these structures are actually reconnection?” What would the answer to that question say about the entire structure? The standard practice thus far in the literature has been to overlook the fringe parts of the x-line, naming the central hall-region as the 'real reconnection.' With the formal definitions of reconnection still in dispute, a rigorous support or denial of that stance has as of yet, been undeveloped.

In the course of our research, overlooking these fringe elements of the greater reconnection system did not seem to be an option. So we developed our own interpretations of the phenomenon.

Our Qualitative Interpretation

When we took a step back and asked ourselves the big question: "Why do people study reconnection? Why is this interesting to our society?" We really concluded that people study reconnection, because it throws plasma around. It takes magnetic energy and converts it into plasma flow energy. We care about reconnection because it ejects plasma out of tokamaks. We're interested in reconnection because it throws plasma against the Earth to create the aurora, or damages satellites, or heats the corona. So we want to study this system because it energizes plasma. If somewhere in the universe, there is a reconnecting system which only allows plasma to change connectivity, without any plasma acceleration, we frankly wouldn't be interested in it. So any part of the x-line which energizes plasma by converting magnetic energy into flow energy via a change in plasma connectivity is going to be called reconnection. This basically means, the entire structure.

Even though we are calling the entire structure, "magnetic reconnection," it's still important to acknowledge that different parts of the x-line have fundamentally different structures and behaviors and so should be categorized differently. We've adopted the following nomenclature. Locations along the x-line which appear to be reconnecting with a large 'Sweet-Parker-Like' diffusion region will be called "slow" regions. Regions which appear to have a fixed aspect-ratio diffusion region will be called, "fast." Be warned: It could very well be that further studies will show these

designations to be misnomers. It could be that the aspect ratio I am calling "slow," may not actually scale with system size. So it may not actually be slow.

In addition to this distinction, it's also pretty clear that the slow reconnection at the top and the slow reconnection at the bottom fringes of the reconnection site are not the same things. The top of the reconnection site spreads the x-line into the fresh current sheet. The bottom of the reconnection site often sits stagnant. We have taken to calling the part of the x-line which traditionally spreads as the "north side." Conversely, the part of the x-line which traditionally does not spread we call the "south side." Figure 22 depicts this naming convention. Slow reconnection, typically a hazy and diffuse region of current, is colored blue while fast reconnection, typically the pinched region of intense current, is colored red.

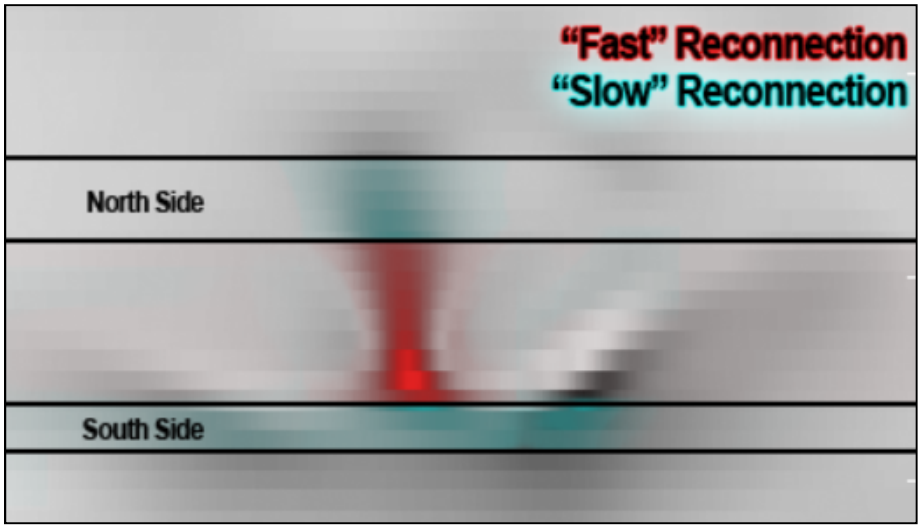

Figure 22 A qualitative description of the out of plane x-line structure. Grayscale of J_z inside of a reconnecting current sheet. The diffuse reconnection at the top of the graph is what will be called "north side." The fishtail structure on the bottom of the x-line is what we call "south side." The dividing barrier should be roughly indicated by the transition in the diffusion region geometry from a short, Petschek-like fixed structure to an elongated structure.

Although it's possible to manually disassemble any given time on any given run visually using, the above classifications, it's not practical en masse. So we present an algorithmic approach.

Quantitative / Algorithmic Approach

The primary technique researchers use to track and classify x-lines in 3D has been by either inspecting the magnitude of the out-of-plane current or in 2D by calculating a quantity called the reconnection rate. Because of this history, we first address those options.

Out-of-Plane Current

When opposing field lines meet in a plane, the instantaneous magnetic field can be approximated by a *Tanh* function of a characteristic width, ω,

$$\vec{B} = tanh(y/\omega)\hat{x}.$$

Which leads easily leads to:

$$\overrightarrow{J_z} = \vec{\nabla} \times \left[tanh(y/\omega)\hat{x}\right] \cdot \hat{z},$$

$$\overrightarrow{J_z} = \frac{1}{\omega}\,\mathrm{sech}^2(y/\omega),$$

$$\overrightarrow{J_z}(y = 0) = \frac{1}{\omega}.$$

Thus, the magnitude of the current is determined by the width of the current sheet. A quick look at Figure 23, where we plot the product $J_z L_y$, confirms the accuracy of this estimation in simulation. In the region of the x-line, on the right, the amplitude of the product is roughly constant. This means that measurements of J_z are a proxy for the current sheet width.

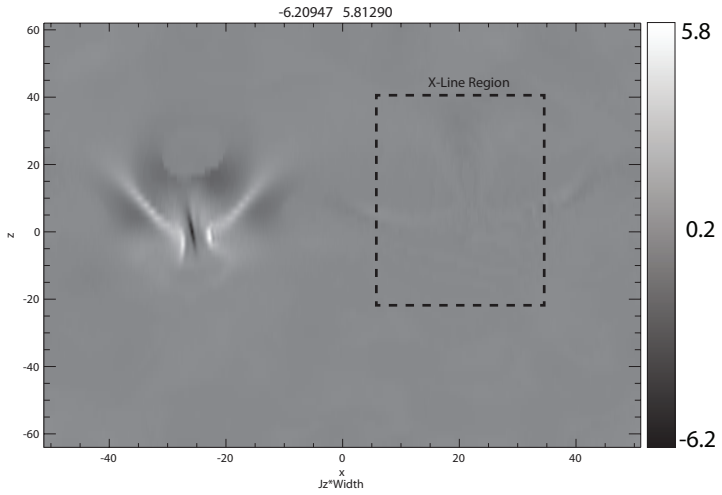

Figure 23 (107.8; t = 60) A plot of $J_z L_y$. The dotted box surrounds the region where reconnection is happening. The absence of any structure indicates that the quantity $J_z L_y$ is constant through the x-line.

Since the length scales at which Hall physics begins to dominate the reconnection dynamics is well established in 2D, it stands to reason that this could be a good indicator of the reconnection structure in 3D. However, this expectation was not borne out in simulation. Although there was a rough correlation between current magnitude and how developed an x-line was, this was very often not the case. For example, in Figure 24, we have a snapshot of an x-line both before and after the onset of 'fast' reconnection. Even though the two snapshots show completely different diffusion region aspect ratios, the current magnitude, is comparable between the two, having magnitudes of roughly -3.0. In addition to this problem, the bulk of the current is established by the equilibrium current sheet. As a consequence of that, any comparison across simulations with differing equilibrium current sheets would have to take that into account. Although commonly used to identify x-lines via manual

inspection, attempting to use it in any automated schema would prove ineffective for these reasons.

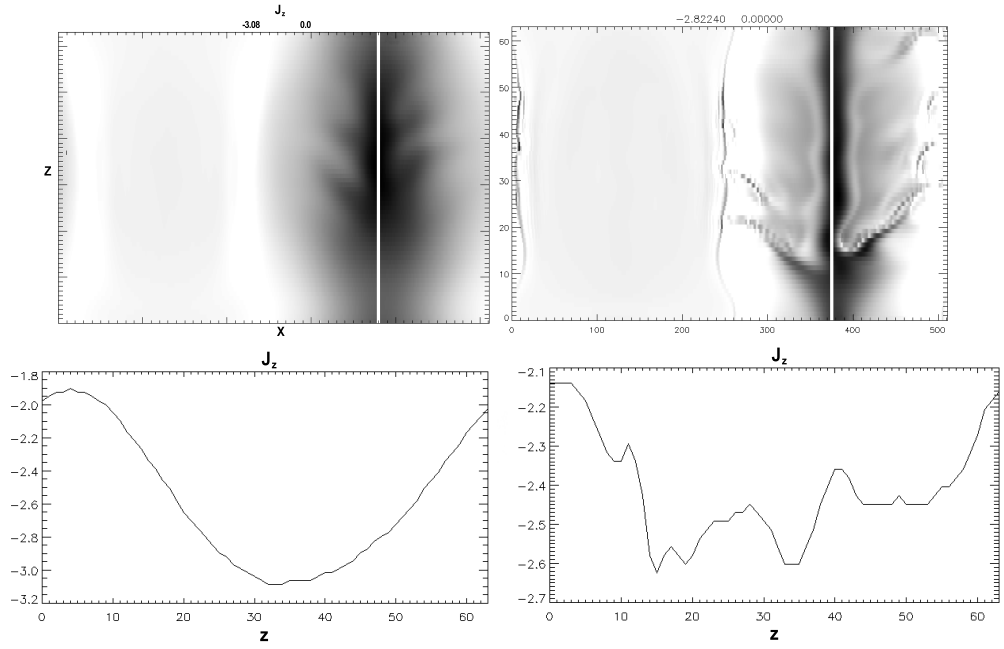

Figure 24 (107.25; t = 80,105) A large 2D-like reconnection simulation at two different time steps. (Top) Grayscale plots of J_z. To the left is an undeveloped x-line to the right is a fully developed x-line. The white vertical line is the path through which a cut was taken. (Bottom) Cut through the current ribbon depicting J_z. Both the developed and undeveloped x-lines have similar maximum currents $J_z \cong -3.0$.

Reconnection Rate

The real tooth behind quantitative studies of 2D reconnection has been the reconnection rate. Colloquially it's defined as, "The rate at which magnetic flux flows into and out of the x-line region." Mathematically it is,

$$Reconnection\ Rate = \frac{d}{dt}\int \vec{B} \cdot d\vec{A}, \tag{11}$$

where the area of integration is taken to be a plane perpendicular to the reconnecting plan with one edge coincident with the x-line and the other ending either at the center of the magnetic island or some other place where this is no convection of magnetic flux. In a 2 dimensional system, this reduces to:

$$2D\ rrate = \frac{d}{dt}\int B_y dx.$$

In practice, the integration is taken from the x-line to the o-line in simulations. In two dimensions, the reconnection rate can distinguish between fully developed x-lines and under developed x-lines. With knowledge of the system's geometry, It can also distinguish between x-lines undergoing Hall reconnection from Sweet-Parker reconnection. A formulation of the reconnection rate in 3D would be ideal for our purposes. Unfortunately, the meaning and adaptation of Equation (11) to three dimensions is of dubious utility.

The first problem with the equation is that it's an integral equation. Integrating the flux of the magnetic field across a surface destroys any local information about the x-line. So a 3D reconnection rate would only be able to give us information about the x-line as a whole. Since x-lines spread in the 'northern' direction, larger x-lines would inherently have a larger 3D reconnection rate. Considering that x-lines are known to

spread many times longer than their initial length, the integral would more strongly represent the extent of the x-line, rather than the intensity/maturity of the x-line.

Additionally, simply choosing an area to integrate over is a non-trivial task. The x-line could flap, bend, or grow its way out of the integration area. This necessitates a technique for detecting the x-line so that we can catch any strange motions. The technique we would use to track x-line flapping or bending is the very technique we're in a process of discovering.

Choosing to ignore the 3D nature of the reconnection system by calculating the reconnection rate 2D-plane by 2D-plane could be done. However, with magnetic flux convecting into and out of the planes from above and below the results would be muddied -- A reconnection rate for a particular 2D sheet, could falsely score a region of x-line as strong or weak, due to out-of-plane convection downstream. With no answer to these difficulties, we preferred a technique with a simpler physical meaning.

Ion Acceleration

Going back to our big picture for inspiration, we explored utilizing the ion acceleration in the outflow direction as a metric for analyzing the reconnection site. The ion diffusion region for Hall reconnection is known to be approximately 10-15 c/ω_{pi} in the outflow direction. For Sweet-Parker reconnection, the diffusion region scales to fill the available space. So it should be roughly $1/4^{th}$ of the system size. If the outflow must accelerate to the Alfven speed over those distances, a first order estimate of the expected gradient would be:

$$Fast\ Acceleration = \frac{C_A}{10} \sim .1,$$

$$Slow\ Accleration = \frac{4C_A}{L_{system}} \sim \frac{4}{\Delta_x}.$$

This means that we should be able to distinguish between Sweet-Parker geometries and Hall geometries by measuring the gradient of the ion outflow velocity. For brevity, we're going to call this quantity an acceleration. The question remains as to whether this is a *good* technique for locating and classifying the x-line.

As can be seen in Figure 25, the outflow 'acceleration' is co-incident with the current and so is comparably good for locating the x-line in the plane. In quite a few cases, it does a slightly better job. The ion acceleration graphs tend to be more localized in the outflow ($\hat{x}$) direction. This often eliminates spurious current structures which are due to a compression of the current sheet without the presence of reconnection.

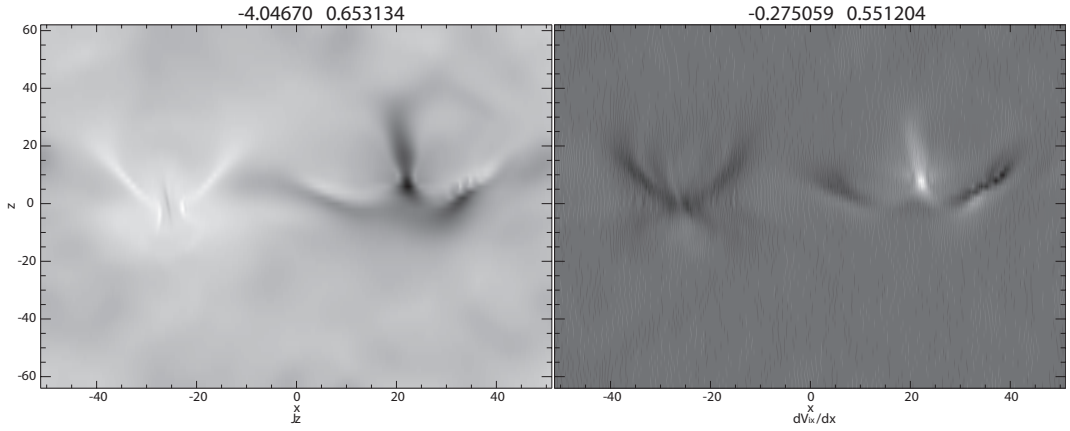

Figure 25 (107.8; t=60) A plot of the J_z on the left and $\partial/\partial x(v_{ix})$ on the right. The two structures are coincident in space.

Unlike the current, $\partial v_{ix}/\partial x$ has fixed thresholds which can be used to determine the diffusion region structure. For that same reason, it can also make these determinations cross-simulation. Revisiting the extended x-line from Figure 24, Figure 26 cuts display the ion acceleration within the diffusion region and show a clear distinction between the structures in the two time slices. Whereas both time slices in the current plots showed similar current magnitudes, the ion acceleration plot clearly distinguishes between proto-reconnection and full reconnection. The early time slice shows an acceleration magnitude below .1 across the entire extent of the box. While the fully formed x-line in the later time step shows values for the acceleration above .1 everywhere except in the diffuse 'slow' region on the south side. It's clear in this example as well as many more that the diffusion region structure can consistently be identified by the ion outflow gradient. The breakdown is,

$$0 \leq \frac{\partial v_{ix}}{\partial x} < \frac{4}{\Delta_x} \quad \rightarrow No\ Reconnection,$$

$$\frac{4}{\Delta_x} \leq \frac{\partial v_{ix}}{\partial x} < 0.1 \quad \rightarrow Slow\ Reconnection,$$

$$0.1 \leq \frac{\partial v_{ix}}{\partial x} \quad \rightarrow Fast\ Reconnection.$$

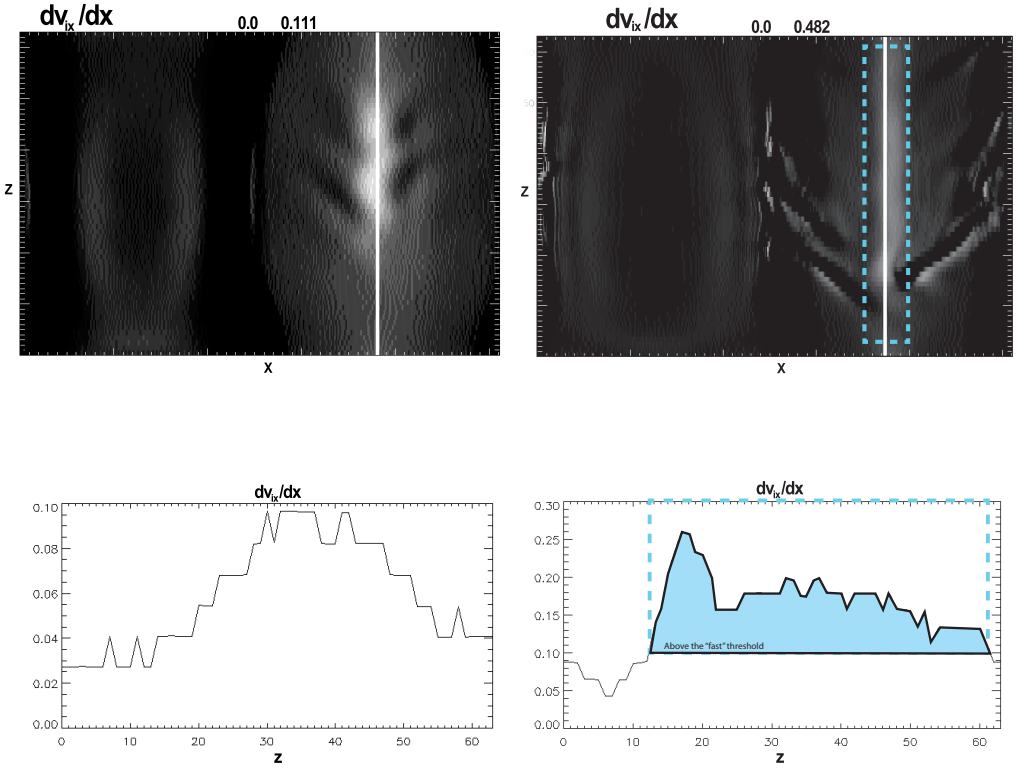

Figure 26 (107.25; t = 105) $\partial/\partial x(v_{ix})$ at an early time on the left and $\partial/\partial x(v_{ix})$ after reconnection onset on the right. On the top are the grayscale cuts along the current sheet. The blue box surrounds the regions where $\partial/\partial x(v_{ix}) \geq 0.10$. Below are cuts of the variables along the white cut markers in the grayscale figures.

Tracing the X-Line

Unfortunately, classifying the reconnection as being in either the "fast" or "slow" configuration is only half of the difficulty. In general, x-lines grow or spread chaotically in the out-of-plane direction [Figure 27], much as one would expect a tree or root to grow. As such, cuts or slices 'along' the x-line are not necessarily straight, but rather they can bend or fork with the current flow. Consequently, it was also

necessary for us to develop an algorithm by which we could trace the x-line through its bends and weaves.

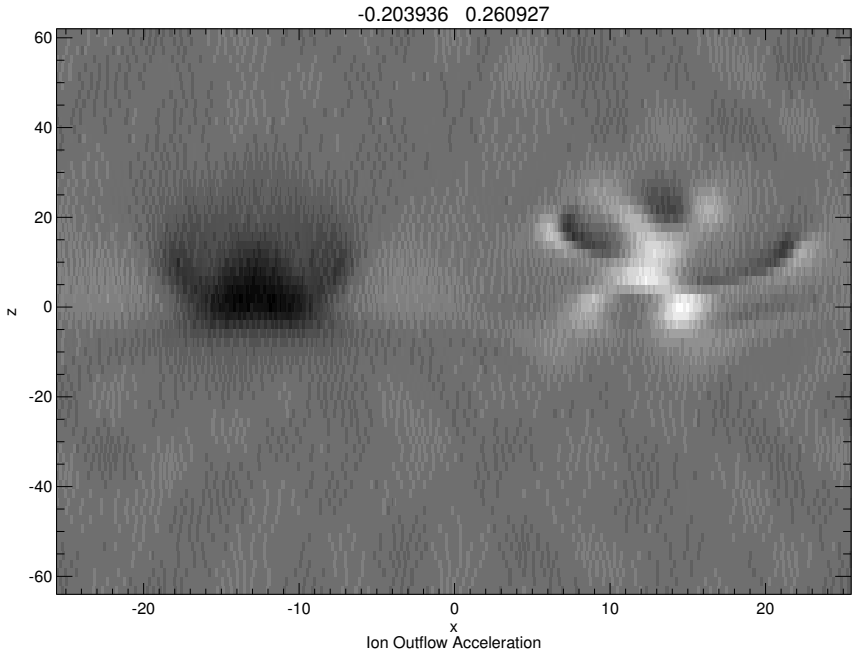

Figure 27 Plot of $\partial/\partial x(v_{ix})$ inside of a current sheet demonstrating a more complex x-line structure. White represents high values and black represents low values.

To attempt to trace at least one, but hopefully more, useable x-line paths from the forking reconnection structure, we developed an algorithm to trace the x-line by following the maximum ion outflow acceleration. This algorithm is presented in Figure 28 through Figure 32

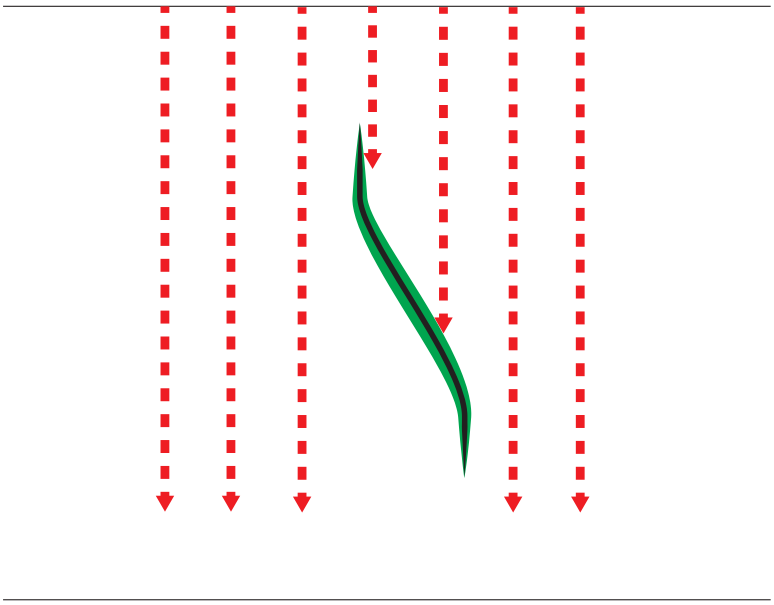

Figure 28 First step in the tracing process. At a particular time step, we search for regions where $\partial v_{ix}/\partial x \geq the\ slow\ reconnection\ threshold$. The search paths, depicted in red, begin at the top of the simulation (high z-value) and work their way down to the bottom of the simulation. In this diagram, two of the search paths have successfully found a region exceeding the slow reconnection threshold, which is represented by the green curve.

Tracing Step Two

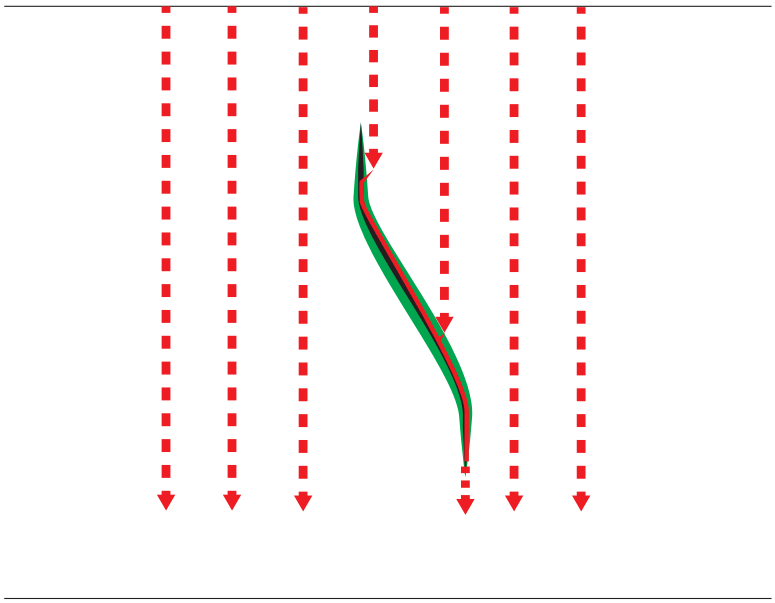

Figure 29 Second step in the tracing algorithm. Once a search path has successfully located reconnection, it begins to follow the maximum local $\partial v_{ix}/\partial x$ as it progresses down the simulation space, here local was defined as an adjustable parameter frequently set to c/ω_{pi}. The local maximum is represented by the black curve. The tracing of this local maximum is done in a solid red line. So for this time step, we have identified two tracing paths which have successfully located an x-line.

Tracing Step Three

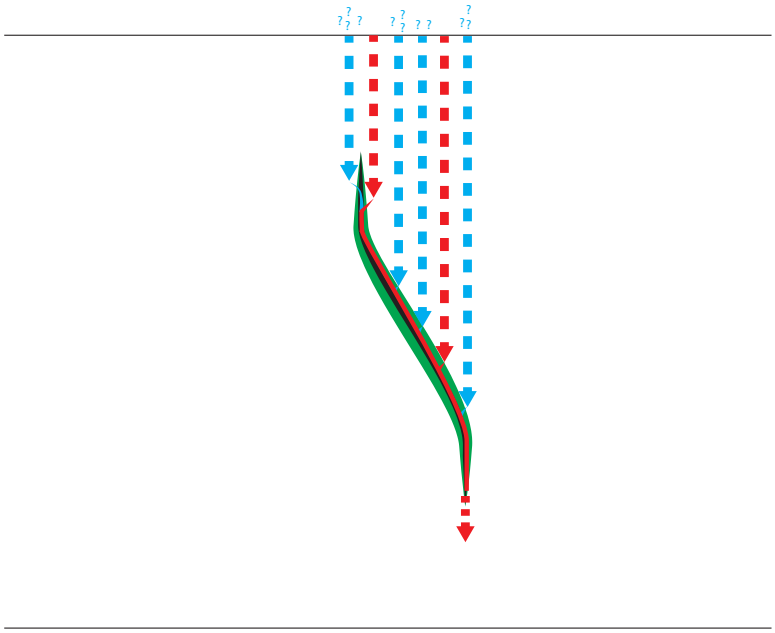

Figure 30 The third step in the tracing algorithm. As we can see in the previous step, although we had two tracing paths detect the x-line, one of the two seeds intersected it far from the beginning. In preparation for the search of the next time step, we assess whether or not we should move the starting point of the search paths to a new location. To do this, for every search path we create a two trial search paths to either side, depicted in blue. We measure the length of the x-line traced by each search path.

Tracing Step Four

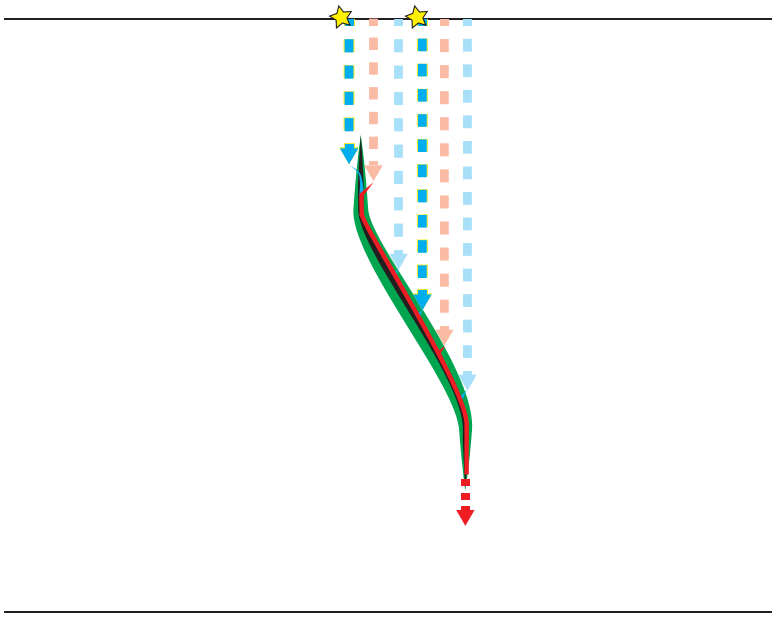

Figure 31 On the fourth and final step of the tracing algorithm, we assess which paths resulted in the longest x-line tracings. These longest paths, marked with a star here, determine the starting points for the search paths on the next following time step. This selection by length results in the search paths gradually migrating toward a complete x-line trace, along a particular fork.

Result of X-Line Tracing

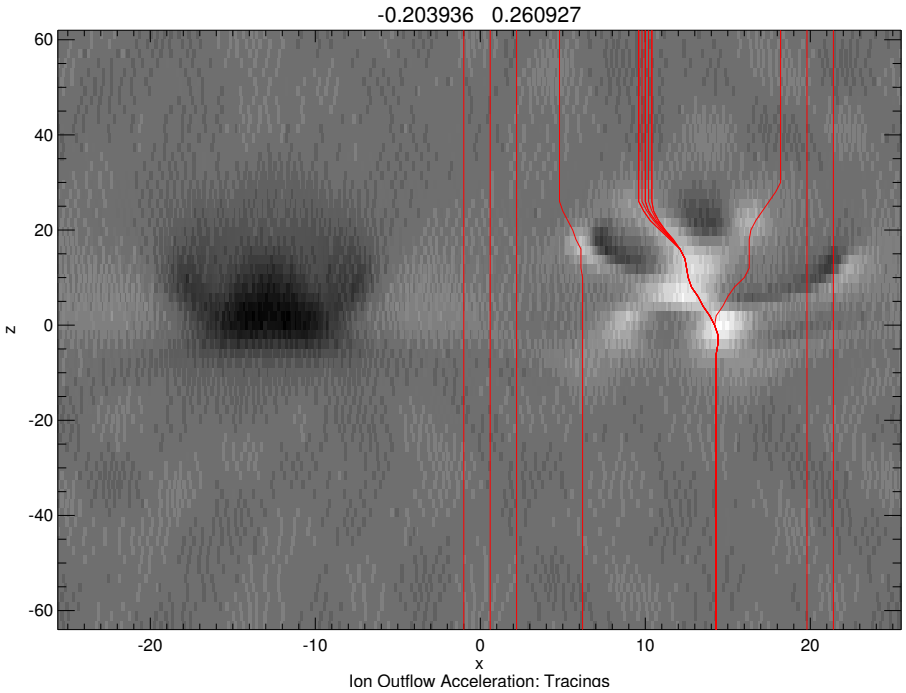

Figure 32 (105.3, t = 16) Example of x-line tracing algorithm. The grayscale plot presents the ion outflow acceleration while the red lines are the x-line traces.

After a run is processed like this, we evaluate the overall effectiveness of each seed at tracing a primary x-line from beginning to end. All analysis of our x-lines in this thesis occurs down one of these chosen paths.

Taking everything together, we've developed a system to trace 3D x-lines while roughly classifying the differing geometry of their diffusion regions as functions of z. This allows automatic tracing and calculation of the x-line paths in the next chapter, which is critical for understanding the time variation of finite length x-lines as well as the factors controlling their dynamics.

Chapter 4

3D STRUCTURE OF THE X-LINE

Contour Plots

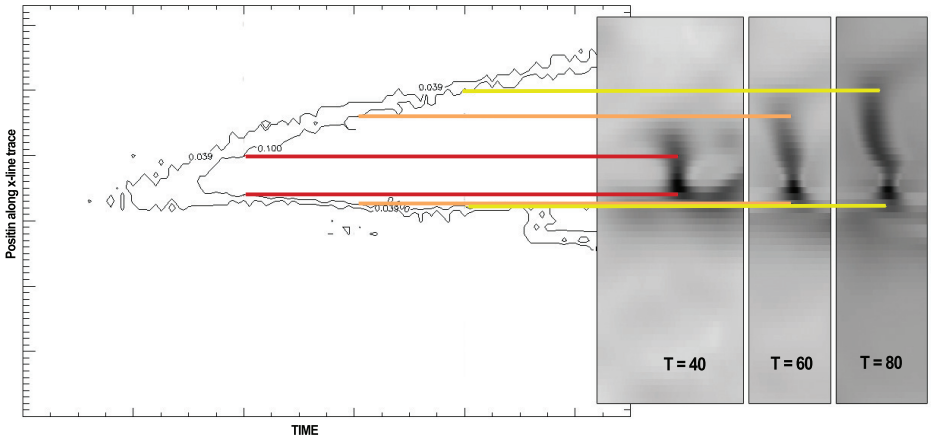

Figure 33 A new way of visualizing the spreading of the x-line in time. The canvas of the plot represents the x-line tracing at each time step. In this canvas, we have plotted a contour of the ion outflow acceleration. Those contours define the body x-line in time. To the right, we can see a comparison with current sheet at different time steps.

Using these techniques for tracing and classifying x-lines in time, we can create a novel plot of the x-line as a function of time, by taking a contour of the ion outflow acceleration. A typical example of this contour is see in Figure 33. The principle structure in this plot is a band of slow reconnection having an acceleration with a magnitude between .039 and .1. This band represents the transition region

separating the fast reconnection from the passive current sheet. The bottom of this band of the contour is what we have previously dubbed the 'south side' of the reconnection site. While the upper portion of the strip is what we called the 'north side.' Using plots like this, we can quickly identify the presence of reconnection, its growth rate, as well as whether it is predominantly slow or fast.

More physically the boundaries represent geometric transformations of the x-line. Progressing through the contours from left to right (or small values to large values): the first contour occurs when the current sheet has narrowed into a thin Sweet-Parker like configuration. So cuts of the current sheet before that contour would show a still narrowing current sheet with no magnetic flux conversion. After crossing the first contour threshold, reconnection begins. Traversing between the contours has the aspect ratio of the diffusion region shrinking until it reaches the fixed threshold value of $10c/\omega_{pi}$. Once it has reached that aspect ratio, we cross the final threshold into what we have termed 'fast reconnection.' It is at some point within this region that the outflow jets open up. Figure 34 is a schematic presenting this break down.

Figure 34 A breakdown correlating the in-plane reconnection geometry to the x-line contour. Regions in white correspond to regions where the current sheet is not yet narrow enough to support reconnection. The black band represents the transition region between 'slow' and 'fast' reconnection. It is in that region. In the yellow region the diffusion region has attained a fixed aspect ratio of approximately 10:1, which means that open outflows have developed.

Density

Reconnection can also be viewed as a plasma transfer system, where plasma from outside of the current sheet is injected into its interior. So long as the injection is slow, the low density plasma from the exterior is able to enter the current sheet and diffuse along the x-line, eventually finding rest in near homogeneity. In slow or resistive MHD simulations, this remains true through the lifetime of the reconnection site. However, after the onset of fast reconnection, the plasma injection increases to the point where the plasma in the current sheet can no longer diffuse into a uniform z-equilibrium. The rapid influx of low density plasma leads to the development of a density minima inside of the current sheet. Although this also happens in 2D reconnection, it does not play a significant role in dynamics of 2D reconnection. In 3D, this plasma injection produces a z-dependent plasma distribution which

subsequently develops pressure gradients along the x-line [Figure 35]. These gradients in turn drive significant plasma flows in the z-direction. In other words, the high density plasma to the north and south of the x-line are always trying to fall into the heart of the reconnection site. The minima location itself remains fairly stable through all of the simulation examples. It rarely moves from its starting location and often represents the location where reconnection is most vigorous and elder.

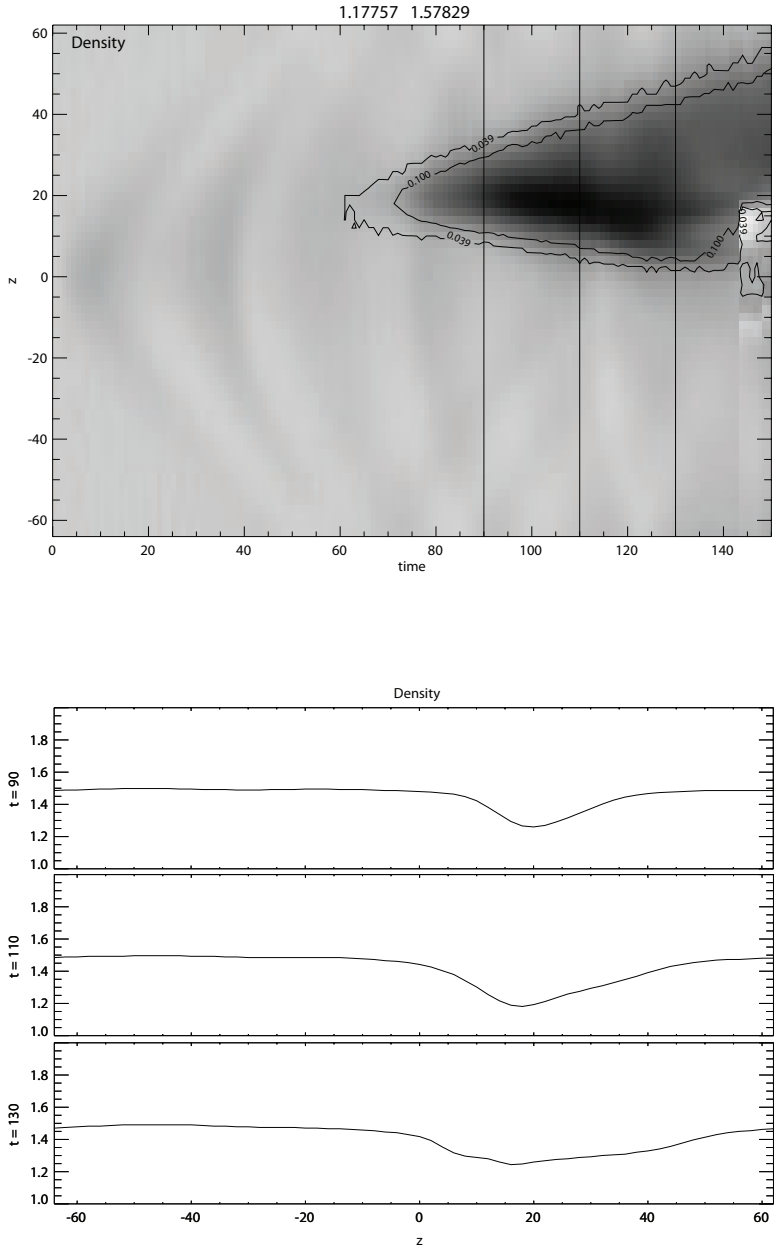

Figure 35 (107.46)(Top) Grayscale plot of the density within the x-line. The black contours represent the reconnection boundaries. The vertical lines represent the times where we plotted traces of the density. (Ladder Plot) The density along the x-line traces.

Z-Directed Force

In addition to the plasma density contributing to strong z-directed flows, there are other 'out-of-plane' forces at play inside of the current sheet. In Figure 36, we can see the two forces felt by the ions within the diffusion region. Foremost is the already mentioned gradient in the plasma density. In that figure, we see two prominent structures within the gradient. The first is a sharp gradient on the top of the graph corresponds to the north-side onset point. This fact that this gradient is co-located with the reconnection boundary suggests that pressure driven acceleration plays a significant role in the spreading of reconnection on the north-side. Secondly and not unexpectedly, the most significant plasma pressures can be found near the density minima, right in the heart of the x-line. The other force driving the ions, featured in the second figure, is the $\vec{J} \times \vec{B}$ force. The average ion gyroradius being roughly the size of the diffusion region, this average force can be felt by the plasma as it samples the current sheet wall - subsequently, the figure represents an average of the force over d_i. Considered one of the traditional players in 2D reconnection responsible for developing plasma flow in the z-direction, we see that this force is also well represented in 3D as well. Unlike the density gradient, $\vec{J} \times \vec{B}$ usually accelerates the ions toward the southern end of the x-line across the entire x-line length. In this particular plot, the anomalous northward contribution at late times is due to the interference of a secondary island. It's also important to note that this force is not present in the current sheet itself, since the magnetic field is so small near the neutral point.

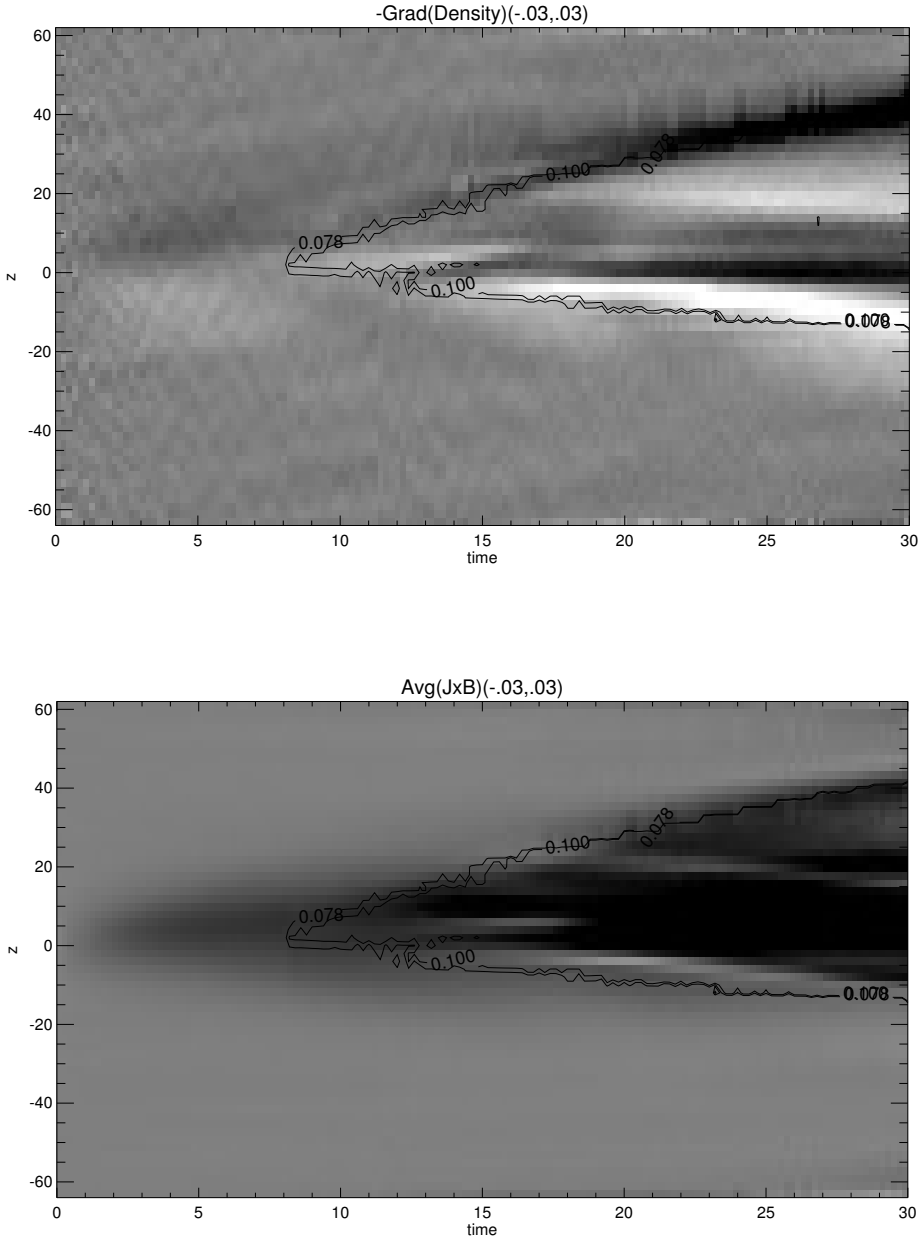

Figure 36 (105.3)(Top) Grayscale plot of $-\nabla_z \rho$ in the x-line. (Bottom) Grayscale plot of the $\vec{J} \times \vec{B}$ forces felt by the ions.

Combining the two forces, we develop a rough picture of the dynamics of the plasma flow in the z-direction. On the northern half of the x-line, the two forces work in collusion to drive the plasma flow southward. However, as the plasma crosses the heart of the reconnection site, the pressure gradient begins to work strongly against the plasma flow. This results in a rapid de-acceleration of the plasma flow on the south-side of the reconnection site. More than simply being a de-acceleration, as seen in Figure 37 it can lead to a complete arrest of the plasma flow.

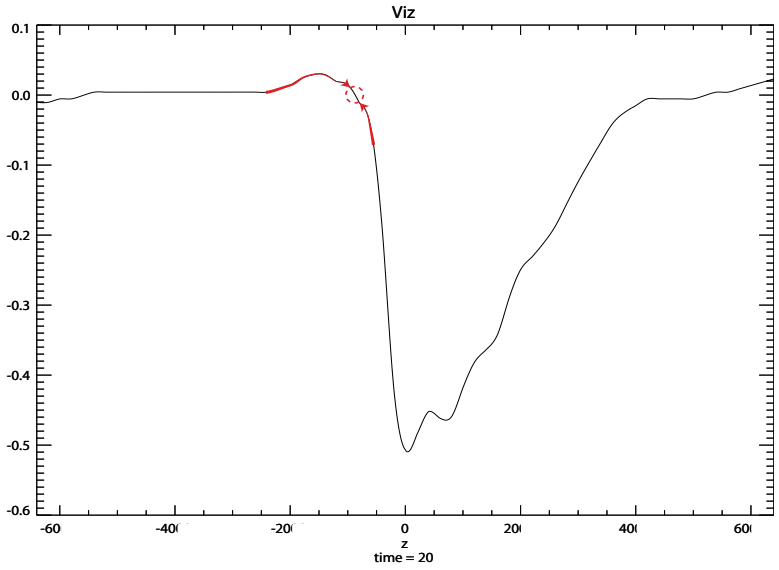

Figure 37 (105.3, t = 20) Ion flow in the z-direction taken along a trace of the x-line demonstrating the existence of a z-stagnation point.

The stagnation of the plasma flow doesn't simply happen sometimes. This stagnation point was present in every simulation we ran. Not only that, but it was also coincident with the south-side boundary in every run - both in the current sheet and in time. In Figure 38, we plot the x-line contours for 3 representative runs in black.

Overlaid in red is the $v_{iz} = 0$ contour. The stagnation point sticks closely to the southern boundary, even through interference from secondary islands. In Figure 39, we show a single time-step inside of the current sheet, where once again the velocity contour in red bends to match the south-side of the x-line. It even goes so far as to match the v_{ix} fishtail structure in panel 1. Clearly, the stagnation point on the southern end is an important player in the dynamics of 3D reconnection.

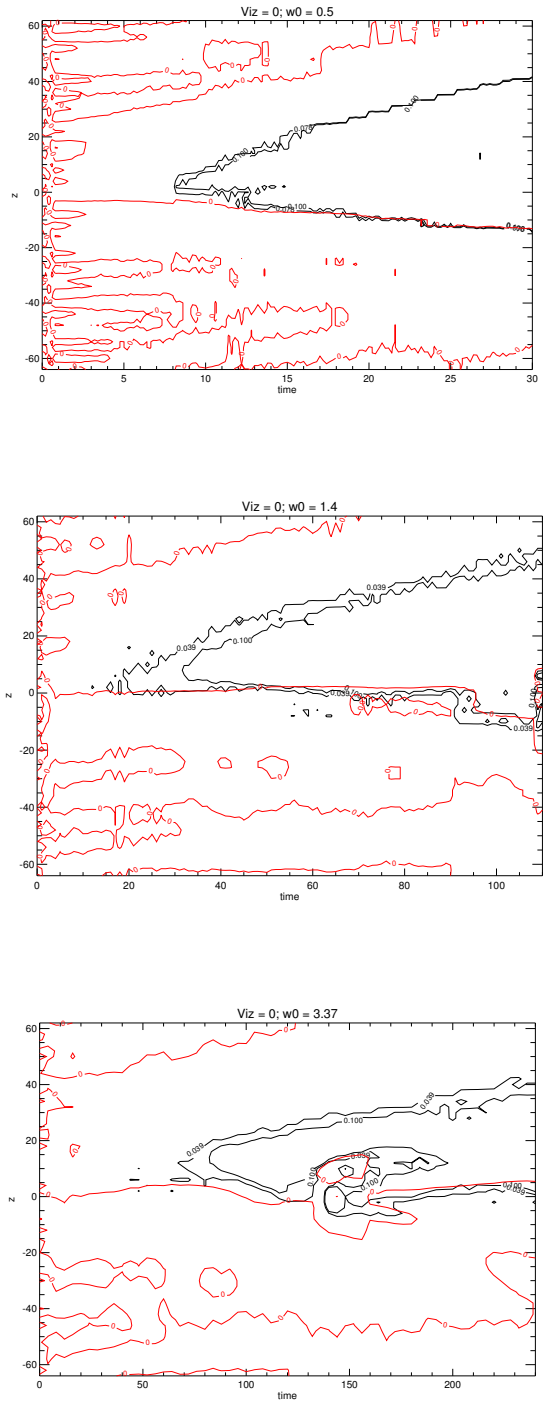

Figure 38 (105.3, 107.8, 107.6) In black for all figures are the ion outflow acceleration contours -- defining the reconnection boundaries. Coincident with the southern boundary in all 3 examples is the red contour representing the z-stagnation point in the flow.

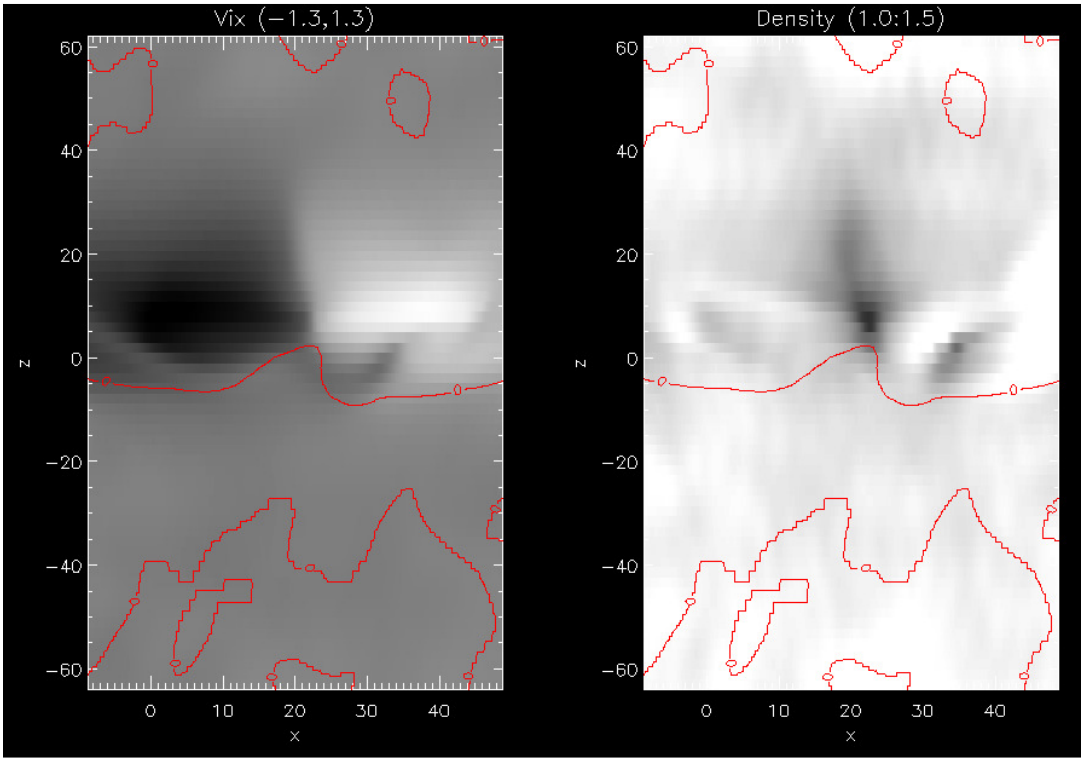

Figure 39 (107.8, t = 60) Grayscale plots within the current sheet with a red overlay representing the stagnation in the z-flow. Once again, the stagnation line conforms to significant reconnection structures.

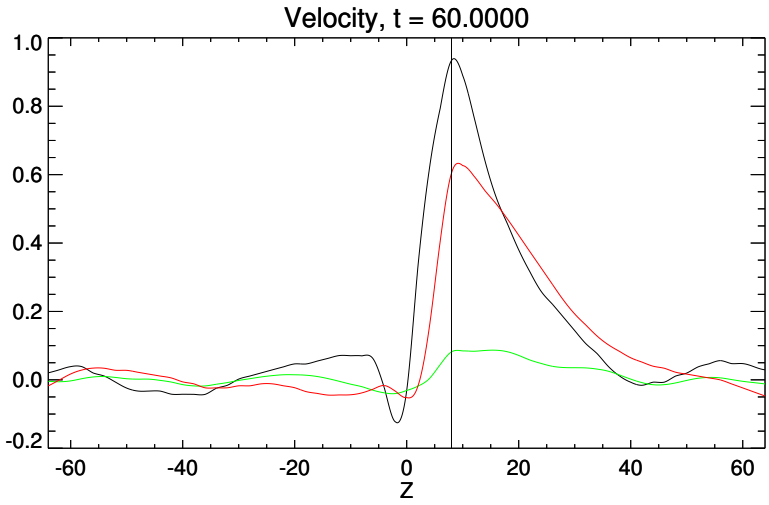

Figure 40 The velocities: v_x, v_y, and v_z as functions of z. In black v_x is measured just downstream of the x-line near the outflow edge of the diffusion region. In red, v_z is measured along the trace of the x-line. Finally in green, v_y is measured near the upstream edge of the diffusion region.

To round out our discussion of the structure of the 3D x-line, we present the other outflows and inflows in Figure 40. The highest intensity in the outflow coincides with the density minima. This makes perfect sense, since the minima is caused by plasma injection from outside the current sheet, the oldest and strongest part of the reconnection site should have the most reduced plasma density. Interestingly enough, the inflow from the y-direction crosses zero while there is still a substantial outflow present. Taken together, this suggests that the top half of the x-line is dominated by y-inflows, whereas the bottom half of the x-line is dominated by z-inflow. As a consequence, the some of the most intense outflow regions of an x-line may not have the most magnetic flux in the outflow.

This leads us to our completed picture of the 3D reconnection structure [Figure 41]. An x-line can be broken into 2 distinct domains. A northern and a southern half.

Bisecting the x-line into the distinct halves is the density minima. Above the density minima the pressure gradient works together with the reconnection forces to bring plasma in from the current sheet above. In this domain, the outflow will carry stronger magnetic fields, as the magnetic inflow is relatively high. It is this region that looks very much like typical 2D reconnection. For very long three dimensional x-lines this region forms the large majority of the x-line. Below the bisector, converging z-flows shut down the reconnection process stagnating any growth. The maximum outflow from the reconnection site occurs along the bisector, where both z-inflow and y-inflow can contribute strongly.

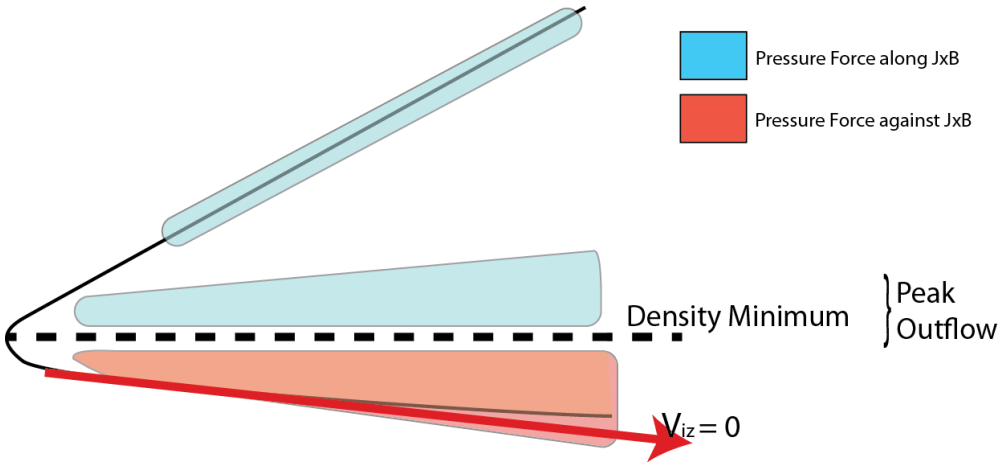

Figure 41 Diagram of the x-line structure in time. The black line represents the $\partial/\partial x(v_{ix})$ threshold defining the reconnection region.

Chapter 5

TRANSIENT RECONNECTION

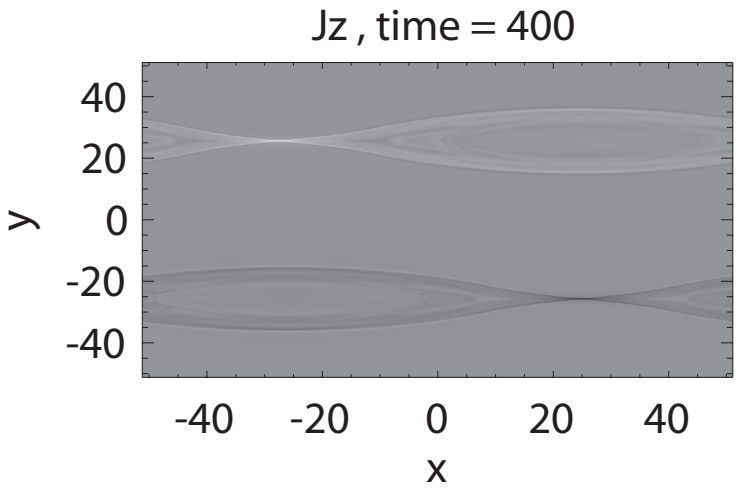

Figure 42 2D simulation where the perturbation amplitude, ε_0 is set to 0.03. Reconnection proceeds normally.

In all of the examples of reconnection we have used thus far, the x-lines have preferentially spread northward. This asymmetric spreading was observed to have a strong dependence on the equilibrium current sheet width, ω_0 in simulations by *Shay et al.* [59]. In this work, *Shay et al.* observed that narrower initial current sheets produced more rapid spreading than their more expansive counter parts. In the widest cases studied, the rate of asymmetric spreading had been reduced to the point of stagnation, i.e, the growth on the north side is offset by shortening on the south side,

leading to an x-line of fixed length. These stagnated x-lines, called solitary x-lines, drifted with the current sheet without growing or spreading. The decline of the x-line growth rate with large ω_0 suggested that there may be some threshold width beyond which reconnection is either unstable or cannot occur. In pursuit of this threshold value, we present a several simulations with $\omega_0 = 5.0$. First to establish a baseline or expected behavior we initialize this wide current sheet width in both a 2D as well as a sister 3D simulation. In 2D, as can be seen in Figure 42, this system reconnects normally. Furthermore in every 2D case ran, the reconnection process proceeds until all of the available magnetic flux is consumed. This behavior agrees with our expectation of 2D reconnection. However, in the sister configuration, which is fully 3D, the system ran for 3000 Alfven time units without showing any indication of reconnection. This is 10 times longer than the onset time demonstrated in the 2D case. However, when the initial perturbation size ($\mathcal{E}_0$) was increased from 0.03 to .06, the system did reconnect [Figure 43].

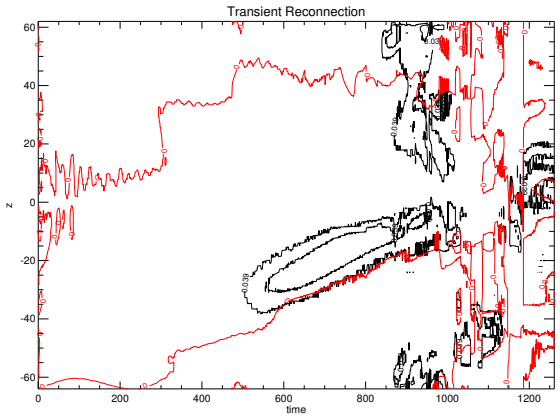

Figure 43 (107.34) An example of transient reconnection. Like before, the plasma stagnation point is plotted in red and the black contours represent the fast and slow reconnection boundaries.

Not only did the system reconnect, but the resulting reconnection was transient. Further varying the perturbation magnitude and volume resulted in table 2. Where we see that when ordered by the product of $\mathcal{E}_0$ and ω_{0z} that all of the runs with a value below 0.4 fail to reconnect and all of those with a value 0.4 and above successfully reconnect. This includes a run where the product was set to 0.38.

Run Number	Magnitude($\mathcal{E}_0$)	ω0z	Product	Reconnected?
107.29	0.015	10	0.15	no
107.31	0.03	10	0.3	no
1077.2	0.12	2.5	0.3	no
107.39	0.06	5	0.3	no
107.45	0.038	10	0.38	no
107.42	0.04	10	0.4	yes
107.41	0.05	10	0.5	yes
1077.4	0.24	2.5	0.6	yes
107.37	0.12	5	0.6	yes
107.34	0.06	10	0.6	yes
107.36	0.12	10	1.2	yes
107.30	0.24	10	2.4	yes

Table 2 Table of runs with marginal initial conditions. The product of $\mathcal{E}_0$and ω_{0z} is positively correlated with the system's instability to reconnection.

These two conclusions taken together are very interesting. The fact that there is a mechanism by which reconnection can become a transient instability, without consuming all the available flux, is very interesting. This transient reconnection could be responsible for transient magnetotail flows such as bursty bulk flows (BBFs). Secondly, the instability of this current sheet to reconnection seems to depend on the product of the perturbation magnitude and the extent of the perturbation in the out of plane direction. Since the perturbation energy scales with the product of those terms (6), this suggests the existence of an activation energy for 3D reconnection. To gain more insight into the physics behind this behavior, we inspect the most marginal example of reconnection having a perturbation magnitude of .04 [Figure 44].

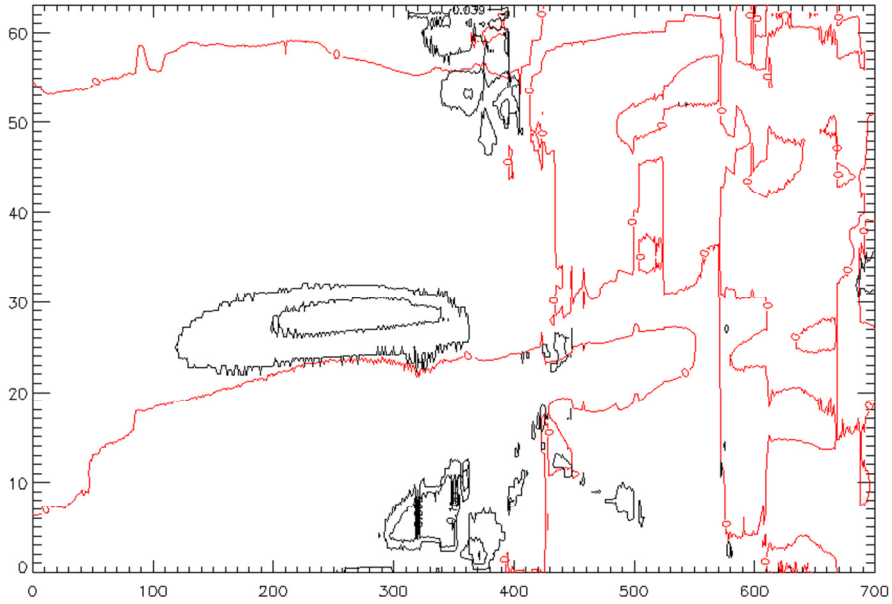

Figure 44 (107.42) The most marginal example of reconnection.

The first thing of note about even this 'most marginal' reconnection example is that it has the presence of both fast and slow modes. So regardless of how difficult it is to begin hall reconnection, it appears that once begun, reconnection always configures into a fast reconnection diffusion region geometry. Therefore the energy costs for the activation of reconnection must occur in the geometry transformations before the onset of slow reconnection. Secondly, we can see that like the previous sections, the presence of a v_{iz} stagnation point is coincident with the southern reconnection boundary. The presence of a stagnation point along the southern boundary indicates that even in the weakly reconnecting regime, the out of plane pressure gradient is a significant player in the dynamics.

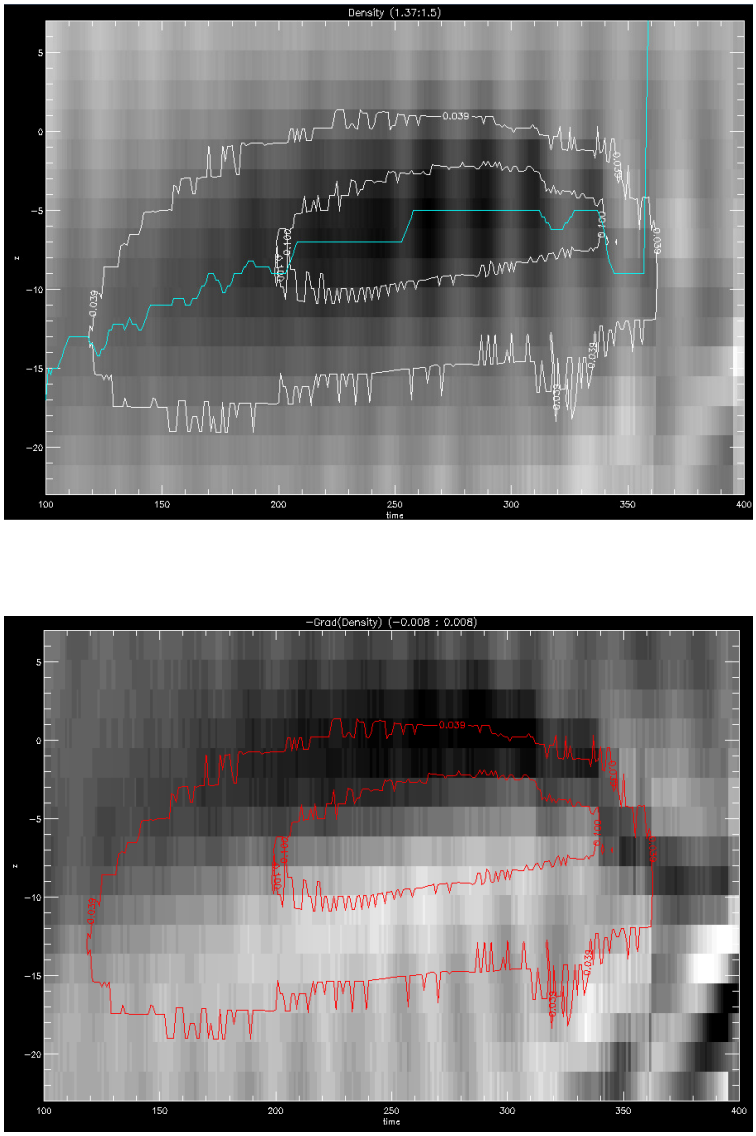

Figure 45 (107.42) (Top) Density grayscale. Overlaid in blue, the location of the density minima. (Bottom) Grayscale plot of $-\nabla_z \rho$. The boundary contours are over-plotted in red to ease visibility.

Investigating the contribution of the density gradient to the marginal x-line dynamics, Figure 45 shows that a significant rarefaction of plasma density is aligned with the x-line in time. From our previous discussion on the structure of 3D

reconnection, we claimed that the density minima typically was found toward the bottom end of the reconnection site. However, in this more marginal example the density minima (indicated by the cyan line) is centrally located in the x-line. In the second panel, we see the pressure gradients we would expect within the x-line -- they work to move the ion fluid elements inside the diffusion region toward the heart of the x-line. Parlaying this into an inspection of the average electromagnetic force: $\vec{J} \times \vec{B}$, in Figure 46, shows a radical departure from the *typical* 3D x-line viewed before. Instead of contributing to a net ion flow southward throughout the bulk of the x-line, it acts neutrally in the early life of the x-line. Later in the x-line's life, this affect grows very strong and is directed oppositely from our previous experience. Since this affect coincides with the termination of the reconnection process (340 < t < 360), it's worth spending some time understanding what it is.

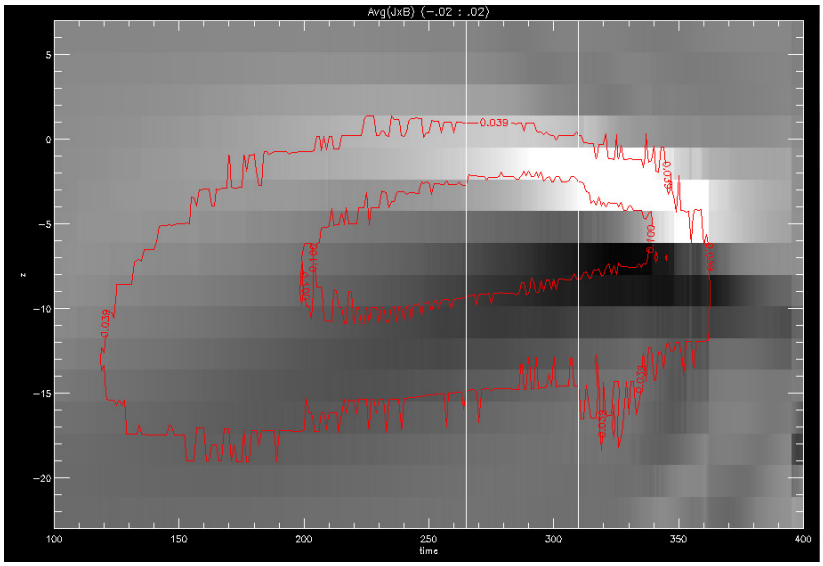

Figure 46 (107.42) Grayscale plot of forces felt by the ions: $\left(\vec{J} \times \vec{B}\right)_z$. The vertical white lines demark the point where the spreading of the x-line is arrested and then collapses.

If we revisit the forces felt by a fluid element of ions due to the electromagnetic effects,

$$\vec{F} = \frac{\vec{J}}{\mathrm{nc}} \times \vec{B}.$$

We can substitute,

$$\vec{J} = \left(\frac{\mathrm{c}}{4\pi}\right)\vec{\nabla} \times \vec{B},$$

to get:

$$F_z = \left(\frac{1}{4\pi \mathrm{n}}\right)\left[\left(\partial_y B_z - \partial_z B_y\right)B_y - \left(\partial_z B_x - \partial_x B_z\right)B_x\right].$$

In 2D reconnection as well as the stronger 3D reconnection seen earlier, it is the first term, $B_y \partial_y B_z$, which leads to the strong plasma flow from north to south. This physics comes into play when the two-scale structure of the diffusion region allows the frozen-in electrons to pull the magnetic field in the out-of-plane direction. This structure is mostly, but not completely, absent from these marginal reconnection examples. The term which appears to be strongly present and correlated with the collapse of the x-line is instead:

$$F_z \sim -B_x \partial_z B_x$$

To understand the effect that this term has on the reconnection structure, consider that this is derived from a fluid equation. It represents the force applied to a fluid element by the electromagnetic fields. In this case, the force is located on the northern side of the reconnection region and is directed away from the x-line. This can be seen in the diagram in Figure 47. For our purposes, it's not necessary to calculate the exact force felt. Rather a rough understanding of this process paints a sufficient picture.

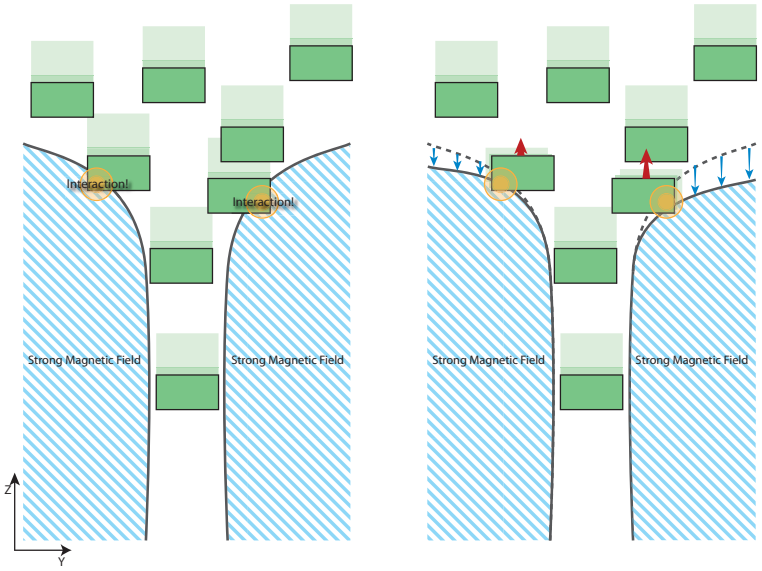

Figure 47 Schematic of the forces felt by a Larmor radius sized ion fluid element (green squares) as they enter the narrow passage of a thinning current sheet in the Y-Z plane. The solid black lines represent the magnetic walls bounding the current sheet. In the second figure, roughly representing the 'later' time step, the dashed line represents where the location of the bounding wall before the interaction. The region of *strong magnetic field* has a magnetic field pointed into and out of the page. During the process, the ions feel a force directed upward (red arrows). The walls of the current sheet feel a reactive force directed downward (blue arrows). The reactive force widens the current sheet.

The ion fluid element feels an upward force when it is pressed against the funnel-like opening of the northern x-line. We know from basic physics that the magnetic field must experience an opposing reaction force. This force, the force of the ion fluid element applied to the magnetic bottle, works to open up the aperture of the x-line. In essence, this is symptomatic of the collapse of the x-line rather than the cause.

To investigate the cause of the collapse, we return to Figure 46, where we have marked two times with white vertical lines. In every case of dying reconnection, the

same basic structure appears. Reconnection persists for a while, then at some point the northward spreading of the fast x-line is arrested. We can see by the first time marking, this occurs around the t= 265 mark. Once this occurs, there is a small time window before a dramatic collapse of the x-line, as seen around t=310. After this small time window expires, the fast reconnection completely shuts off. Keeping these timings in mind, we'll inspect the dynamics with respect to time.

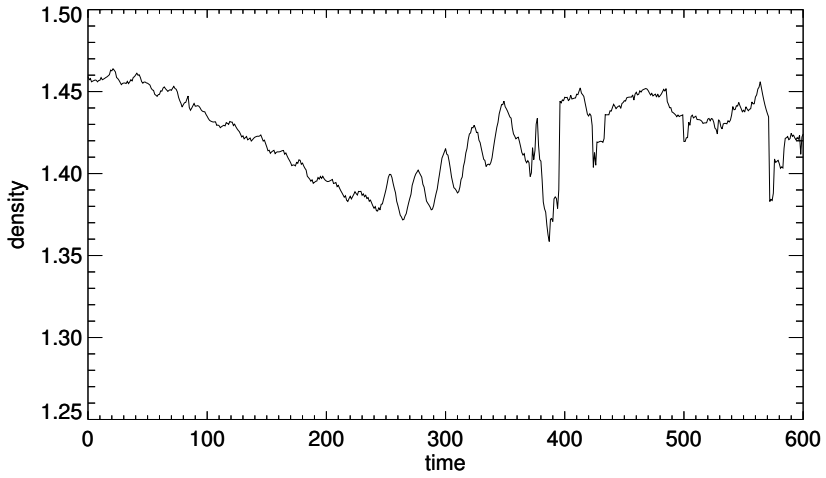

Figure 48 (107.42) Density minimum within the x-line as a function of time.

We begin by looking at the density, since it appears to be the only player in the north-south dynamics [Figure 48]. The density decreases monotonically until approximately t=250. At which point we can see two changes in its behavior. Most

notably is that the density begins to oscillate fairly strongly. Although this is interesting, this strong oscillation did not appear in every simulation so it's unlikely to be the cause of the collapse. More subtly is that the density minima itself reaches a minimum value then reverses direction.

In all of the cases of reconnection we have seen previously, the plasma outflow was always greater than or equal to the plasma inflow. This reversal represents a significant change to the reconnection dynamics. This change in behavior appears before any of the visual structural changes to the x-line. So we inspect the plasma flux into the reconnection site, looking for a change in behavior occurring at or before t=250.

To measure the flux entering the x-line, we chose a box measuring 10 c/ω_{pi} in the z-direction, 10 c/ω_{pi} in the outflow direction, and 1.4 c/ω_{pi} in the inflow direction and placed it around the most intense part of the reconnection site. The plasma flux into and out of the box was integrated along each of the six surfaces of the box. Each pair of sides was summed to give the net plasma flux along the inflow direction, the outflow direction, and the out-of-plane direction. The box was held fixed in space and did not attempt to track the x-line in the x-direction. Although a fixed geometry would be inappropriate for most x-lines, this particular x-line moved very little.

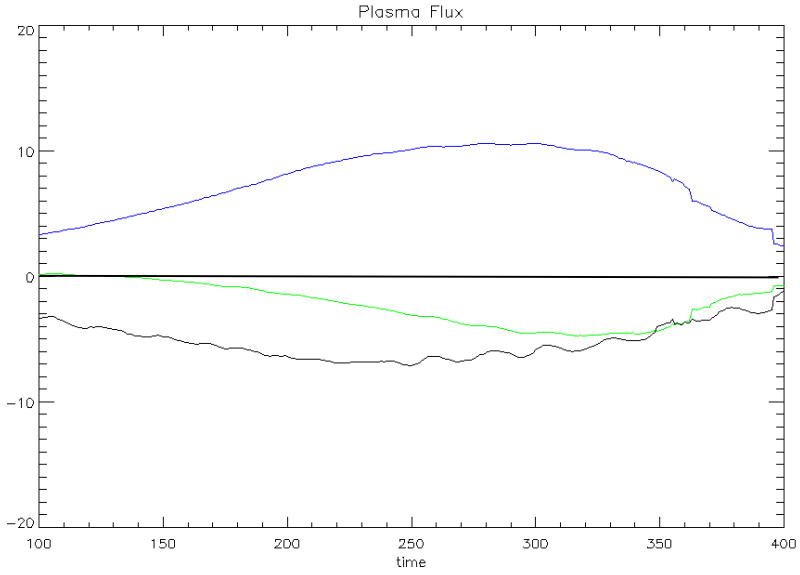

Figure 49 (107.42) Plasma flux entering and leaving a bounding box surrounding the x-line. Each color represents the flux along a coordinate direction. In blue is the flux leaving the region through the $\hat{x}$-facing surfaces. In green is the flux entering the region through the $\hat{z}$-facing surfaces. Finally, in black, is the flux entering the x-line through the $\hat{y}$-facing surfaces.

In the graph [Figure 49], the blue line depicts the integrated plasma outflow flux, the black line the traditional inflow flux, and the green line presents out-of-plane inflow flux. Reconnection is an outflow driven process; highly bent magnetic flux ropes undergo a contraction from the x-line to the o-line, as this is done they pull fresh plasma into the x-line. In two dimensions, the plasma pulled into the x-line comes from outside of the current sheet and as such is heavily laden with magnetic flux. In this sense it is self-sustaining. Because that magnetic flux is what is then unwound, driving the process onward.

The plasma flux in Figure 49 is initially like this. Since the initial z-inflow is very small, the plasma for the outflow is completely fed from outside of the current sheet. However, in time, the pressure driven inflow begins contribute a significant amount of plasma to the reconnection process. At first, the outflow can easily accommodate the additional influx. This cannot remain true indefinitely, since there is a physical limit to how quickly plasma can leave the system. Since the timescales over which the density within the x-line can change are much slower than the timescale of the reconnection process, the pressure driven inflow begins to supplant the inflow brought in from outside the current sheet. This is apparent from the fact that of the 3 graphs of plasma influx, it is the black curve which reaches its peak first. Occurring when t=225, this is the earliest indication of the imminent x-line collapse. The reconnection is not sustainable in this state. Since the process is still ongoing, all of the processes which were resulting in the rarefaction of the plasma are also ongoing. The z-influx continues to rise, magnetic influx begins to fall, and the outflow begins to suffer.

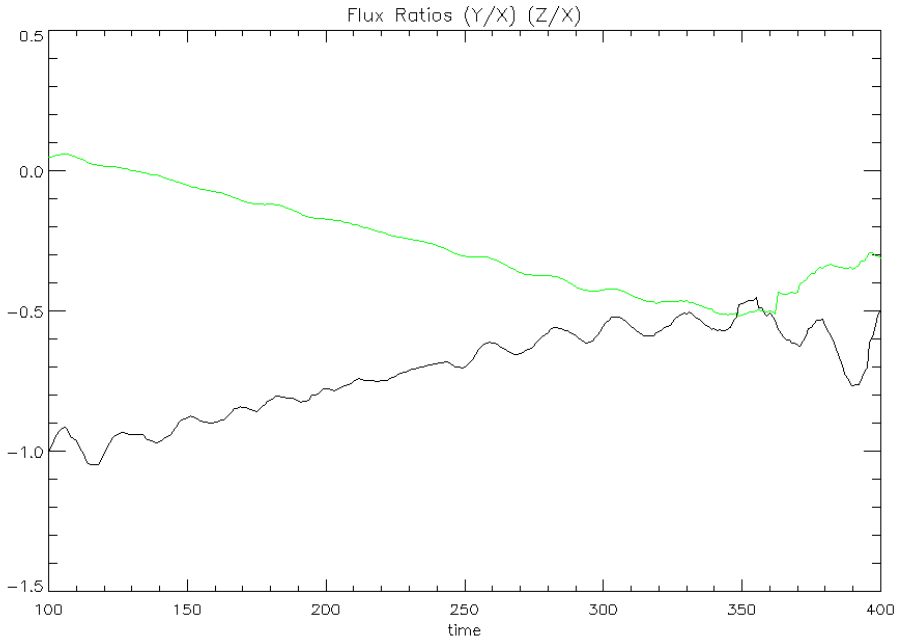

Figure 50 (107.42) Ratio of incoming plasma flux over outgoing plasma flux. In green is the ratio of z-influx over the outflow. In black is the ratio of y-influx over the outflow.

To see this more clearly, Figure 50 depicts the ratio of different inflows to the outflow. In green, is the ratio z-inflow/outflow. In black is the complementary ratio where the inflow is laden with magnetic energy. Knowing that the energetics of the outflow depend critically on the magnetic inflow, this graph makes it clear from even a very early time, that the reconnection must be transient. At approximately t=350, over half of the plasma outflow will come from a non-magnetic contribution. This is also when the x-line catastrophically collapses.

It is possible that the magnetic influx, instead of being inhibited, is reaching some sort of natural limit. To check for this, we looked at the inflow velocities for the different directions [Figure 51]. Here we have the outflow velocity colored black, the y-inflow velocity colored green, and z-inflow velocity colored blue. Initially, all

three velocities grow together. However around t=200, we can see that the y-velocity begins to be inhibited. Instead of approaching an asymptotic limit, it peaks and declines (depicted is $10v_y$ to make it visible on the same graph). This occurs very early in the lifetime of the reconnection. It occurs before the density minima. It also occurs before the emergence strong $\vec{J} \times \vec{B}$ forces.

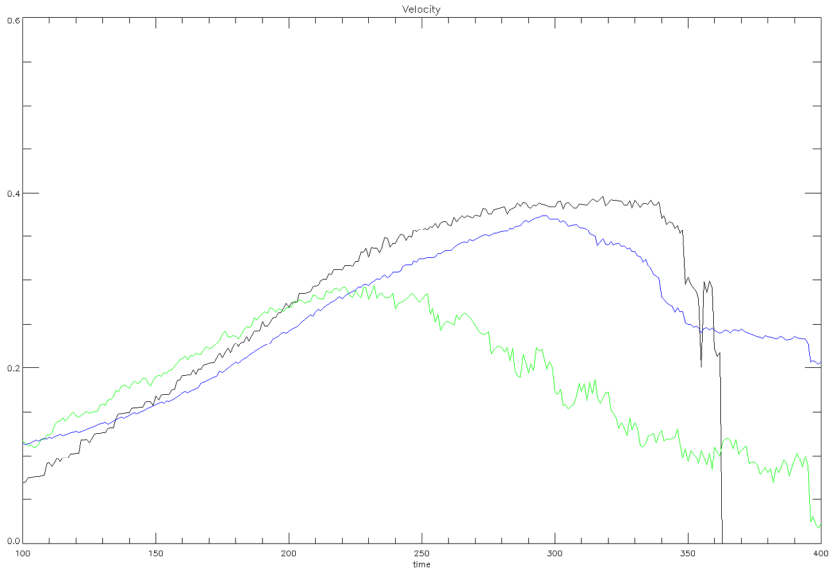

Figure 51 (107.42) Inflowing and outflowing velocities. Black, blue, and green are in the $\hat{x}$, $-\hat{z}$, and $\hat{y}$ directions, respectively. The z-flow was measured in the x-line where the density was at a minimum. The x-flow was measured 10 c/ω_{pi} downstream from the density minimum and the y-flow was measured 2 c/ω_{pi} upstream of the density minimum.

Taking everything together, a very clear picture of transient reconnection becomes apparent. When fast reconnection occurs, the quick injection of low density plasma from outside of the current sheet results in the formation of a density minima. So long as reconnection proceeds, this minima becomes more significant - driving

stronger and stronger out-of-plane ion flows into the heart of reconnection from the north side.

Because of the demands of continuity, this additional inflow needs an outflow. Until it has been dealt with, no additional magnetic flux can enter the system. So long as the outflow is un-throttled it can process the y and z inflowing plasma and reconnection can continue unfettered. However, as the outflow approaches its maximum speed, any increase in pressure driven flows can only come at the expense of the magnetic inflow.

The various plasma inflows, Φ_i, all scale with different pieces of the reconnection geometry,

$$\Phi_z = \rho v_z L_x L_y,$$

$$\Phi_y = \rho v_y L_x L_z,$$

$$\Phi_x = \rho v_x L_y L_z.$$

The in-plane reconnection geometries, L_x and L_y, are fixed in time. So that as the x-line spreads in the z-direction, the contribution to the flux balance from the pressure driven flows will be diminished -- stabilizing the reconnection process. Furthermore, since the development of strong pressure driven inflows is inevitable, the system must spread beyond a minimum size in the z-direction in order to survive.

Chapter 6

STEADY STATE MODEL

With the stability of marginal reconnection depending so heavily on the flux dynamics, we similarly inspect the more stable reconnection systems. We expect the pressure driven flows to have little effect on the gross behavior of the x-line, since as the system spreads into the out of plane direction, its behavior should approach the behavior of a 2D x-line.

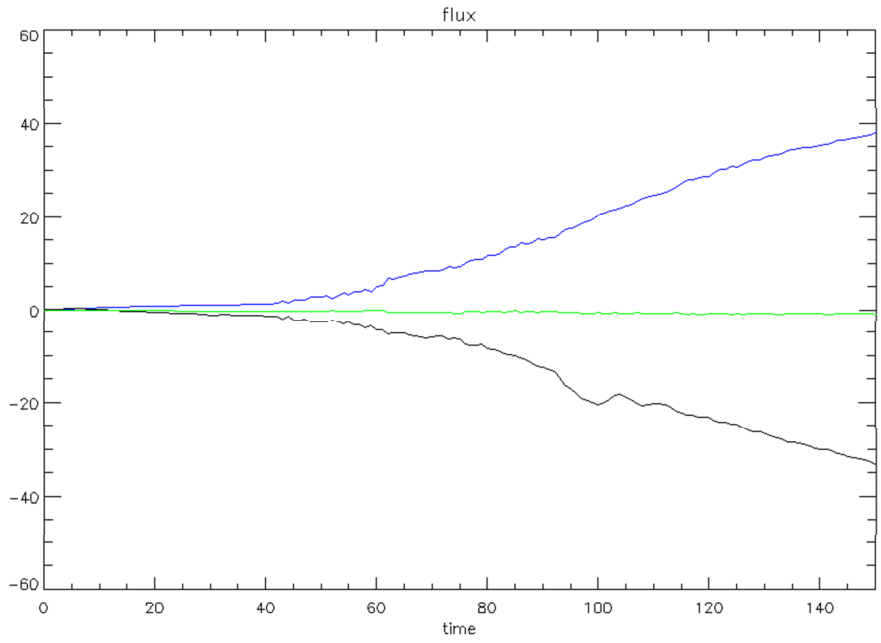

Figure 52 (105.3) Plasma flux entering and leaving the x-line. The bounding box spreads with the x-line in the z-direction. Outflow($\hat{x}$) is in blue. The in-plane inflow($\hat{y}$) is in black. The pressure driven flux ($\hat{z}$) into the system from the out-of-plane direction is in green.

We see on our most quickly spreading run, on aggregate this is true [Figure 52]. The figure represents the total flux entering the x-line as a function of time. In green, it can be seen that there is little flux entering the x-line from the north. Most of the flux enters the x-line from the y-direction (black) and passes out through the x-direction (blue). Although true enough to get a rough estimate of the total flux into and out of the x-line, this figure should be taken with a grain of salt. As we've already discussed, the reconnection system spreads, winds, and forks in time. Because of this, the bounding box through which we are measuring the flux also bends and grows in time. A proper accounting of flux would take into account flux which passes through the bounding walls due to the motion of those walls. We neglected that nuance.

We know from our previous discussion in Chapter 4 that the x-line has significant out-of-plane structure which is unrepresented in the aggregate posed in Figure 52. In order to investigate this structure, we turn to figures involving flux as a function of the out-of-plane coordinate, z. To do this we created enough 10x10x1 boxes to span the system in the z-direction and measured the flux into and out of these boxes individually at each time step.

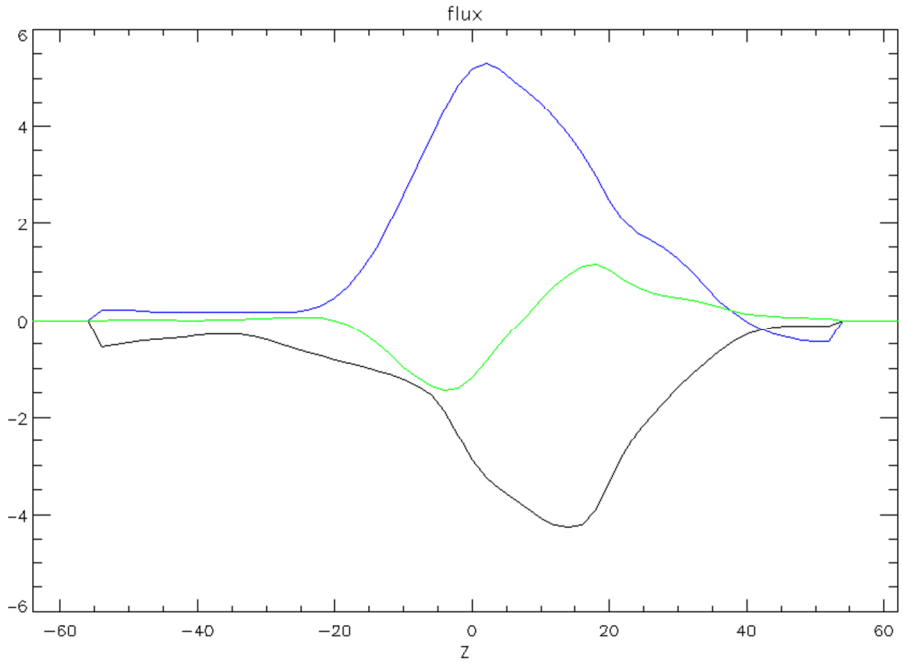

Figure 53 (105.3) Plasma flux as a function of position along x-line trace. In blue, green, and black are the x, z, and y directed fluxes.

Figure 53 is an illustrative example of what we found in the same run as our previous figure. Taken early in the life cycle of Figure 52(t=14), it shows the z-directed plasma flux as a function of z in green. Although the net out of plane flux is zero, we can see that internally there is a transfer of plasma from the northern half (high z-values) to the southern half (low z-values). The other two fluxes in blue and black are consistent with what we expect from our overview in Figure 52. The net behavior of x-directed flux , in black, is that of an outflow and the y-directed flux, in blue, is an inflow. However, there are some interesting things to note about the internal structure of both. For example, in the case of the y-inflow, the peak occurs further north than the x-outflow peak. In fact, the steepening of the slope and peak are coincident with the steeping and peak of the green curve as opposed to the expected

black curve. This suggests that excess plasma leaving the north side because of the pressure imbalance along the x-line results in a significant enhancement of inflow plasma from the y-direction. Even more surprising, if we look further north to $z = 50$, we see that the traditional outflow variable has the wrong sign. This means that the x-direction is actually serving as a plasma inflow channel. And it's serving this role in the very region responsible for spreading the x-line. Taking into account that this particular x-line was from our most rapidly spreading simulation (105.3), it suggests that the continuity requirements imposed by the z-directed flux is an aspect of healthy x-line spreading. The fact that it was necessary for the system to bring plasma flux in from the x-direction means that the y-inflow channel was already saturated – a saturation which provides the freshly spreading x-line with the magnetic energy it needs to establish itself.

However, as beneficial as this can be for the formation of reconnection on the north side, the south side must eventually pay back this 'loan' of plasma flux. Instead of enhancing the reconnection process, the additional z-flux can inhibit the south side's ability to draw in plasma from outside of the current sheet.

This leads us to a first model for steady state 3D reconnection [Figure 54].

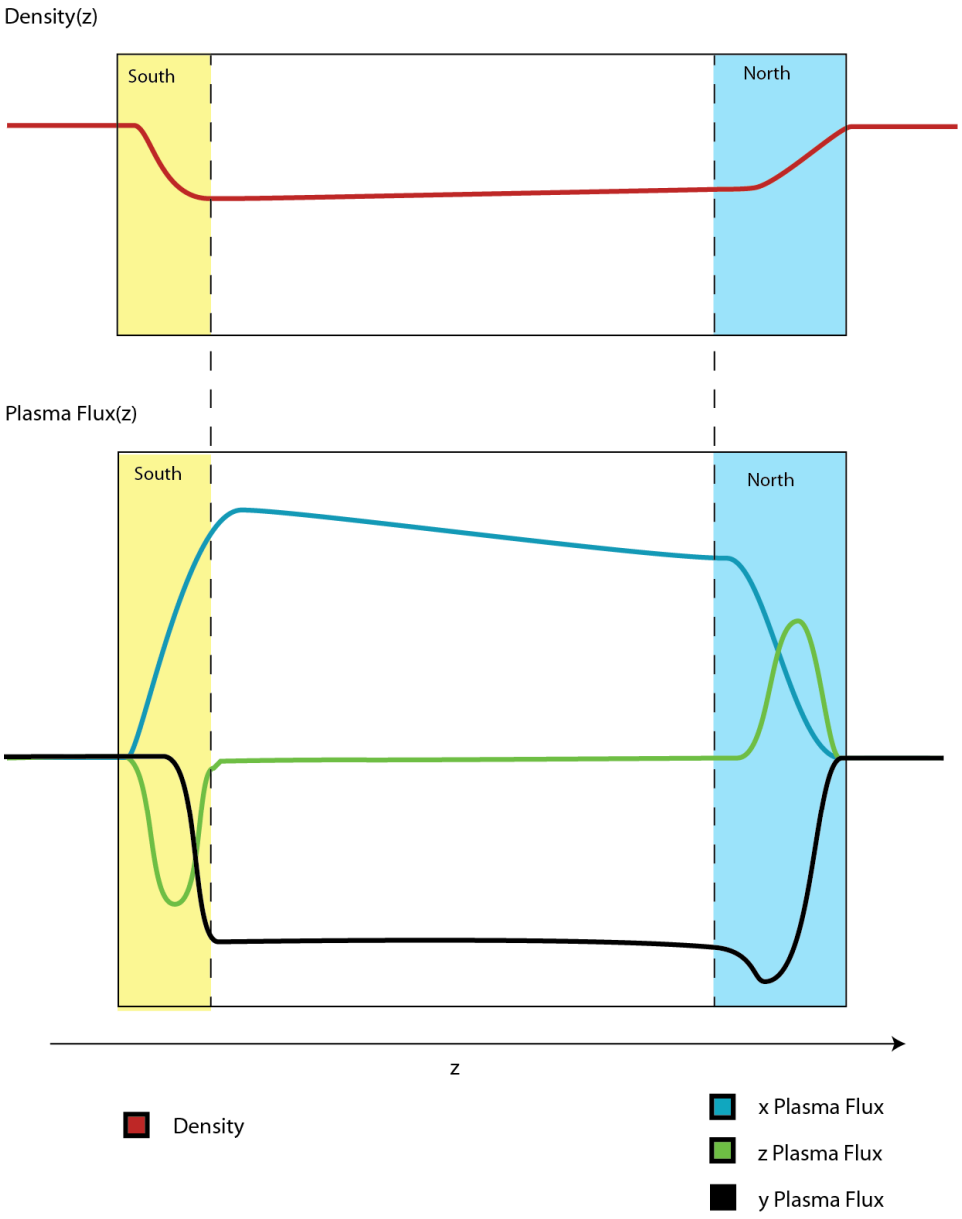

Figure 54 Parameters for an idealized 3D x-line.

In the figure we present the three regions along the x-line which play a significant role in reconnection process. In a sense, this figure is an idealized version of what was seen in Figure 53. In steady state reconnection, there will be a northern region, depicted in light blue, where the plasma density will suddenly drop. The drop in density is shown as the red line in the upper figure. This drop in density will aid with the rapid acceleration of the ions toward the southern end of the x-line. As we saw in Figure 53, this acceleration will enhance the traditional plasma inflow. Across the intermediate area, reconnection will be assumed to be 2D-like. The x-outflow will be derived from the inflowing magnetic flux. Meanwhile, the pressure driven flow acts as a spectator through this section of the reconnection, passing through the plane of reconnection without influencing the reconnection dynamics. On transitioning to the southern region, depicted in yellow, we once again see a large density gradient. This density gradient halts the z-directed ion flows, leading to our previously mentioned stagnation point. In other words, the south side has a large ion inflow from the z-direction without a corresponding z-outflow. By continuity, this influx needs to go somewhere. It goes to the x-direction, saturating that channel and leaving little room for magnetic rich y-inflows. By inhibiting the inflowing flux from the y-direction, the reconnection in that region is denied necessary magnetic energy needed to sustain itself.

In a steady state situation, the three principle movers of the dynamics are the conservation of energy, the continuity of the plasma, and the conservation of momentum. In order to build upon this model, we'll be focusing our attention on the first two.

Continuity

Conceptually, the continuity equation is simple. It says that in general, things do not appear or disappear. In order for an object to be somewhere, it must have traveled there from somewhere else. Like most objects we are familiar with, plasma also behaves this way.

Taking a car tunnel as an example, if an observer views a number of cars entering the tunnel, but fewer cars leaving the tunnel, the observer can conclude that the number of cars inside of the tunnel is increasing in time. Since the number of cars inside of the tunnel is changing in time, it is not in a steady state. However, if the number of cars inside of the tunnel must stay the same (or roughly the same), then the number of cars leaving the tunnel, must equal the number of cars entering the tunnel. In which case, steady state has been achieved. Likewise, when our system is assumed or observed to be in steady state, any plasma entering a region must be balanced by the same amount of plasma leaving the region. Mathematically, this can be expressed simply as:

$$\rho_{in} v_{in} A_{in} = \rho_{out} v_{out} A_{out}. \tag{12}$$

Or this is expressed more formally as:

$$\oiint_S \rho \vec{v} \cdot d\vec{S} = 0.$$

For the most part, in our reconnection system, the x-direction is always an outflow and the y-direction is always an inflow. And depending on whether or not we are discussing the north or south side of the x-line, the flow in the z-direction can be considered an inflow or an outflow.

Energy

In an isothermal system, the steady state does not invoke the simple rule of 'what goes in must come out.' Instead, energy flowing into the system does work or has work added to it before leaving through an outflow channel. In the simple example of a standing density shock, an inflowing gas must be compressed as it passes through the shock front. The energy consumed by the compression process results in an outflowing gas which is less energetic. So in the isothermal steady state,

$$Energy\ In = Energy\ Out + Work$$

However, if the system is to remain in a steady state, the amount of energy lost or gained through work must remain constant.

As for the energy itself, the transport of it is mainly carried by two effects. The first effect is the kinetic transport of energy by the plasma body itself. As the plasma moves, it carries kinetic energy with it. The other mechanism by which energy can enter or leave the system is through the convection of the magnetic field. As the electron plasma enters or leaves the system, it drags magnetic energy with it.

So the energy transport through a flux boundary can be expressed as,

$$\left(\frac{1}{2}\rho m_i v_{in}^3 + \frac{B^2}{2}\mathbb{v}_{in}\right)A_{in} = \left(\frac{1}{2}\rho m_i v_{out}^3 + \frac{B^2}{2}\mathbb{v}_{out}\right)A_{out} - W_{compression}.$$

The electron velocity is represented by $\mathbb{v}$ and the ion velocity is presented with the standard v. In most cases, the electron moves with the protons so the velocities are typically equal.

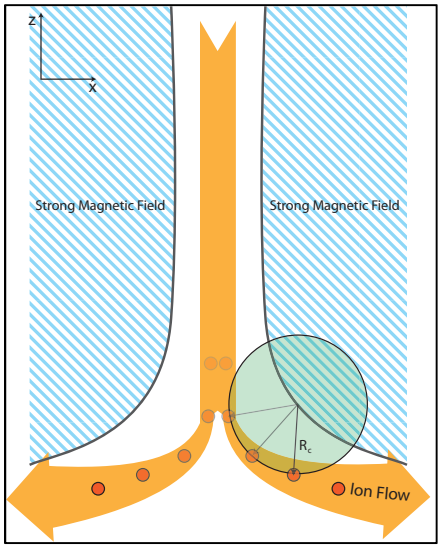

Figure 55 Schematic showing the ions turning the corner at the southern end of the reconnection site. The region denoted by the light blue lines indicates current sheet walls. In those walls, the magnetic field is leaving or entering the page. Between them is the current sheet itself.

Velocity

Returning to the particle picture for inspiration [Figure 55], it is expected that ions drifting through the diffusion channel will eventually find themselves captured by the outflowing magnetic fields and will have their z-directed trajectories bent toward the x-direction. In that scenario we would expect a relationship between v_z and v_x. Namely:

$$v_z \sim v_x.$$

More importantly, we can see in Figure 56 that our expectation is well represented in simulation. The figures compare v_z to v_x for three drastically different equilibrium parameters. In all three cases, there is a clear scaling relationship between the two plasma flows.

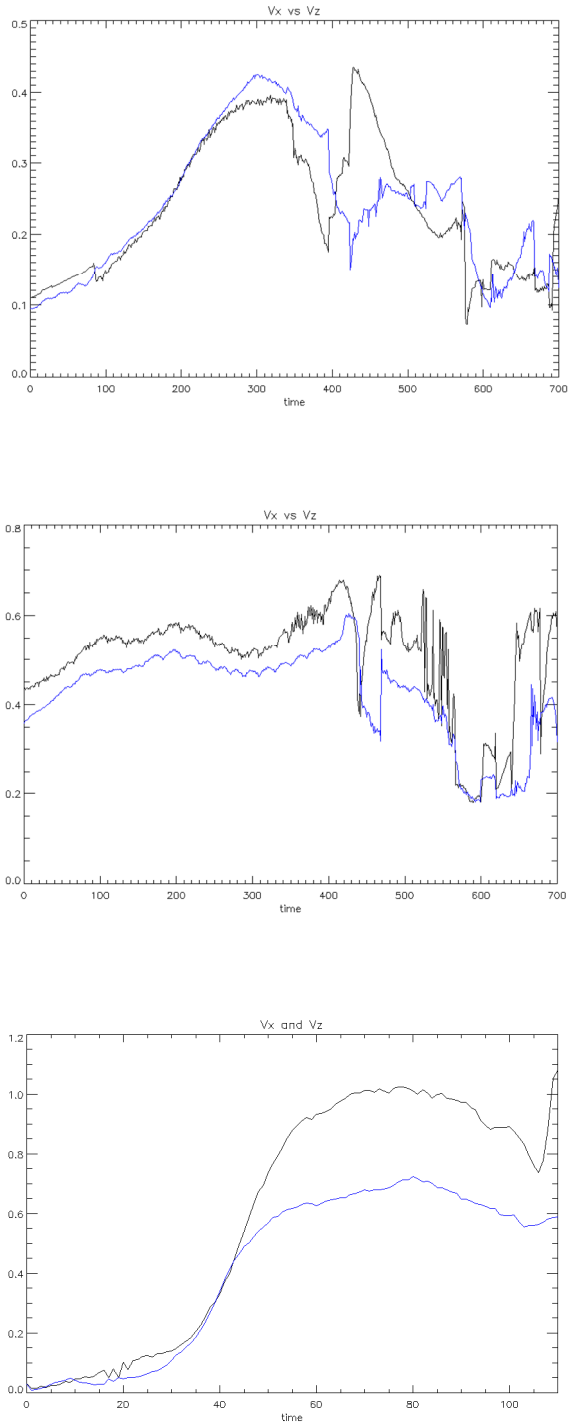

Figure 56 (107.43, 107.48, 107.8) Peak velocities. In black is v_x, the outflow velocity. Plotted in blue, v_z, is the plasma flow velocity along the x-line.

Southside Scaling

If we return to our basic picture of reconnection depicted in Figure 54, we have 3 reconnection regions. We're going to focus on two of these regions in the steady state – the 2D-like central region and the southern exhaust-like region.

As mentioned in Chapter 4, the southern region is bounded by a flow-stagnation point on the bottom and a density minimum at the top. The steady state flow of plasma through the south can be represented by,

$$v_z \rho(L_x L_y) = 2 v_x \rho(L_S L_y).$$

The variables are taken to be averages over their respective flux boundaries, $L_x L_y$, $L_S L_x$, and $L_S L_y$, respectively. Since the plasma flux from the current sheet wall is typically much smaller than the flux from the z-direction, we neglect the term $v_y \rho(L_S L_x)$.

We can use the observation that,

$$v_z \sim v_x.$$

To immediately derive that the length scale on the south should be a constant roughly of the order:

$$L_S \sim \frac{1}{2} L_x.$$

To see whether or not this scaling relationship is borne out in the simulation, we plot L_s for eight different x-lines in Figure 57. These x-lines represent the spectrum of results we observed in simulation -- everything from rigorously spreading to collapsing x-lines. Plotted together in the upper pane are runs which reconnected for several hundred Alfven time units. In black and green are solitary x-lines which showed a propensity to reconnect indefinitely. In blue are the x-lines which were transient. The important point is that all of the x-lines appeared to have an L_s which was independent of the extent or duration of the x-line. This is reminiscent of the

other reconnection length scale, L_x. In the bottom pane, we visit the other side of the spectrum. These two x-lines represent classically spreading x-lines which reconnect very strongly. Even though they are very different systems than those in the upper pane, they also express an L_s which seems to remain roughly constant.

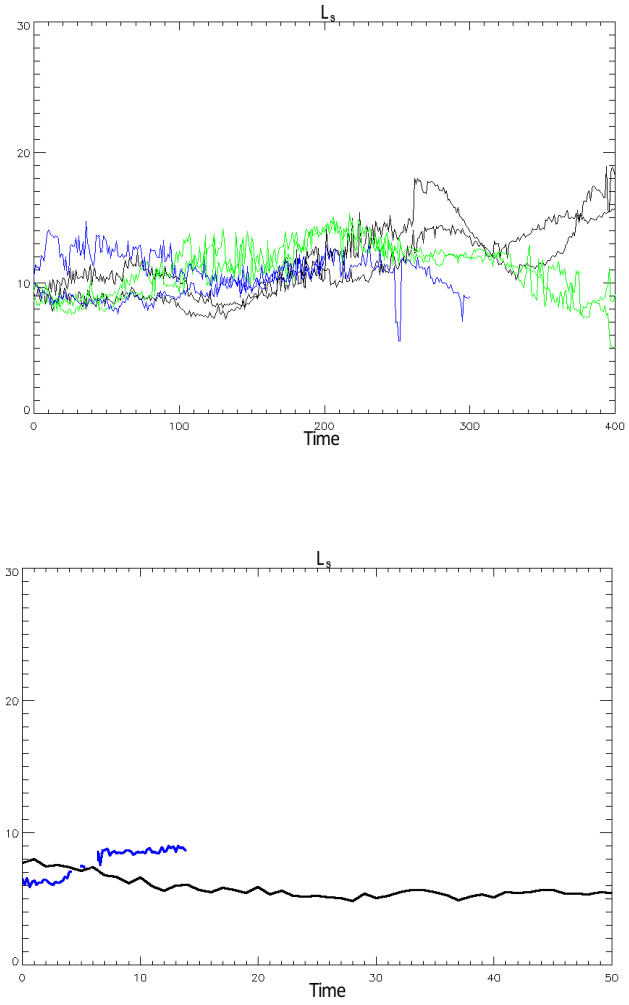

Figure 57 (Top)(107.42, 107.47, 107.50 : blue, green, black) Plots of L_s for six different current sheets in 3 separate simulation configurations. (Bottom)(105.3, 107.8 : blue, black) Additional plots of L_S for simulations on much shorter time-scales.

Joint Scaling

Looking at the scaling of the southern region alone allowed us to derive the length scale, L_s. In doing so we have established that the south-side is a permanent fixture in the reconnection structure. With that done we look to question the impact of the south-side on the larger reconnection ecosystem. In order to do this, we join it to the central region and analyze the flux of energy and plasma flowing into and out of them jointly. Together, we have a plasma flux of

$$\rho m v_y (L_x L_c) + \frac{1}{2}\rho m v_z \left(L_x L_y\right) \sim \rho m v_x \left(L_y L_T\right).$$

And we have an energy flux of

$$B_x^2 v_y (L_x L_c) + \frac{1}{2} m \rho v_z^3 (L_y L_x) \sim \rho m v_x^3 \left(L_y L_T\right) + W_{compression}.$$

In these equations, we've introduced the length scale L_T. L_T is the combined z extent of the central and southern regions, $L_T = L_S + L_c$.

If we use the scaling we found in our previous section,

$$v_z \sim v_x,$$

$$v_z = \alpha v_x.$$

And the assumption that the z-flowing energy remaining after compression is small compared to the magnetic energy flux into the entire system,

$$\frac{1}{2} m n v_z^3 \left(L_x L_y\right) - \mathrm{W} \ll B_x^2 v_y (L_x L_c).$$

The existence and position of the flow stagnation point lets us know that this is a reasonable approximation. If the flow carried much more or less energy than was demanded by the compression, then there would be substantial plasma flow south of the x-line.

We can solve for $v_y L_x L_c$ in the continuity equation

$$v_y L_x L_c \sim L_y v_x \left(L_T - \frac{\alpha}{2} L_x\right).$$

And use that in addition to

$$B_x^2 v_y (L_x L_c) \sim n m v_x^3 \left(L_y L_T\right).$$

To derive,

$$v_x^2 \sim \frac{B_x^2}{n m L_T} \left(L_T - \frac{\alpha}{2} L_x\right). \tag{13}$$

Although ignoring the capacity of the southern end to have a magnetic inflow of its own, this equation does capture the essential dynamics of the x-line in 3D. It expresses that the magnetic influx driving the extended length of reconnection must energetically carry the burden of the southern end. In other words, energy inflow scales with L_c, while energy outflow scales with L_T. For very large values of L_T, they are approximately equal, so there is no issue. However, for small values of L_T, this becomes problematic.

This situation occurs because of the large flux of plasma into the southern end from the regions above. This influx must go somewhere by continuity, so the south has a large obligation to produce an outflow. However, much of the energy that this influx contributes is spent compressing the gas. This leaves the x-line with a large energy burden which must be met. Because the z-flow approaches the maximum outflow velocity, it saturates the outflow channel in the south. The saturation of the outflow channel, in turn, restricts the amount of additional plasma that can be brought into the southern region from other sources. With limited room for additional plasma inflow, the energy demands cannot be fed by the magnetized plasma in the current sheet wall.

The only solution to this dilemma is to have the central region produce enough extra energy to support itself and the energy sink represented by the southern region.

Quite clearly, this introduces the concept of a minimum size for the x-line. The x-line must be at least $(\alpha/2)L_x$ in size in order to have an outflow. Exactly what this minimum is can't be divined from our scaling argument as there are constant factors neglected, but some reasonable estimations for those factors keep the minimum size near the range 5 to 15 c/ω_{pi}.

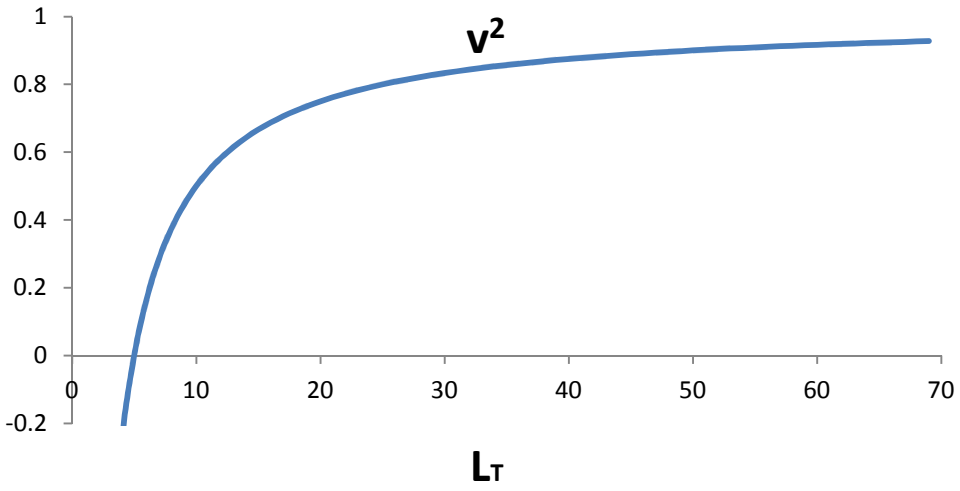

Figure 58 Plot of v_x^2 using Equation (13).

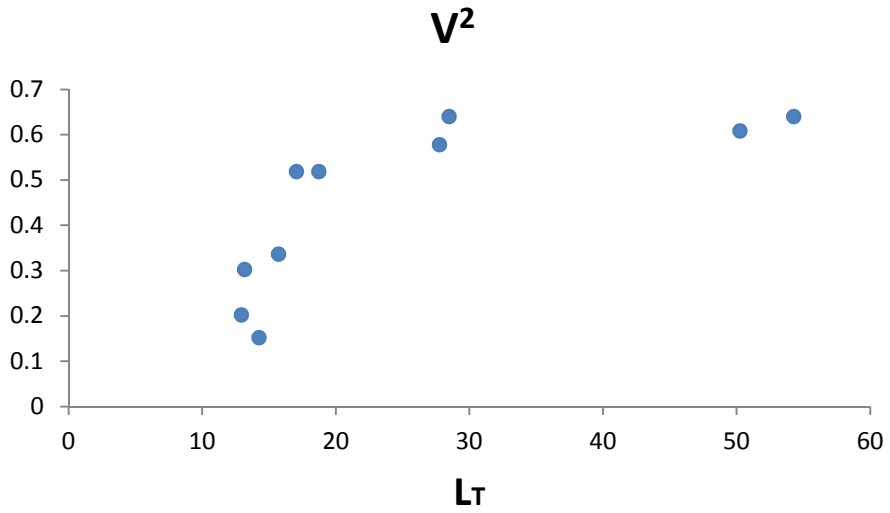

Figure 59 (107.43, 107.47, 107.49, 107.50, 107.51) Plot of v_x^2 when L_T is at its maximum size for 10 different transient x-lines. All runs have ω_0= 5.0 and $\mathcal{E}_0$ = 0.04.

In Figure 58, we plot the theoretical value of v_x^2 against L_T. In the following figure, Figure 59, we have the sister diagram plotting the equivalent values found in the transient and solitary x-line simulations, where $\omega_0 = 5.0$ and $\mathcal{E}_0 = 0.04$. The velocity is taken to be the peak velocity of the system. Both simulation and theory predict a cutoff length near 10 c/ω_{pi} and they predict that for large L_T the velocity should asymptotically approach similar maximum velocities. Here it was expected that the plotted points appear in pairs: one for each current sheet in a simulation.

Indeed, even including all of the runs where the x-line maintained a constant, and therefore measurable L_T, the theory maintains strong agreement with the simulations. A modified figure which includes runs with various initial perturbation sizes can be seen in Figure 60.

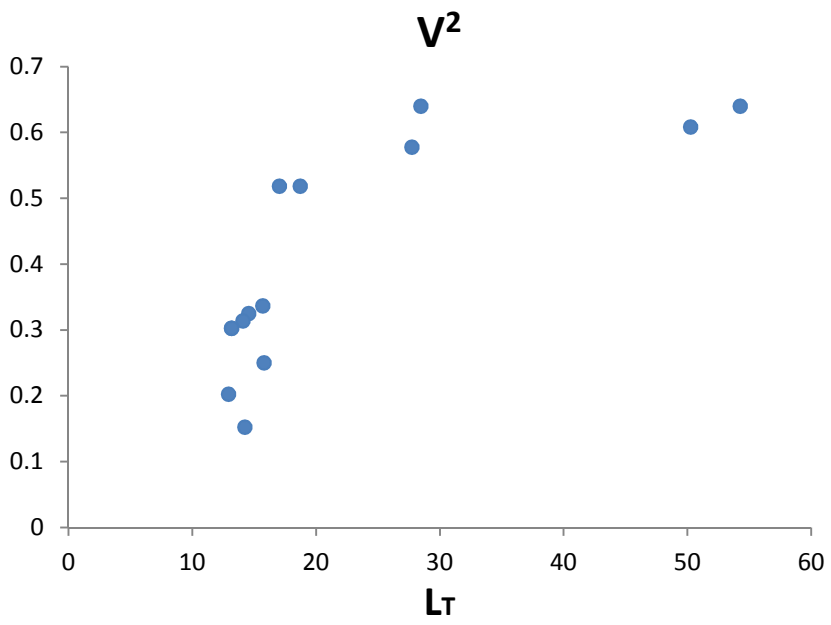

Figure 60 (107.42 107.41, 1077.4, 107.37, 107.34, 107.36, 107.30) Plots of v_x^2 versus maximum L_T for all x-lines with an equilibrium current sheet width, ω_0 = 5.0.

To see if there is any dependence of the outflow velocity on the initial perturbation parameters, we first plot the velocity against ω_{0z}. Although this reveals a clean linear relationship for the restricted data set, $\omega_0 = 5.0$ with $\mathcal{E}_0 = 0.04$, as can be seen in Figure 61. The correlation breaks down when different values of $\mathcal{E}_0$ are included [Figure 62]. In particular for the cases where $\omega_{0z} = 10$, we have a multi-valued results in simulation.

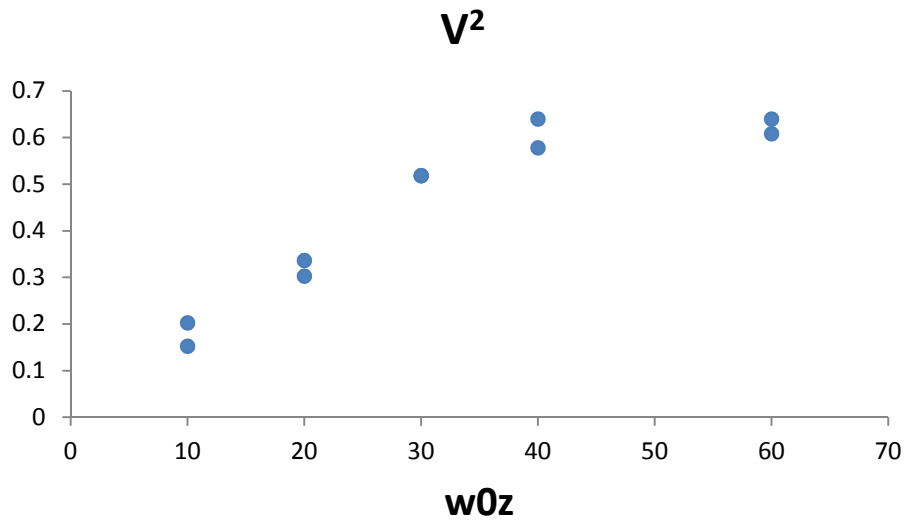

Figure 61 (107.43, 107.47, 107.49, 107.50, 107.51) Outflowing velocity versus the size of the seed perturbation in the z-direction for runs with ω_0= 5.0 and $\mathcal{E}_0$ = 0.04.

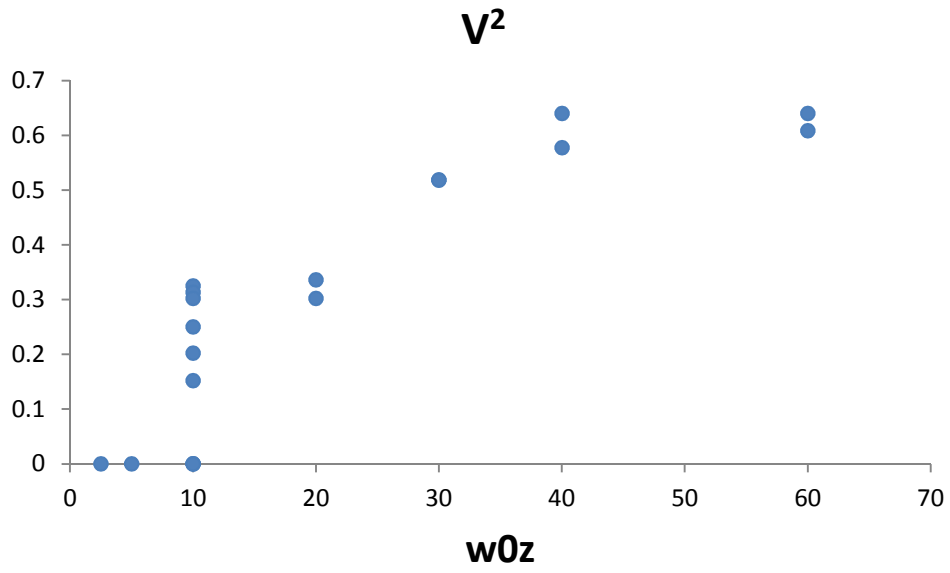

Figure 62 (107.42 107.41, 1077.4, 107.37, 107.34, 107.36, 107.30) Plot of velocity versus seed perturbation size in the z-direction, ω_{0z} for all runs where $\omega_0 = 5.0$.

However, taking a cue from our earlier observation that the viability of a current sheet for reconnection depends on the product, $\omega_{0z}\mathcal{E}_0$, we plot the velocity against that in Figure 63. This plotting breaks the multi-valued stacking and sorts the data well. Recall from earlier that the perturbation energy scales with the perturbation magnitude and the perturbing volume,

$$\mathcal{E}_1 \sim \omega_0 \omega_{0z} \mathcal{E}_0.$$

Since all of these runs have the same ω_0, the terms remaining to tune the perturbation energy are ω_{0z} and $\mathcal{E}_0$. In other words, very wide current sheets may not be unstable to reconnection without the presence of a strong perturbation. Even with a

strong perturbation, the reconnection produced will not grow freely in the out of plane direction. It may produce a transient x-line or drift as a solitary x-line. Marked in yellow on the figure is the region in which none of the current sheets were unstable to reconnection. Marked in blue are the initial configurations which produced transient x-lines. The remaining configurations appeared to be solitary for very long time frames.

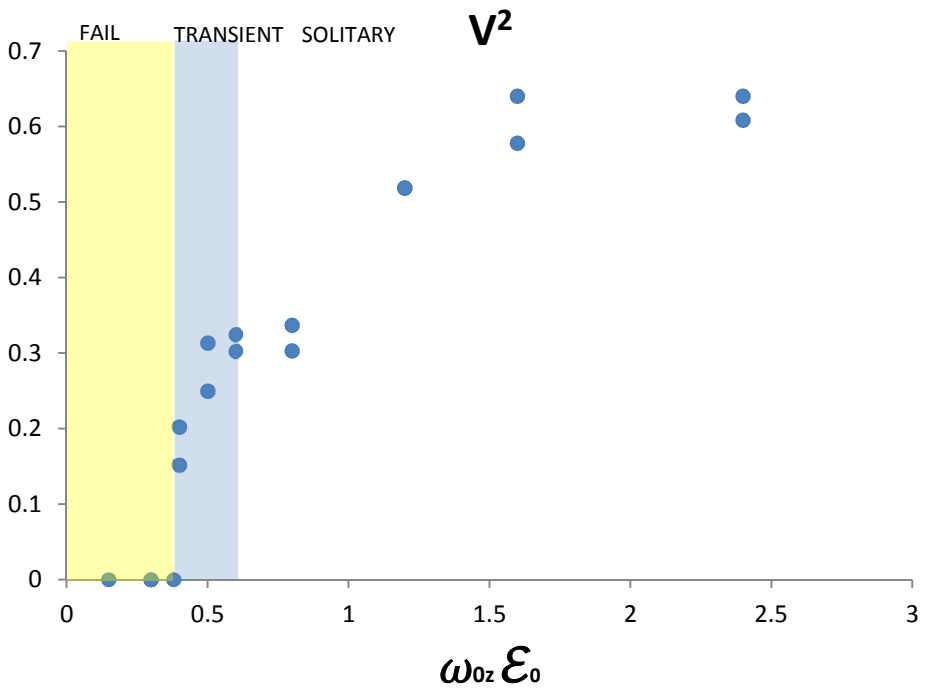

Figure 63 (All x-lines with $\omega_0 = 5.0$, including failed runs) Plot of v_x^2 versus the energy of the seed perturbation.

As we discussed earlier, there should be a minimum x-line length which produces stable reconnection. Plotting the x-line length, L_T, versus the perturbation energy, $\omega_{0z}\mathcal{E}_0$, shows this restriction nicely [Figure 64]. Colored in red and growing

linearly with the perturbation energy are the solitary x-lines. In green, most of the transient x-lines have approximately the same length, $L_T = 15\ c/\omega_{pi}$. Everything below the perturbation energy 0.4 completely failed to reconnect and are represented by X's. The stagnation in x-line growth as the energy supplied grows from .04 to .07, suggests that like a thermodynamic phase transition, the reconnection site must undergo some internal configuration change after onset in order to become stable. This reconfiguration of the internal structure comes with an energy cost. Every case of reconnection studied, once begun, transitions from the wide Sweet-Parker like current sheet structure to the fixed Petschek-like structure. This geometry change happening regardless of the initial energetics of the system means that it is unlikely to be the configuration change consuming the activation energy. This leaves one major configuration change unaccounted for – the opening of the outflow nozzles as depicted at the end of Figure 10.

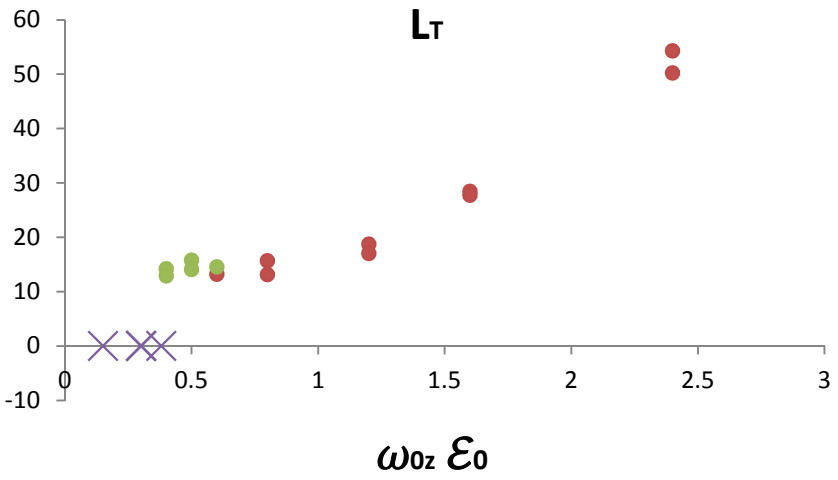

Figure 64 Plot of the maximum length of the x-line for all runs with $\omega_0 = 5.0$. In red are runs which appear to be solitary – lasting indefinitely. In green are x-lines which collapse, showing a transient behavior. Purple X's demark runs which failed to reconnect at all. The x-axis represents the energy in the initial seed perturbation.

Finally, to test the applicability of the scaling law,

$$v_x^2 \sim \frac{B_x^2}{nmL_T}\left(L_T - \frac{\alpha}{2}L_x\right),$$

to a general x-line, we present a scatter plot of v_x^2 versus L_T for two rapidly spreading x-lines in Figure 65. Unlike in the simulations for the previous plots using L_T, the strongly reconnecting x-line grows continuously. As such L_T, is not a measurement of the maximum value, rather it is a measurement of the x-line length as a function of time. In any case, we see that this scaling law holds for more than just marginal reconnection sites.

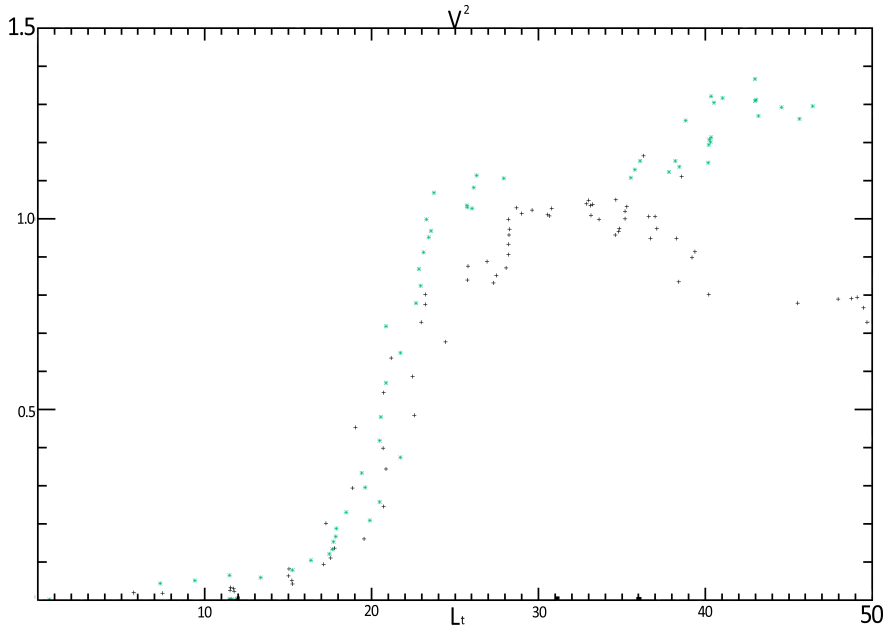

Figure 65 (107.8) Scatter plot of v_x^2 versus L_T for two strongly reconnecting x-lines.

The results of Figure 65 solidify the importance of the north/south interplay as a fundamental aspect of reconnection.

Conclusion

In this dissertation, we first presented a novel way of tracking and classifying reconnection along the spreading x-line by using the quantity $\partial v_{ix}/\partial x$. With this metric we were then able to correlate significant 3D structures within the x-line to the better known 2D aspect ratios and behaviors. Of principal importance was the discovery that the density plays a significant role in the asymmetric spreading of the x-line and its minima also serves to bifurcate the x-line into a distinct northern and southern region.

After presenting a basic outline for the structure of 3D reconnection, we then probed the domain of marginal reconnection with very large equilibrium current sheets. In this section, we presented examples of reconnection systems which are not unstable to the tearing mode as well systems whose instability was only transient – both in contradistinction to their 2D counterparts. By investigating these marginal reconnection cases in the context of our established 3D structure, we were able to identify the principle mechanism by which the transient reconnection sites collapsed.

And from that mechanism, in the following section, we were able to construct a simple 3D model of reconnection. This model proposes that the south-side of the reconnection site acts as an energy sink on the x-line as a whole. Using this model, we derived a new constant length scale, L_S for the size of the south-side of the reconnection site. We showed that the activation energy required for the onset of reconnection scales with the initial perturbation, $\omega_{0z}\mathcal{E}_0$. And finally we derived a new scaling law for the reconnection outflow speed:

$$v_x^2 \sim \frac{B_x^2}{nmL_T}\left(L_T - \frac{\alpha}{2}L_x\right).$$

This outflow speed was shown to be consistent with x-lines initiated through many different starting equilibriums. And from the equation, we have inferred the existence of a minimum stable x-line length.

As a whole this work greatly strengthens the argument that bursty bulk flows in the magnetotail are the outflows of smaller magnetic reconnection events. The minimum x-line lengths observed in simulation are comparable to the same properties in observed BBFs; when scaled to the conditions in the magnetotail, the simulation length scale of 15 is roughly equivalent to $.7R_E$. Likewise the outflow velocities, being roughly 50% - 75% of the Alfven speed also match the observed BBF speeds. The defining characteristic of BBFs, being short bursts of plasma flow lasting between 1 and 10 minutes, was also seen in simulation. The shortest duration transient x-line found in our work lasted approximately 1 minute, while the longest lasting transient x-line lasted 6 minutes. Finally, the equilibrium current sheet condition, $\omega_0 = 5.0$, when converted into the magnetotail dimensions of 1,423 km was observed by *Nakamura et el.* to be the approximate width of the current sheet just before the observation of BBF outflows [38].

So not only does the novel x-line behavior presented in this thesis introduce the adaptability needed in order to explain the observed BBF phenomenon, but its apparent constraints also fall within the parameter regime required to explain them.

BIBLIOGRAPHY

[1] V Angelopoulos et al., "Statistical characteristics of bursty bulk flow events," *Journal of Geophysical Research: Space Physics (1978--2012)*, vol. 99, pp. 21257--21280, 1994.

[2] V Angelopoulos et al., "Characteristics of ion flow in the quiet state of the inner plasma sheet," *Geophysical Research Letters*, vol. 20, pp. 1711--1714, 1993.

[3] V Angelopoulos et al., "Magnetotail flow bursts: association to global magnetospheric circulation, relationship to ionospheric activity and direct evidence for localization," *Geophysical research letters*, vol. 24, pp. 2271--2274, 1997.

[4] WI Axford, "Magnetic field reconnection," *Geophysical Monograph Series*, vol. 30, pp. 1--8, 1984.

[5] Wolfgang Baumjohann, Gotz Paschmann, and Hermann Luhr, "Characteristics of high-speed ion flows in the plasma sheet," *Journal of Geophysical Research: Space Physics (1978--2012)*, vol. 95, pp. 3801--3809, 1990.

[6] J Birn et al., "Geospace Environmental Modeling (GEM) magnetic reconnection challenge," *Journal of Geophysical Research: Space Physics (1978--2012)*, vol. 106, pp. 3715--3719, 2001.

[7] Joachim Birn, M Hesse, K Schindler, and S Zaharia, "Role of entropy in magnetotail dynamics," *Journal of Geophysical Research: Space Physics (1978--2012)*, vol. 114, 2009.

[8] Dieter Biskamp, "Magnetic reconnection via current sheets," *Physics of Fluids*, vol. 29, p. 1520, 1986.

[9] Allen H Boozer, "Reconnection and the ideal evolution of magnetic fields," *Physical review letters*, vol. 88, p. 215005, 2002.

[10] MR and Cothran, CD and Landreman, M and Schlossberg, D and Matthaeus, WH Brown, "Experimental observation of energetic ions accelerated by three-dimensional magnetic reconnection in a laboratory plasma," *The Astrophysical Journal Letters*, vol. 577, no. 1, p. L63, September 2002.

[11] MR and Cothran, CD and Fung, J Brown, "Two fluid effects on three-dimensional reconnection in the Swarthmore Spheromak Experiment with comparisons to space data," *Physics of Plasmas*, vol. 13, no. 5, p. 056503, 2006.

[12] Jinbin Cao et al., "Kinetic analysis of the energy transport of bursty bulk flows in the plasma sheet," *Journal of Geophysical Research: Space Physics*, 2013.

[13] CX Chen and RA Wolf, "Interpretation of high-speed flows in the plasma sheet,"

Journal of Geophysical Research: Space Physics (1978--2012), vol. 98, pp. 21409--21419, 1993.

[14] CD and Landreman, M and Brown, MR and Matthaeus, WH Cothran, "Three-dimensional structure of magnetic reconnection in a laboratory plasma," *Geophysical research letters*, vol. 30, no. 5, 2003.

[15] John C Dorelli, Amitava Bhattacharjee, and Joachim Raeder, "Separator reconnection at Earths dayside magnetopause under generic northward interplanetary magnetic field conditions," *Journal of Geophysical Research: Space Physics (1978--2012)*, vol. 112, 2007.

[16] S Dubyagin et al., "Can flow bursts penetrate into the inner magnetosphere?," *Geophysical Research Letters*, vol. 38, 2011.

[17] James W Dungey, "The interplanetary magnetic field and the auroral zones," techreport 1962.

[18] JP Eastwood, TD Phan, SD Bale, and A Tjulin, "Observations of turbulence generated by magnetic reconnection," *Physical review letters*, vol. 102, p. 035001, 2009.

[19] JT Gosling et al., "Direct evidence for prolonged magnetic reconnection at a continuous x-line within the heliospheric current sheet," *Geophysical Research Letters*, vol. 34, p. L06102, 2007.

[20] JT Gosling, S Eriksson, RM Skoug, DJ McComas, and RJ Forsyth, "Petschek-type reconnection exhausts in the solar wind well beyond 1 AU: Ulysses," *The Astrophysical Journal*, vol. 644, p. 613, 2006.

[21] JT Gosling, RM Skoug, DJ McComas, and CW Smith, "Direct evidence for magnetic reconnection in the solar wind near 1 AU," *Journal of Geophysical Research: Space Physics (1978--2012)*, vol. 110, 2005.

[22] JT Gosling, RM Skoug, DJ McComas, and CW Smith, "Magnetic disconnection from the Sun: Observations of a reconnection exhaust in the solar wind at the heliospheric current sheet," *Geophysical Research Letters*, vol. 32, 2005.

[23] Eo G Harris, "On a plasma sheath separating regions of oppositely directed magnetic field," *Il Nuovo Cimento Series 10*, vol. 23, pp. 115--121, 1962.

[24] Michael Hesse, Masha Kuznetsova, and Joachim Birn, "Particle-in-cell simulations of three-dimensional collisionless magnetic reconnection," *Journal of Geophysical Research: Space Physics (1978--2012)*, vol. 106, pp. 29831--29841, 2001.

[25] M Hesse and K Schindler, "A theoretical foundation of general magnetic reconnection," *Journal of Geophysical Research: Space Physics (1978--2012)*, vol. 93, pp. 5559--5567, 1988.

[26] JD Huba, JF Drake, and NT Gladd, "Lower-hybrid-drift instability in field reversed plasmas," *Physics of Fluids*, vol. 23, p. 552, 1980.

[27] JD Huba and LI Rudakov, "Hall magnetohydrodynamics of neutral layers,"

Physics of Plasmas, vol. 10, p. 3139, 2003.

[28] JD Huba and LI Rudakov, "Three-dimensional Hall magnetic reconnection," *Physics of Plasmas*, vol. 9, p. 4435, 2002.

[29] S Hu, A Bhattacharjee, J Dorelli, and JM Greene, "The spherical tearing mode," *Geophysical research letters*, vol. 31, 2004.

[30] Margaret G Kivelson and Christopher T Russell, *Introduction to space physics*.: Cambridge university press, 1995.

[31] James A Klimchuk, "On solving the coronal heating problem," *Solar Physics*, vol. 234, pp. 41--77, 2006.

[32] James A Klimchuk and Lisa J Porter, "Scaling of heating rates in solar coronal loops," 1995.

[33] Giovanni Lapenta et al., "Kinetic simulations of x-line expansion in 3D reconnection," *Geophysical research letters*, vol. 33, p. L10102, 2006.

[34] Yun-Tung Lau and John M Finn, "Three-dimensional kinematic reconnection in the presence of field nulls and closed field lines," *The Astrophysical Journal*, vol. 350, pp. 672--691, 1990.

[35] WH Matthaeus, JJ Ambrosiano, and Melvyn L Goldstein, "Particle acceleration by turbulent magnetohydrodynamic reconnection," *Physical review letters*, vol. 53, p. 1449, 1984.

[36] T Nagai et al., "Geotail observations of the Hall current system: Evidence of magnetic reconnection in the magnetotail," *Journal of Geophysical Research: Space Physics (1978--2012)*, vol. 106, pp. 25929--25949, 2001.

[37] R Nakamura et al., "Spatial scale of high-speed flows in the plasma sheet observed by Cluster," *Geophysical research letters*, vol. 31, 2004.

[38] R Nakamura et al., "Fast flow during current sheet thinning," *Geophysical research letters*, vol. 29, p. 2140, 2002.

[39] S Ohtani and T Mukai, "Plasma sheet expansion: Statistical characteristics," *Journal of geophysical research*, vol. 111, p. A05206, 2006.

[40] S Ohtani, HJ Singer, and T Mukai, "Effects of the fast plasma sheet flow on the geosynchronous magnetic configuration: Geotail and GOES coordinated study," *Journal of Geophysical Research: Space Physics (1978--2012)*, vol. 111, 2006.

[41] S Ohtani et al., "Quiet time magnetotail dynamics and their implications for the substorm trigger," *Journal of Geophysical Research: Space Physics (1978--2012)*, vol. 107, pp. SMP--6, 2002.

[42] EV Panov et al., "Plasma sheet thickness during a bursty bulk flow reversal," *Journal of Geophysical Research: Space Physics (1978--2012)*, vol. 115, 2010.

[43] EN Parker, "Magnetic reconnection and the lowest energy state," *EARTH PLANETS AND SPACE*, vol. 53, pp. 411--416, 2001.

[44] Eugene N Parker, "Sweets mechanism for merging magnetic fields in conducting

fluids," *Journal of Geophysical Research*, vol. 62, pp. 509--520, 1957.

[45] Harry E Petschek, "Magnetic field annihilation," techreport 1963.

[46] TD Phan, JT Gosling, and MS Davis, "Prevalence of extended reconnection X-lines in the solar wind at 1 AU," *Geophysical Research Letters*, vol. 36, p. L09108, 2009.

[47] TD Phan et al., "A magnetic reconnection X-line extending more than 390 Earth radii in the solar wind," *Nature*, vol. 439, pp. 175--178, 2006.

[48] DH Pontius and RA Wolf, "Transient flux tubes in the terrestrial magnetosphere," *Geophysical research letters*, vol. 17, pp. 49--52, 1990.

[49] Eric R Priest, "Nonlinear Plasma Physics of the Solar Corona," , vol. 1320, 2011, p. 3.

[50] Eric R Priest, "The magnetohydrodynamics of current sheets," *Reports on Progress in Physics*, vol. 48, p. 955, 1985.

[51] E Priest and T Forbes, "Magnetic Reconnection (Cambridge," *UK: Cambridge*, 2000.

[52] Arjun Raj, Tai Phan, Robert P Lin, and V Angelopoulos, "Wind survey of high-speed bulk flows and field-aligned beams in the near-Earth plasma sheet," *Journal of Geophysical Research: Space Physics (1978--2012)*, vol. 107, pp. SMP--3, 2002.

[53] Alessandro RetinÃ² et al., "In situ evidence of magnetic reconnection in turbulent plasma," *Nature Physics*, vol. 3, pp. 236--238, 2007.

[54] K Schindler, M Hesse, and J Birn, "General magnetic reconnection, parallel electric fields, and helicity," *Journal of Geophysical Research: Space Physics (1978--2012)*, vol. 93, pp. 5547--5557, 1988.

[55] VA Sergeev, V Angelopoulos, JT Gosling, CA Cattell, and CT Russell, "Detection of localized, plasma-depleted flux tubes or bubbles in the midtail plasma sheet," *Journal of geophysical research*, vol. 101, pp. 10817--10, 1996.

[56] S Servidio et al., "Statistics of magnetic reconnection in two-dimensional magnetohydrodynamic turbulence," *Physics of Plasmas*, vol. 17, p. 032315, 2010.

[57] Michael A Shay, James F Drake, Richard E Denton, and D Biskamp, "Structure of the dissipation region during collisionless magnetic reconnection," *Journal of Geophysical Research: Space Physics (1978--2012)*, vol. 103, pp. 9165--9176, 1998.

[58] MA Shay, JF Drake, BN Rogers, and RE Denton, "The scaling of collisionless, magnetic reconnection for large systems," *Geophysical research letters*, vol. 26, pp. 2163--2166, 1999.

[59] MA Shay, JF Drake, M Swisdak, W Dorland, and BN Rogers, "Inherently three dimensional magnetic reconnection: A mechanism for bursty bulk flows?," *Geophysical research letters*, vol. 30, 2003.

[60] Kazunari Shibata, "Evidence of magnetic reconnection in solar flares and a unified model of flares," *Astrophysics and Space Science*, vol. 264, pp. 129--144, 1998.

[61] Kazunari Shibata, "Theory of Flares and MHD Jets," pp. 9--12, 1998.

[62] Kazunari Shibata and Syuniti Tanuma, "Plasmoid-induced-reconnection and fractal reconnection," *arXiv preprint astro-ph/0101008*, 2001.

[63] David P Stern, "Euler potentials," *American Journal of Physics*, vol. 38, p. 494, 1970.

[64] Brian P Sullivan, Barrett N Rogers, and MA Shay, "The scaling of forced collisionless reconnection," *Physics of plasmas*, vol. 12, p. 122312, 2005.

[65] Arcadi V Usmanov, Melvyn L Goldstein, and William H Matthaeus, "Three-dimensional Magnetohydrodynamic Modeling of the Solar Wind Including Pickup Protons and Turbulence Transport," *The Astrophysical Journal*, vol. 754, p. 40, 2012.

[66] Arcadi V Usmanov, William H Matthaeus, Ben Breech, and Melvyn L Goldstein, "An MHD Solar Wind Model with Turbulence Transport," , vol. 406, 2009, p. 160.

[67] Vytenis M Vasyliunas, "Steady state aspects of magnetic field line merging," *Magnetic reconnection in space and laboratory plasmas*, pp. 25--31, 1984.

[68] M Wiltberger, TI Pulkkinen, JG Lyon, and CC Goodrich, "MHD simulation of the magnetotail during the December 10, 1996, substorm," *Journal of Geophysical Research: Space Physics (1978--2012)*, vol. 105, pp. 27649--27663, 2000.